Doctoral Thesis

Modeling and Control of Direct-Drivable Radial Gap Magnetic Screw-Like *RotLin* Machine as a Novel Trend to Linear Actuation

（新しいリニアアクチュエータとしてのダイレクトドライブ・
ラジアルギャップ磁気ねじ型 **RotLin** モータのモデリングと制御）

by

CYUSA S. Christophe
チュサ シンバ クリストフ

Dissertation submitted to the
Department of Physics, Electrical and Computer Engineering
in partial fulfillment of the requirements
for the degree of
Ph.D. in **Electrical & Computer Engineering**

Graduate School of Engineering
Yokohama National University

Advisor:
Prof. Yasutaka Fujimoto

March 2018

Declaration

I hereby declare that I am the sole author of this bona fide Doctoral Thesis entitled **"Modeling and Control of Direct-Drivable Radial Gap Magnetic Screw-Like *RotLin* Machine as a Novel Trend to Linear Actuation"**. This is a true copy of the thesis, including any required final revisions, as accepted by my examiners.

I understand that my thesis may be made electronically available to the public.

CYUSA S. Christophe

Members of Ph.D. Dissertation Committee:

- Professor Atsuo Kawamura, *Yokohama National University*
- Professor Tsutomu Oyama, *Yokohama National University*
- Professor Yasutaka Fujimoto, *Yokohama National University*
- Associate Professor Tomoyuki Shimono, *Yokohama National University*
- Associate Professor Takao Tsuji, *Yokohama National University*

Abstract

The future trend of mechanical systems is to substitute most of them by Permanent Magnet (PM) and/or Electromagnetic based ones as new actuation technology for human support systems mainly in robotics, automation, electric vehicles, industrial systems and so on.

Most systems are characterized by, either rotary or linear motion, or their combinations. Rotary motion is achieved by simply choosing suitable motors based on their efficiency; whereas linear motion, more often, results from combination of servo motors with high ratio gears such as in electromechanical actuators.

This research thesis highlights a paradigm for future studies of the advanced direct-drivable safe and precise motion actuators and headlines design, modeling, simulation and implementation based control of a novel *RotLin* (Rotary-Linear) Radial-Gap Helical Machine. The machine is comprised of Stator, Mid-Layer Rotor and the Inner Layer Translator. This is a hybrid of Magnetic Screw with a Synchronous Motor by modifying the design concept.

Structurally, it is made of smartly piecewise helical-shaped Permanent Magnet which are radially magnetized and helically layered on both Rotor and Translator, and embedded into a nonmagnetic rotor frame. The 3D FEA simulation results and calculations confirmed the realization of rotary and linear motions. To confirm this model, a prototype was enacted and experimental verifications of its performance in terms of direct-drive position and speed control were conducted. This compact machine can realize high Thrust Force densities when used as a linear actuator.

RotLin actuator is flexible and almost maintenance free. Its flexibility can be improved through controlled backdrivability achieved by experimentally designing a closed-loop force controller to accurately make *RotLin* become more flexible in terms of backdrivability than in the case of intrinsic backdrivability, thanks to the torque DOb *(Disturbance Observer) on the system Rotary Motion side designed to compensate the effect of disturbance force through deflective torque. Moreover, Multi-Encoder-based Sensorless Force Control was also tackled.

RotLin is expected as one of direct-drivable machine for the new trend to linear actuation with its application in mechatronics, industrial systems, robotics, and human support systems where safe and precise motion is required, plus high thrust force densities per volume when used as actuator. Furthermore, it can also be used for wave energy harvesting.

Acknowledgements

First and foremost, I am thankful to The Almighty God for all His benedictions bestowed upon me and healthy life.

I am very grateful to The Government of Japan for the award of MEXT Scholarship, partial support through JASSO Scholarship (Monbukagakusho Honors Scholarship for Privately-Financed International Students), and The Goverment of Rwanda through the University of Rwanda for allowing me to go for Doctoral studies.

The research work presented in this dissertation was carried out under Y.Fujimoto Laboratory, Department of Physics, Electrical and Computer Engineering, Yokohama National University from 2014 to 2018. I am immensely grateful to my supervisor, Prof. Yasutaka Fujimoto, for having accepted me in his laboratory and providing me with great opportunities and directions, motivating ideas and invaluable advices without which this work would not have been possible. Mentioning also my thesis committee for their advices and guidances.

On this note I would like to extend my heartfelt appreciation to all Y.Fujimoto Lab members with whom we shared a lot of knowledge forging one another. Most particularly, I would like to mention some labmates in the same promotion who contributed a lot to my research such as Masato Koyama, Akihiro Suzumura, Kenta Nagano, Bui Van Dinh, and all the People who, in spite of being busy, were generous with their time and enthusiasm for translations.

In a special way, I express my heartfelt thanks to my beloved wife Clarisse UWIMANA and our sons CYUSA HOZO Jayden and CYUSA KENZO Jensen for being with me and supporting me. I am indebted to my parents, family, YEC SDA Church members and friends for their continuous prayers and supports.

Finally, I thank all the people who, in one way or another, contributed to the completion of this work among others.

GOD BLESS YOU ALL.

"Commit to the LORD whatever you do, and He will establish your plans."
Proverbs 16:3

CYUSA S. Christophe
Yokohama, Japan
March 2018

Table of Contents

List of Tables

List of Figures

Chapter 1

Introduction

1.1 Background

Stunning high-tech innovations and inventions made it possible to harness magnets and come up with new electromagnetic systems. For instance, mechanical systems in robotics, industrial equipment and in vehicles are being substituted by Permanent Magnet (PM) based ones by just mimicking their working principle. Concrete and more recent examples are the MagLev trains, magnetic screws, etc. In most systems, either rotary or linear motion, or their combinations are observed. To achieve rotary motion, the choice of motors depends on their mechanical efficiency and the corresponding work to be performed by the system. Conversely, to accomplish linear motion, combination of servo motors and high ratio gears such as harmonic gears is widely used in robotic applications.

Electric motors have high-velocity and low-torque characteristics, thus their outputs are reduced by high ratio gears. Pneumatics might also provide the compact direct-drive with resemblance to human/animal musculoskeletal agonistic/antagonistic pair structure. However, output in terms of efficiency and fast dynamic motion are still questionable. The nondirect-drive mechanisms such as motor coupled with pulley, gears, or belts are viable options for high performance though they exhibit Coulomb frictions and low or no backdrivability due to transmission losses, resulting in the lack of adaptability and safety.

Direct-drive mechanisms are almost free from backlash and friction and easy to realize for precise, high-speed, and safe motion. Therefore, from the viewpoint of controllability, the direct-drive mechanisms are suitable for robotics applications where safety issue is of great concern, for instance in the case of rehabilitaion robots expected to support future aging society. [1, 2]

Table 8.3 summarizes some of the already existing actuators and their characteristics [3–6]. Because of the deficiencies in both compact direct-drive and nondirect-drive in achieving linear motion from rotary motion, different types of machines emerging from engineering researches have been proposed to be the less prone to the highlighted deficiencies. Amongst which there are Tubular Linear PM Machine [7] and High Thrust Density Linear motor.

Conventional PM linear motors can produce direct-drive motion without using mechanical transmission devices. Hitherto, a lot of reseach works on PM linear synchronous motors have

been reported in [8–15]. Aspects like low thrust per unit volume characteristic imply the system size becoming relatively big for high-thrust application. In this framework, a high thrust density linear motor was proposed and from the perspective of thrust per air gap area, it can produce thrust forces two times higher than conventional PM synchronous motor and six times than linear induction motors.

From the point of view design, there are several aspects to improve thrust force of linear motors. Intuitively, thrust force is directly proportional to gap area and inversely proportional to gap length. One approach is to expand gap area without increasing volume by designing special 3-D structure motors.

Other example of high thrust-force linear motors/actuators can include Trans-Rotary Magnetic Gear [16–18], Magnetic Lead Screw (MLS) Machine [19–21], Direct-Drive systems free from backlash and frictions with high control precision and safe motion such as Spiral Motor [22, 23]; and also linear to rotary conversion is being explored with the aim of wave energy harvesting [24–26].

Spiral Motor is an axial-gap type motor in which the helical mover does not contact the helical stator when screwing in it under a proper magnetic levitation control. Thus, the motor realizes direct-drive motion without mechanical gears.

More about rotary and linear motions and their realizations have been clearly discussed on in previous research works. In [27], an analysis method, based on field solution, to calculate the thrust force of the magnetic screw-nut actuator system was proposed, and results for a particular set of parameters were in very close agreement with two-dimensional (2-D) and three-dimensional (3-D) finite element analyses (FEA) calculations. Also integrating the Magnetic Screw system with a stator winding was previously proposed by different researchers as a method of achieving high axial force density linear actuator from rotary torque. [28–30]

Acquiring inspiration from this last concept has been the starting point of this innovation research of a novel radial-gap helical actuator/machine comprised of an armature windings stator, a mid-layer rotor, and a translator. The invention concept is about creating linear motion from rotary motion and/or vice-versa, thus obtaining a magnetic screw-like driven by the rotating magnetic field of PM synchronous stator in which it is incorporated. Thoroughly design concept, modeling, 3-D FEA based simulations, prototype development, test measurements and pre-drive control such as Open Loop V/f were highlighted in [31–35], and the current research thesis is an extended updated and detailed version of further improvements and mainly focusing on direct-drive position and speed control, mentioning also closed-loop force control aiming at improving RotLin's flexibility in terms of backdrivability.

In contrast to the conventional linear motors, this compact linear actuator can exhibit high thrust force with high backdrivability. This machine has a great advantage not only in the fact that it exhibits a relatively high thrust force, but also from the point of view design. For example, vis-à-vis to the model proposed in [24], the amount of magnets is reduced; this means instead of having inner and outer layers of magnets on the middle layer rotor, only one layer is considered to interact with stator's magnetic rotating field at the same time with the ones layered on the mover shaft. Furthermore, the PM used are purely helical shaped contrasted to the disc PM used in [24] to mimic helical shape. Also, Radial Gap Helical *RotLin* machine does not need unnecessary helical space like in the above cited model, which results in high thrust-force density per active

volume. Another advantage compared to the Axial Gap Helical/Spiral Motor, there is no need of controlling the gap since it is constant in the Radial Gap Helical Motor. It can have a wide range of applications in industrial robotics.

1.2 Objectives

The prime objective of this Doctoral Thesis is about Modeling and Implementation based Control of a Novel Radial-Gap Helical RotLin Machine.

1.3 Thesis Chapterization

This Doctoral Thesis consists of nine chapters described as follows.

- Chapter 1 - In this chapter, an introduction and background on linear actuator are given.
- Chapter 2 - In this chapter, linear actuation approaches and realization are highlighted.
- Chapter 3 - In this chapter, it is where the prime objective of this thesis begins. Concept, Design, Modeling and analytical analyses are detailed.
- Chapter 4 - In this chapter, simulations based on 3D Finite Element Analyses transient electromagnetic studies for the prediction of thrust force are discussed on.
- Chapter 5 - In this chapter, step by step experimental prototype manufacturing is highlighted.
- Chapter 6 - In this chapter, parameter identifications and measurements are given.
- Chapter 7 - In this chapter, drive control designs and tests are given.
- Chapter 8 - In this chapter, a comparative study of this novelity with other actuators is described.
- Chapter 9 - Finaly, conclusions, recommendations and future work are summarized.

Chapter 2

Linear Actuation Approaches

In this chapter, an overview of some actuators and their features is given.

2.1 State-Of-Art Overview of Linear Actuators

In this section, State-Of-Art brief description of some actuators categorized depending on their limitations and performances is given. The details are left to other technical papers.

2.1.1 Piezoelectric Actuators

Applying an external electric field e to materials exhibiting piezoelectric effect makes them to strain and thus yielding stress. There are multitude of occurences encompassing piezoelectricity ($\epsilon \propto e$), electrostriction ($\epsilon \propto e^2$) and ferroelectricity ($e = 0$); this last being the capability of maintaining a remnant polarization. A particular material's piezoelectric phenomenality relies upon its topological symmetry and its corresponding Curie temperature T_c above which the stable architecture is neither ferroelectric nor piezoelectric. [5]

2.1.2 Hydraulic and Pneumatic Actuators

Through a pressurized fluid flow, hydraulic and pneumatic actuators can yield force and displacement; albeit the actuator topology confines actuation pressure. Authors in [5] defined $\epsilon_{max} \approx 1$ as a tolerable upper limit, and σ_{max} as maximum actuation stress which is constrained by the operating fluid pressure.

In hydraulics there is a drawback of excessive-strain containment somehow dominating high pressure merits around 40-45MPa but higher pressures can be attainable; related systems have actuation stresses up to approximately 70MPa. [5]

In pneumatics, the operating fluid compressibility yields increase to both safety and energy performance boundaries at pressures in excess of about 1MPa and the dilemma on volumetric energy is decided accordingly to maximum sliding speeds v_{max}. [5]

2.1.3 Magnetostrictive Actuators

Underneath the effect of magnetic field, magnetostrictive materials can generate an actuation strain as a result of magnetic domains reorientation. This phenomenon is present in various materials; Terfenol-D ($Tb_{0.3}Dy_{0.7}Fe_{1.9}$) is the best and famous magnetostrictor characterized by high magnetostrain and low magnetic field at ambient temperature. However, some constraints such as magnetic field saturation can be a hinderance to the actuation strain. An analogy can be drawn between magnetostrictors and piezoelectrics performance factors. Therefore, the maximum operating frequency and the maximum power per unit volume can be determined. [5]

2.1.4 Electromagnetic Actuators

These are also termed power transducers based on electromagnetic principle and can be classified in solenoids, moving coil transducers and motors. Solenoids are just electromagnets made of coil in which the current flows, and a high permeability core which undergoes repulsion due to the energized coil magnetic field that gives Maxwell force rise. Commercially available solenoids are specified with a maximum actuation stress σ_{max} of around $1 \times 10^5 N/m^2$ and actuation strains that may reach 0.4. The major drawback of solenoids is their low frequencies (less than $100Hz$) due to the moving armature inertia. Frequencies of up to $50kHz$ can be realizable in moving coil transducers as the moving part is a low-inertia current-carrying coil. [5]

2.2 Magnetic Lead Screw

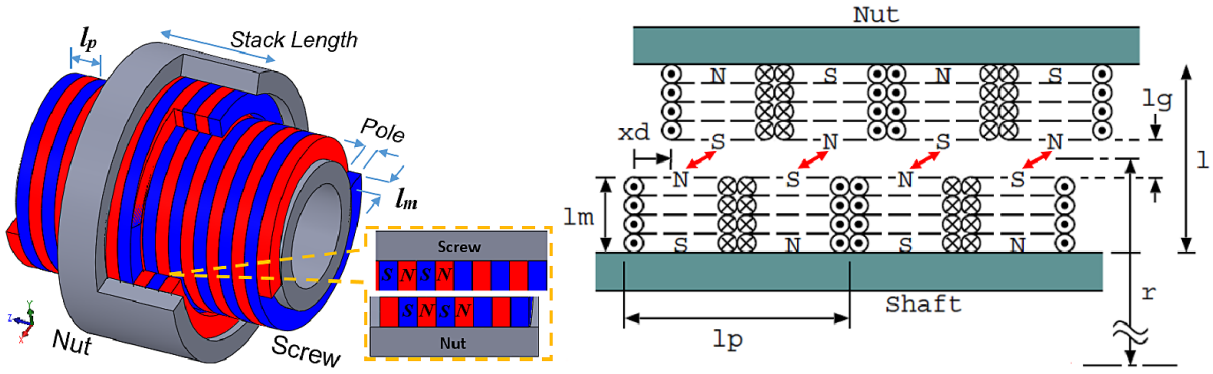

(a) MLS semi-section view

(b) MLS Equivalent Circuit Model

Figure 2.1: Magnetic Lead Screw *(MLS)

2.2.1 Modeling of the Embedded Magnetic Screw

Fig. 2.1(b) shows the simplified equivalent circuit model of a magnetic screw shown in Fig. 2.1(a). An equivalent magnetizing current flows through permanent magnets. Ignoring the mag-

Table 2.1: Parameters of *RotLin* Helical Motor

Nomenclature	**Description**
p	Number of pole pairs
x [mm]	Translational position of the Mover
x_d [mm]	Relative displacement of Mover
θ [rad]	Mechanical rotational angle of the Rotor
μ_0 [H/m]	Magnetic Permeability of vacuum
μ_m [H/m]	Magnetic Permeability of PM
J [kg·m^2]	Moment of Inertia of the Rotor
M [kg]	Mass of the Mover
l_g [mm]	Nominal air gap length
l_m [mm]	PM thickness
l_p [mm]	Pitch or Lead Length of screw
l [mm]	Nominal gap between Nut and Shaft irons
f [N]	Thrust-force of Mover
f_s [N]	Spring force
f_{load} [N]	Load force
τ_s [Nm]	Magnetic Spring Torque of the Rotor
I_m [A]	Equivalent magnetization current i.e PM
	Magneto-motive force
Ψ [Wb]	PM Flux linkage
K_τ [Nm/A]	Torque constant
K_f [N/A]	Thrust force constant
K_s [N/m]	Spring constant

netic resistance of the iron core, and the PM equivalent magnetizing current I_{m1} of magnetic nut, and the PM equivalent magnetizing current I_{m2} of the magnetic screw; inductance matrix is obtained as follows:

$$L = \begin{bmatrix} L_0 & M_0 \cos\left(\frac{2\pi}{l_p} x_d\right) \\ M_0 \cos\left(\frac{2\pi}{l_p} x_d\right) & L_0 \end{bmatrix} \tag{2.1}$$

Since $\mu_m \approx \mu_0$, they are assumed to be equivalent. Hence self inductance L_0 and mutual inductance M_0 are derived as follows:

$$L_0 = 1/R_m \tag{2.2}$$

$$M_0 = \frac{8}{\pi^2 R_m} \tag{2.3}$$

where R_m is magnetic resistance (Reluctance) of airgap R_{m0} and Permanent Magnets R_{mPM}, and given as follows:

$$R_m = R_{m0} + 2R_{mPM} \tag{2.4}$$

$$R_{m0} = \frac{l_g}{\mu_0 l_p 2\pi r} \tag{2.5}$$

$$R_{mPM} = \frac{l_m}{\mu_m l_p 2\pi r} \tag{2.6}$$

Considering a periodic function $f(x_d)$ where $f(x_d - l_p) = f(x_d)$, equation (2.3) is derived from the Fourier series fundamental component of $f(x_d)$.

$$C_1 = \frac{2}{l_p} \int_0^{l_p} f(x_d) \cos\left(\frac{2\pi}{l_p} x_d\right) dx_d \tag{2.7}$$

Solving Equation (2.7), when $f(x_d)$ is a triangular function (see Fig. 2.2) obtained from Fig. 2.1(b), yields the value of Mutual Inductance in Equation (2.3).

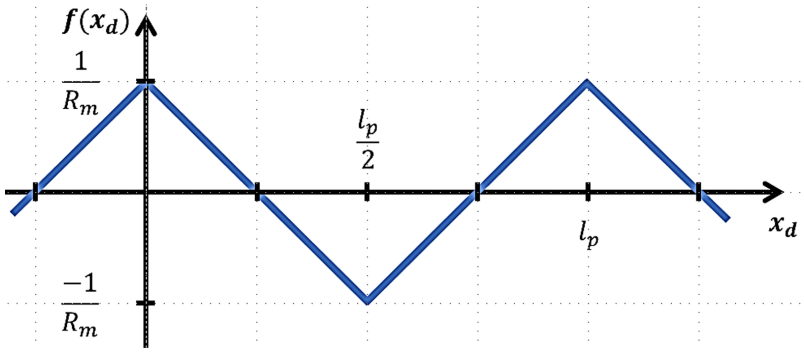

Figure 2.2: Triangular Function Wafeform

$$
\begin{aligned}
C_1 &= \frac{2}{l_p}\int_0^{l_p} f(x_d)\cos\left(\frac{2\pi}{l_p}x_d\right)dx_d \\
&= \frac{2}{l_p}\left[\int_0^{\frac{l_p}{2}} \frac{1}{R_{m\frac{l_p}{4}}}\left(\frac{l_p}{4}-x_d\right)\cos\left(\frac{2\pi}{l_p}x_d\right)dx_d + \int_{\frac{l_p}{2}}^{l_p} \frac{1}{R_{m\frac{l_p}{4}}}\left(x_d-\frac{3l_p}{4}\right)\cos\left(\frac{2\pi}{l_p}x_d\right)dx_d\right] \\
&= \frac{4}{l_p}\int_0^{\frac{l_p}{2}} \frac{1}{R_{m\frac{l_p}{4}}}\left(\frac{l_p}{4}-x_d\right)\cos\left(\frac{2\pi}{l_p}x_d\right)dx_d \\
&= \frac{8}{\pi^2 R_m}
\end{aligned}
$$

It implies $f(x_d)$ approximated as

$$
f(x_d) \simeq \frac{8}{\pi^2 R_m}\cos\left(\frac{2\pi}{l_p}x_d\right) \tag{2.8}
$$

and writen as

$$
f(x_d) \simeq M_0\cos\left(\frac{2\pi}{l_p}x_d\right) \tag{2.9}
$$

where $M_0 = \frac{8}{\pi^2 R_m}$

The spring force f_{s0} generated by the displacement x_d can be expressed by:

$$
f_{s0} = \frac{1}{2}\begin{bmatrix} I_{m1} & I_{m2}\end{bmatrix}\frac{\partial L}{\partial x_d}\begin{bmatrix} I_{m1} \\ I_{m2}\end{bmatrix} = -\frac{2\pi M_0 I_m^2}{l_p}\sin\left(\frac{2\pi}{l_p}x_d\right) \tag{2.10}
$$

where $I_{m1} = I_{m2} = B_r l_m/\mu_m$, B_r being the residual magnetic flux density of the PM and the derivative of L relative to the displacement x_d expressed as follows:

$$
\frac{\partial L}{\partial x_d} = \begin{bmatrix} 0 & -\frac{2\pi M_0}{l_p}\sin\left(\frac{2\pi}{l_p}x_d\right) \\ -\frac{2\pi M_0}{l_p}\sin\left(\frac{2\pi}{l_p}x_d\right) & 0\end{bmatrix} \tag{2.11}
$$

When the loading force exceeds the maximum value of the above equation (3) which represents the MLS stall force, the magnitude of the displacement exceeds $l_p/4$ and thereby pole slip occurs and leads to a loss of control. That is, the maximum value of the transmission power can exist. In addition, in the vicinity of the origin of the displacement x_d, the generated spring force f_{s0} is found to be a magnitude proportional to the displacement x_d. Then, if $x_d < l_p/4$, the spring force equation (2.10) can be approximated as follows, and acts as a spring which is proportional to the displacement. Refer to Appendix B for numerical approaches.

$$
f_{s0} \simeq -K_{s0}x_d \tag{2.12}
$$

2.3 Linear Electromagnetic Actuation Realization

Fig. 2.1(a) depicts ideal magnetic screw type using helically disposed, radially magnetized permanent magnet threads (i.e. magnetic nut and screw) and its equivalent circuit model is shown in Fig. 2.1(b), for which this research has departed from. In this situation, magnetic force is developed by the action of the magnetic nut and the magnetic screw in a contactless fashion. A rotation of 360^o, similar to that in mechanical system, results when the magnetic screw is displaced linearly by a distance l_p (lead length or pitch). The pitch is twice the magnetic pole-pitch or vice versa. Ideally, the principle of energy conservation relates the Torque T_n and Thrust force F_t as carried out in [27].

$$T_n = \frac{l_p}{2\pi} F_t \tag{2.13}$$

Thus proper selection of the magnetic pole-pitch results high thrust force through similar gearing effect of the mechanical screw, however, this approach is contactless and friction-free.

2.4 Summary

In this chapter, linear actuation approaches and realization were highlighted. State-Of-Art of existing Linear Actuator was given just summarizing the characteristics of some selected actuators. Next, MLS on which is based this current research was defined, presented and modeled. At the end an important Torque-Force relationship for magnetic screw was defined.

Chapter 3

Novel Radial Gap Helical *RotLin* Machine

3.1 Design Concept of *RotLin*

The idea stems from combining a conventional magnetic screw with the stator part of PM brushless motor for generating a torque to the nut, hence Thrust Force on the screw as it has been discussed on in the introduction.

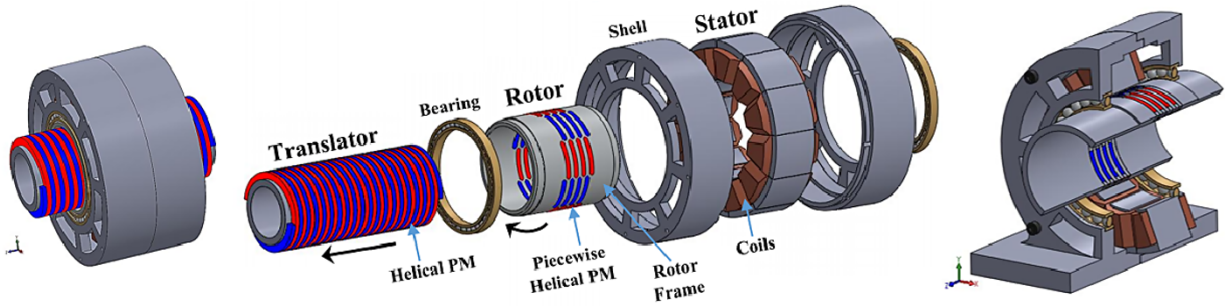

Figure 3.1: Compact, Exploded and Perspective Cross sectional views of *RotLin*

3.2 Features and Operating Principles

A new approach is proposed by integrating the magnetic screw into the stator of a motor, modifiy and rearrange the design of nut, that is going to be called Mid-Layer Rotor as shown in Fig. 3.2, and thus Radial Gap *RotLin* Helical Motor is achieved. It is a novel high-thrust linear actuator with high backdrivability. It is capable of converting rotary motion to linear motion and/or vice-versa. It can be used for converting electrical energy to mechanical energy and/or vice-versa.

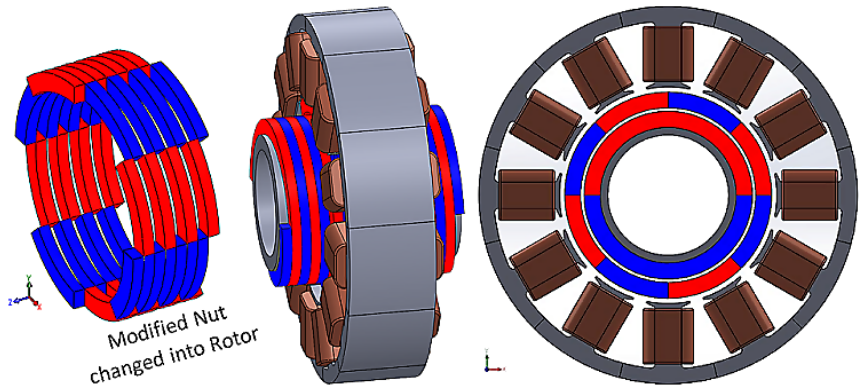

Figure 3.2: Radial Gap *RotLin* Helical Motor

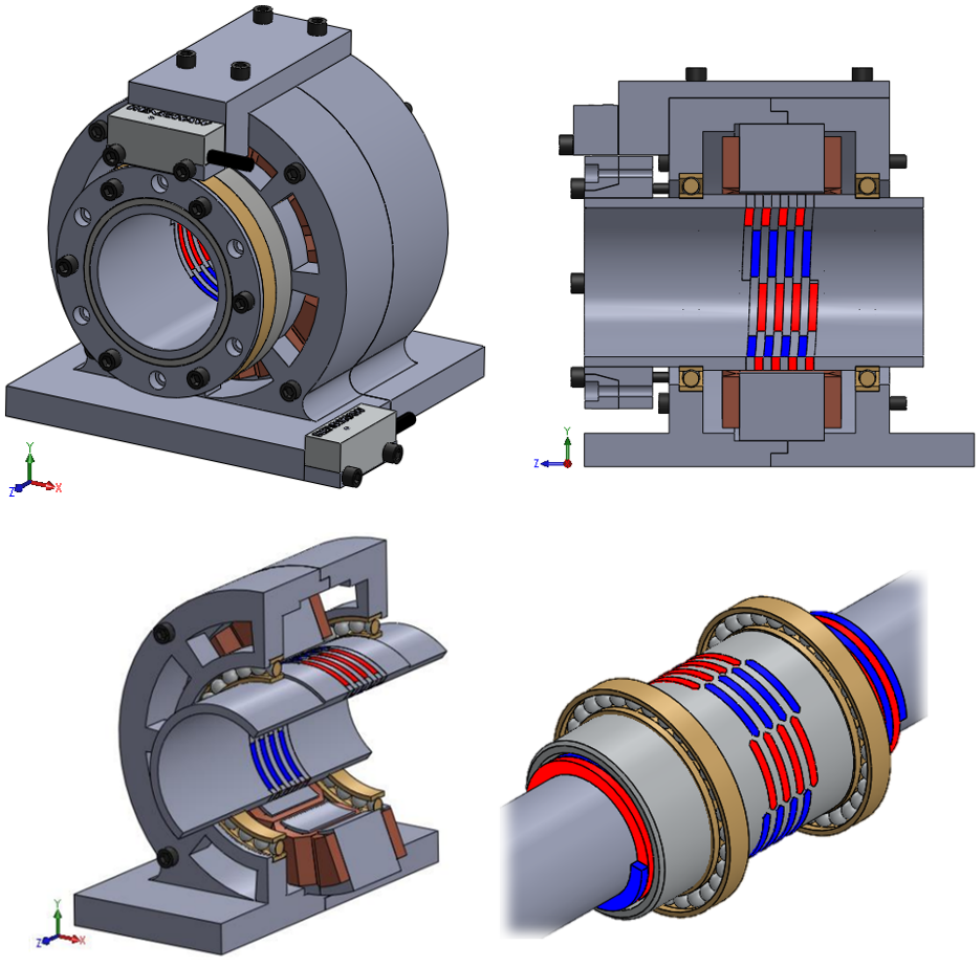

Figure 3.3: Radial Gap *RotLin* Helical Motor Concept

3.3 Modeling of *RotLin* Helical Machine

The aim of combining a motor and a magnetic screw is to generate a torque to the nut (now called Mid-Layer Rotor) and thus, this last rotating, with respect to the stator, around the screw (now called Translator), generates a translational force on this last. However, torque τ_s, in accordance with the displacement x_d of the helical magnet of the translator and helical magnet of the mid-layer rotor, acts as a load. Assuming I_m is constant and ignoring the zero-phase dynamic, the dq-axis Voltages of *RotLin* Helical motor are obtained by below equation matrix.

$$\begin{bmatrix} V_d \\ V_q \end{bmatrix} = \begin{bmatrix} L_d & 0 \\ 0 & L_q \end{bmatrix} \begin{bmatrix} \dot{I}_d \\ \dot{I}_q \end{bmatrix} + \begin{bmatrix} R & 0 \\ 0 & R \end{bmatrix} \begin{bmatrix} I_d \\ I_q \end{bmatrix} + p\dot{\theta} \begin{bmatrix} 0 \\ \Psi \end{bmatrix} + p\dot{\theta} \begin{bmatrix} 0 & -L_q \\ L_d & 0 \end{bmatrix} \begin{bmatrix} I_d \\ I_q \end{bmatrix} \tag{3.1}$$

where I_d, I_q are dq-axis currents; V_d, V_q are dq-axis voltages; and L_d, L_q are dq-axis inductances. Fig. 3.4 portrays the overall open-loop block diagram of Radial-Gap *RotLin* Helical Machine.

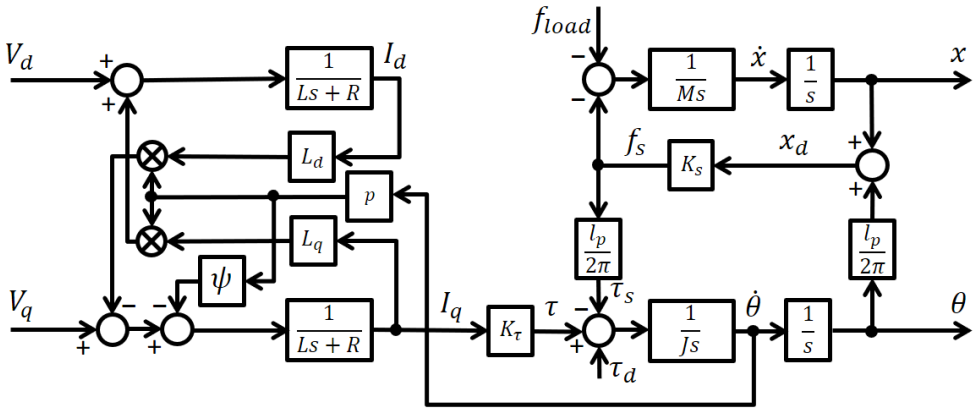

Figure 3.4: Radial Gap *RotLin* Helical Motor Open-Loop Block Diagram

The expanded voltage equations are given as follows:

$$L_d\dot{I}_d = -RI_d + L_q p\dot{\theta} I_q + V_d \tag{3.2}$$

$$L_q\dot{I}_q = -RI_q - L_d p\dot{\theta} I_d - p\dot{\theta}\Psi + V_q \tag{3.3}$$

The Dynamic/Motion equations of the Mid-Layer Rotor and Translator are respectively given by:

$$J\ddot{\theta} = p\Psi I_q + (L_d - L_q) I_d I_q + \tau_s \tag{3.4}$$

$$M\ddot{x} = f_s - f_{load} \tag{3.5}$$

where f_s is the generated thrust force due to the magnetic spring which is generated, substantially proportional to the translational displacement, and can be approximated by:

$$f_s = -K_s x_d \tag{3.6}$$

where

$$x_d = x + h\theta \tag{3.7}$$

is the relative displacement between the translator and mid-layer magnets; and

$$h = \frac{l_p}{2\pi} \tag{3.8}$$

is equivalent to the conversion ratio between rotary and linear motion.

The Mid-Layer Rotor contains no iron core i.e it has no salient poles, hence $L_d = L_q$ holds. Consequently, equation (3.4) is rewritten as follows.

$$J\ddot{\theta} = p\Psi I_q + \tau_s \tag{3.9}$$

Based on the energy conservation law $\dot{\theta}\tau_s + \dot{x}f_s = 0$, the force due to magnetic spring acting on the mover and the torque due to the magnetic spring acting on the mid-layer rotor are approximately related to each other by:

$$\tau_s = \frac{l_p}{2\pi} f_s \tag{3.10}$$

3.4 Summary

In this chapter, the novel machine described in this research thesis is presented, modeled and characteristic dynamic equations are derived as well as other important relationships like torque-force conversion; and also the overall plant model was presented using block diagram.

Chapter 4

FEM-Based Analysis of Radial-Gap Helical *RotLin* Machine

JMAG-Designer^{TM} *ver.14.1.02i* (*JSOL Corporation*'s simulation software for the development and design of Electromechanical Design to accurately analyze a wide range of physical phenomenon that includes complicated geometry and structure at the center of electromagnetic fields) has been used to predict torque and thrust force characteristics from FEA (Finite Element Analysis). It is an important tool to support design for electrical machine devices such as motors, actuators, transformers, circuit components and so on. Table 4.1 shows the simulation study properties while Table 4.3 shows the simulated model specifications. 3D-FEA method was applied to the proposed model and simulated in four steps described in the following sub sections. Fig. 4.1 depicts FEA mesh and magnetic flux densities. With *RotLin*'s dimensions, highest force density was calculated to be $6.14 MN/m^3$.

Table 4.1: 3-D FEA Simulation Study Properties

Analysis Type	3D Magnetic Field Transient Analysis
Model Size	$94.5 \times 94.5 \times 35$mm
Mesh Elements	100,872
Nodes	26,800
Calculation Type	Newton-Raphson
Nonlinear Max Iteration	150
Convergence Tolerance	0.001
Steps	61
Step / Time Step	0.490ms
Step / End Time (point) of Regular Intervals	8.333ms

Table 4.2: 3-D FEA Simulation Steps

FEA Simulation Test	**Parameter**	**Value**
SimTest 1	Current	0A
	Translator Speed	0.15m/s
	Rotor Speed	0rpm
	Initial Displacement x_d	0 mm
SimTest 2	Current	0A
	Translator Speed	0.15m/s
	Rotor Speed	1800 rpm
	Initial Displacement x_d	0 mm
SimTest 3	Current	5A
	Translator Speed	0.15m/s
	Rotor Speed	1800rpm
	Initial Displacement x_d	0mm
SimTest 4	Current	0A
	Translator Speed	0.15m/s
	Rotor Speed	1800 rpm
	Initial Displacement x_d	0.25mm
SimTest 5	Current	5A
	Translator Speed	0.15m/s
	Rotor Speed	1800 rpm
	Initial Displacement x_d	0.25mm

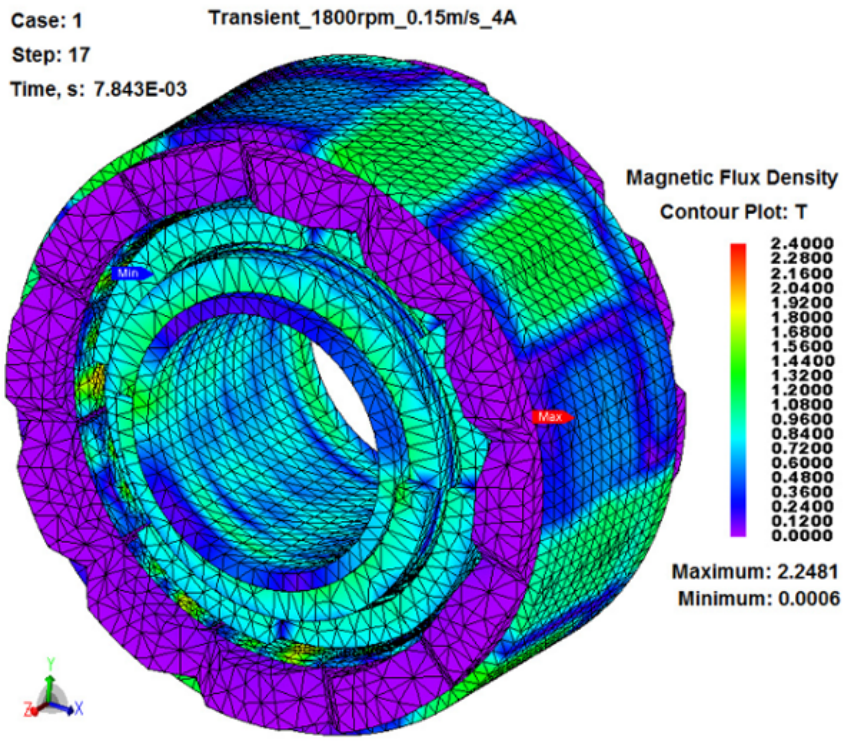

Figure 4.1: *RotLin*'s FEA Mesh and Magnetic Flux Densities

Table 4.3: Dimensions of the Simulated Radial Gap *RotLin* Helical Motor

Description	**Value**
Lead length l_p	5mm
Stator Outer diameter	94.5mm
Stator Inner diameter	54.1mm
Airgap Stator-MidLayer	0.8mm
Mid-Layer Outer diameter	52.5mm
Radial Thickness of Mover PM	4mm
Airgap MidLayer-Mover	0.8mm
Mover Outer diameter	42.9mm
Radial Thickness of Mid-Layer PM	4mm
Shaft Outer diameter	34.9mm
Axial Thickness of PM	2.5mm
Number of coil turns	30
Coil Wire Section	0.8mm
Current Density	9.947A/mm^2
Material Stator Core	15HX1000 JSOL
Material PM	NMX-41SH
Rotor PM Mass	48g
Material Mover Shaft	50A1000 JSOL
Stator Pole Face Area/Coil	324.961mm^2
Stator Stack Length	25mm

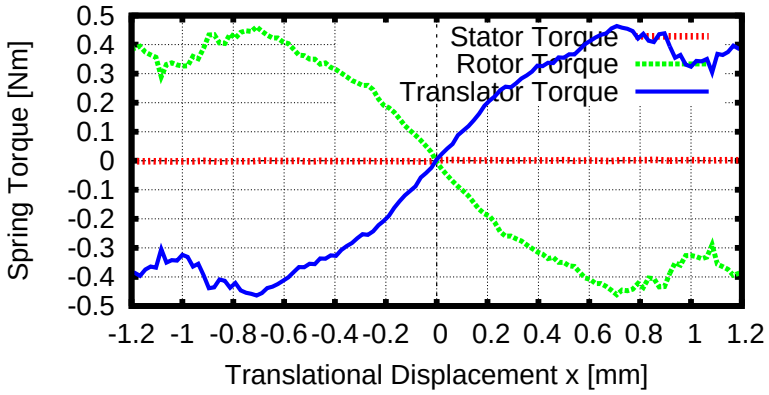

(a) Stall Torque Analysis

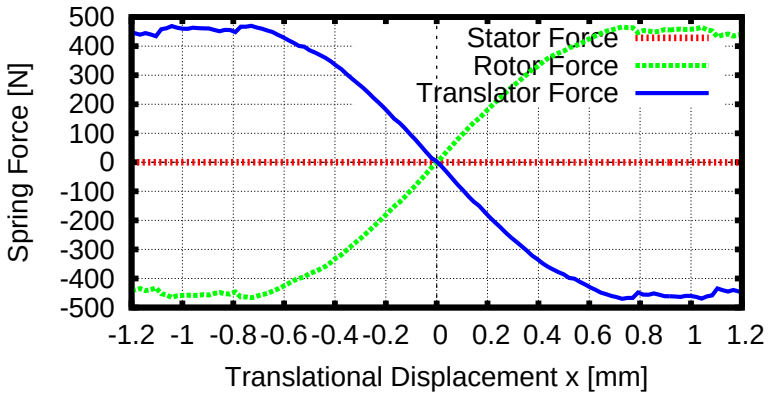

(b) Stall Force Analysis

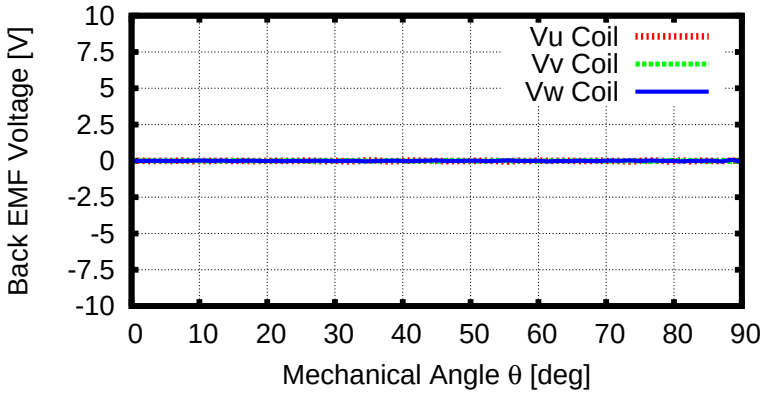

(c) Back emf voltage

Figure 4.2: 3-D FEA Simulation Test 1 [0rpm, 0.15m/s, 0A]

4.1 Magnetic Screw Stalling Properties

Simulation Test 1 is about testing of conventional magnetic screw stalling properties or equivalent magnetic spring characteristics. It is performed without any interaction of rotational speed, only testing the translational stall force of the incorporated magnetic screw under a preset translational speed. This test is similar to compressing and expanding a mechanical spring. Test conducted in both positive and negative axial translation direction. Fig. 4.2(a) and (b) depict the Stall Torque and relatively high Thrust Force which is saturated in the vicinity of $l_p/4$ peaking to around $400N$. Applying to it, a loading force greater than this last, leads to pole slip between Rotor and Translator PM. For up to 0.4mm displacement amount, it has a substantially linear spring characteristic $K_s = 850kN/m$. It is clearly observed that Newton's third law is obeyed between Rotor and Translator thrust forces. In Fig. 4.2(c), negligible back-EMF voltages due to the small motion of translator are observed on the stator coils.

4.2 Magnetic Screw and Synchronous Motor Hybrid

Simulation Test 2 is performed by incorporating the magnetic screw into synchronous motor; under the same conditions as previously, except that here a rotational speed, corresponding to the translational speed, is coupled to it. It is like in generator mode and results in Fig. 4.3(a) show that Torque is too small and rippling around zero, Thrust force (see Fig. 4.3(b)) almost none compared to previous results, and the presence of a considerable back-EMF voltage as observed in Fig. 4.3(c). Due to simulation conditions, the real back-EMF can be considered from around 5 degree rotation.

4.3 Three-Phase Current Source

Simulation Test 3 is a continuation of Test 2 in which a $5A$ three-phase current source is introduced in the simulation circuit to excite the stator coils and thus generate a rotating magnetic field producing a torque acting on the mid-layer rotor, consequently the stator receives a reaction torque. As the rotor rotates, the translator moves linearly. It is observed, in Fig. 4.4(a),(b) and (c), a considerable Torque on the rotor; but translator thrust force almost remains the same as in Test 2 and back-EMF voltages slightly rise. The observed torque ripples because of irregular magnetic field of PM. Up to now, it is assumed the rotor and translator PM are aligned i.e zero displacement between their corresponding magnetic poles.

4.4 Thrust Force Displacement Dependency

Simulation Test 4 is similar to Test 3, except that here the translator initial displacement is set. This means the translator undergoes a forced simulation condition by setting this initial displacement for it to generate thrust force. This confirms that displacement between rotor and translator

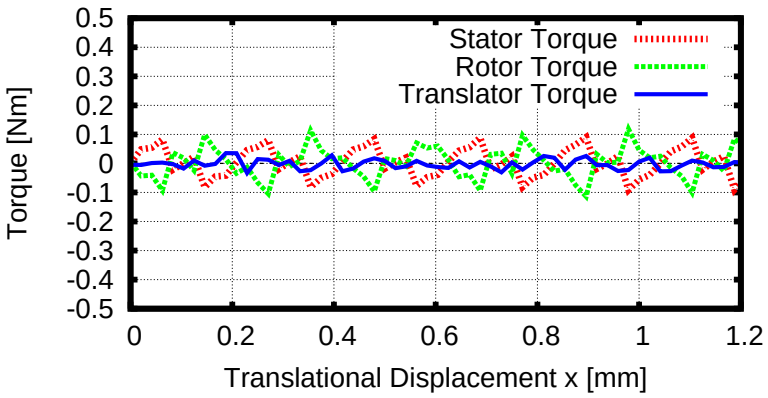

(a) Torque Analysis

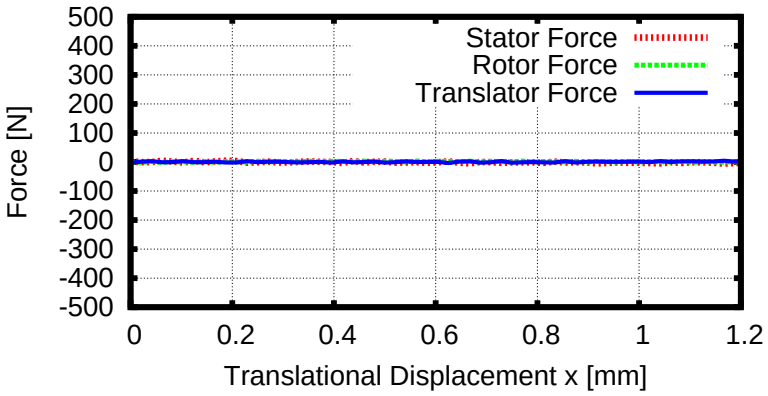

(b) Thrust Force Analysis

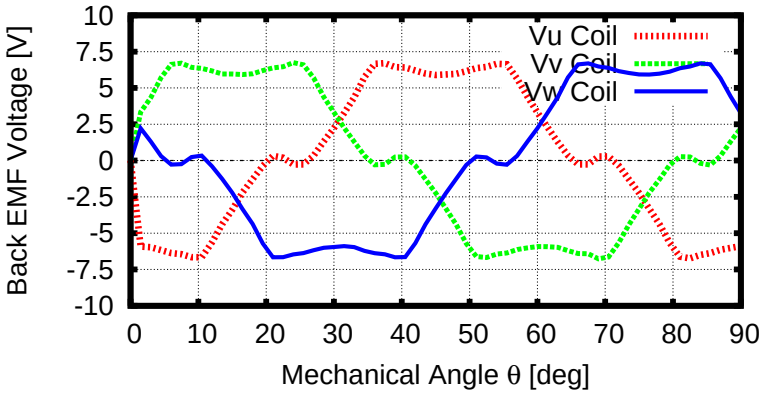

(c) Back-EMF voltage

Figure 4.3: 3-D FEA Simulation Test 2 [1800rpm, 0.15m/s, 0A]

PM poles is a requirement for generation of thrust force. This last is proportional to initial displacement. Fig. 4.6 shows 3-D FEA simulation results demonstrating the capability of such a system to transmit the Rotor torque forces to the Mover thrust forces and thus generating high

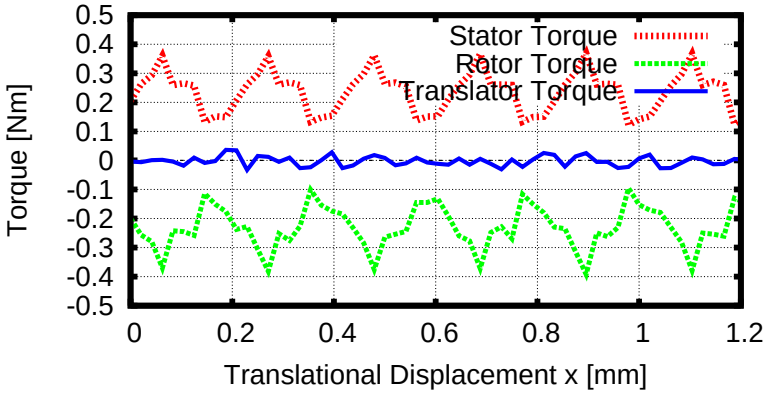

(a) Torque Analysis

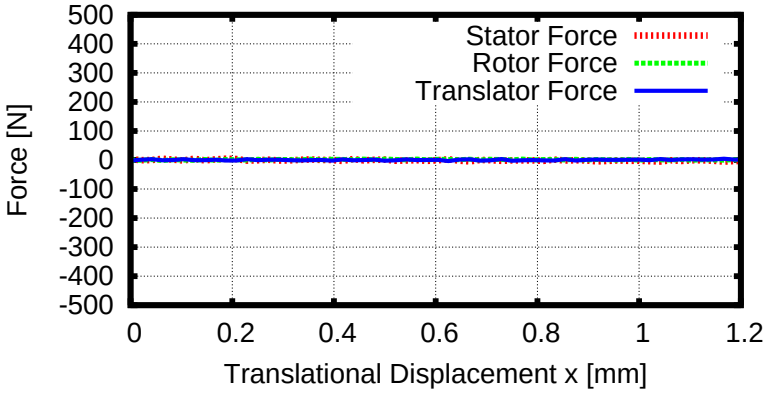

(b) Thrust Force Analysis

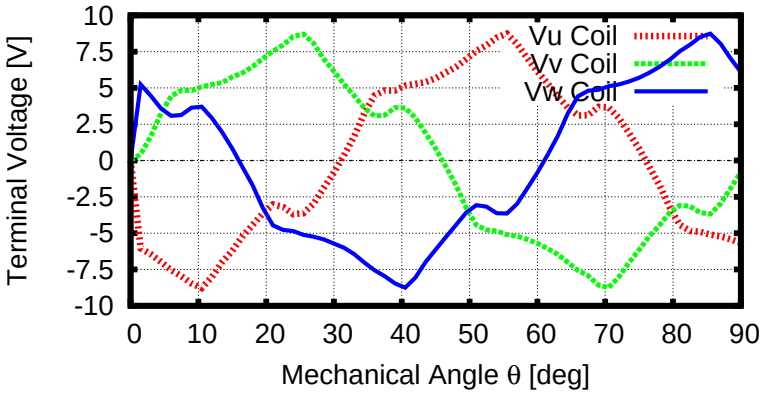

(c) Terminal voltage

Figure 4.4: 3-D FEA Simulation Test 3 [1800rpm, 0.15m/s, 5A]

thrust forces of around $220N$ under proper adjustment of $0.25mm$ initial displacement. Consequently, the stator is subjected to an anti-torque while the rotor is subjected to a reaction force as visualized in Fig. 4.6(a) and (b) respectively. According to equation (3.10), normally the

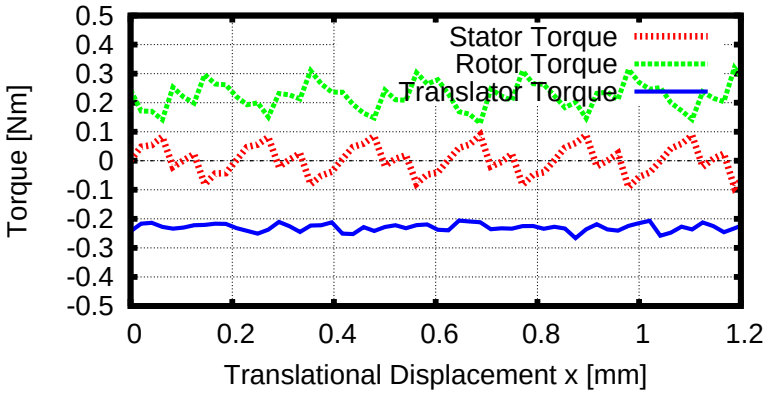

(a) Torque Analysis

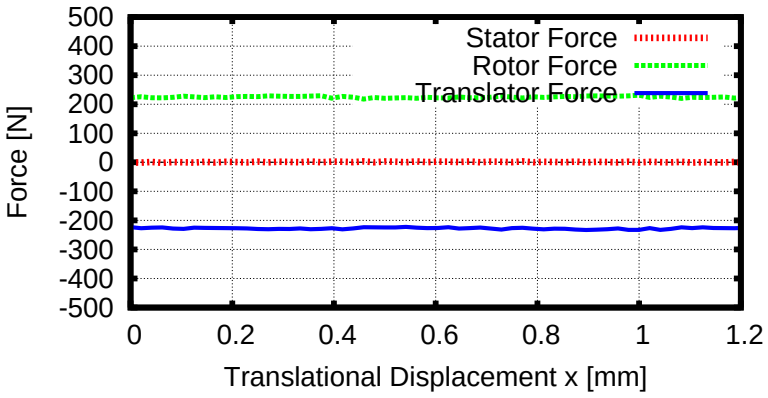

(b) Thrust Force Analysis

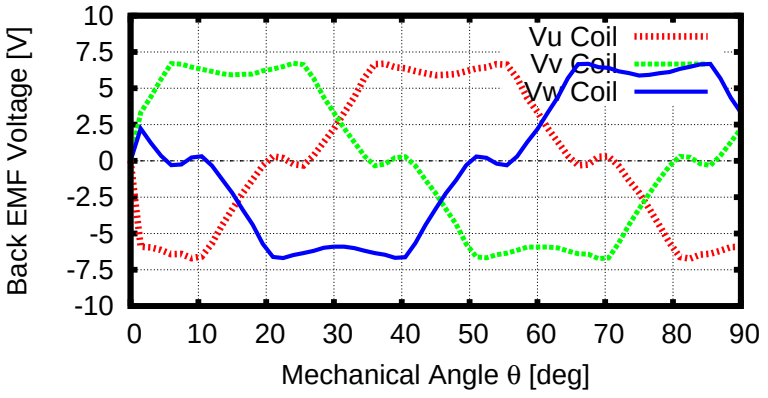

(c) Back-EMF voltage

Figure 4.5: 3-D FEA Simulation Test 4 [1800rpm, 0.15m/s, 0A, Displacement of 0.25mm]

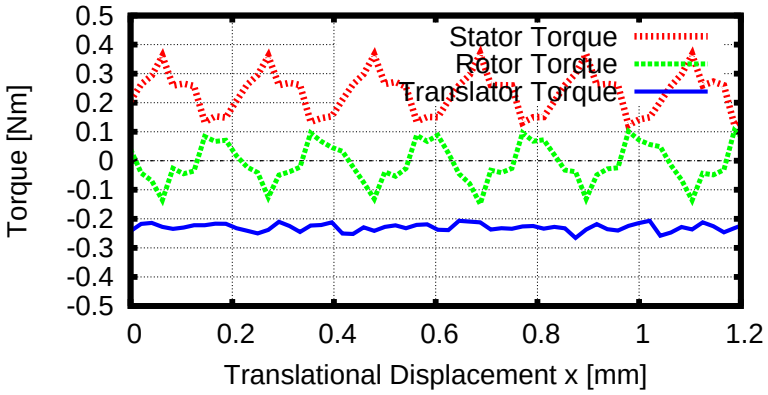

(a) Torque Analysis

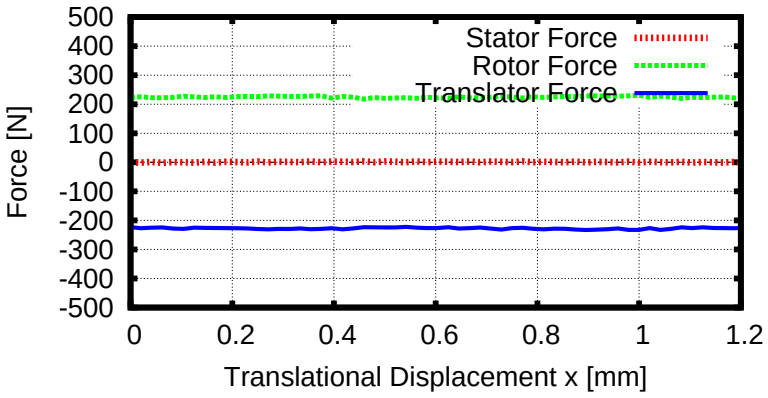

(b) Thrust Force Analysis

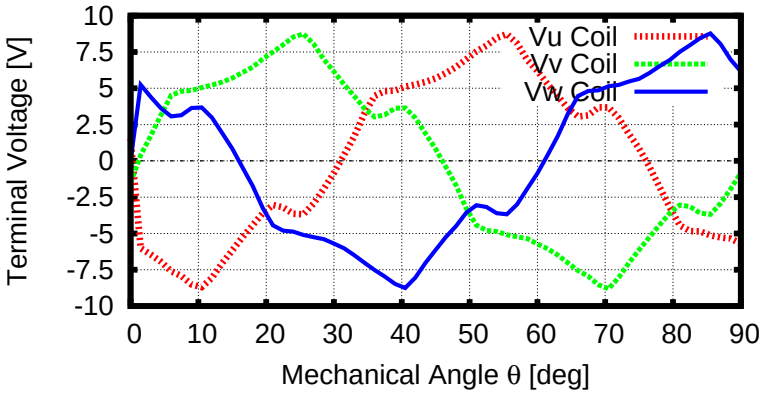

(c) Terminal voltage

Figure 4.6: 3-D FEA Simulation Test 5 [1800rpm, 0.15m/s, 5A, Displacement of 0.25mm]

torque ripples should be transmitted to force, but in this simulation, displacement between rotor and translator was kept constant. Consequently, the force of the translator is affected by this displacement. Reason why the force is almost constant due to this simulation condition of the displacement.

4.5 Summary

In this chapter, simulations based on 3-D Finite Element Analyses (FEA) transient electromagnetic studies for the prediction of thrust forces were discussed on and relevant results were presented as prerequisites of experimental prototype development. FEA based simulations were conducted in many steps in order to end up with optimal and reliable results.

Chapter 5

Prototype Implementation of *RotLin* Helical Machine

An experimental prototype model was developed and preliminary experiments were conducted in order to validate the direct-drive characteristics of *RotLin*. The Translator and Mid-Layer Rotor are coupled via magnetic spring. This is a two-inertia system (Series Elastic Actuator) and the linear position of the Translator is almost proportional to rotational angle of the Mid-Layer Rotor. Fig. 5.1 depicts the said experimental prototype. One inverter is used to provide three-phase currents to the stator coils; rotary encoder, linear encoder and controller for the direct-drive of this machine as shown in Fig. 5.1(b) and in Fig. 7.13 the equivalent circuit diagram is depicted.

5.1 Stator Part

5.1.1 Stator Core and Coil Winding

In this section, the stator core insulation and coil winding procedures are summarized. 3D printer was used to make the core insulation and thereafter a 0.8*mm* diameter copper wire was selected to make the three phase coils of 30 turns each. The slot fill factor was precalculated, in both *JMAG Express* simulations and calculations, to be of 16% per each slot. Fig. 5.2 depicts all procedures in just one picture.

5.1.2 Shell Manufacturing

The shell or frame structure to house the stator and the rotor was manufacturerd using *CNC Modeling Machine*. It consists of left and right flanges. The material used is non-heat treated aluminum-magnesium alloy A5052P. Fig. 5.3 portrays the overview of manufacturing processes.

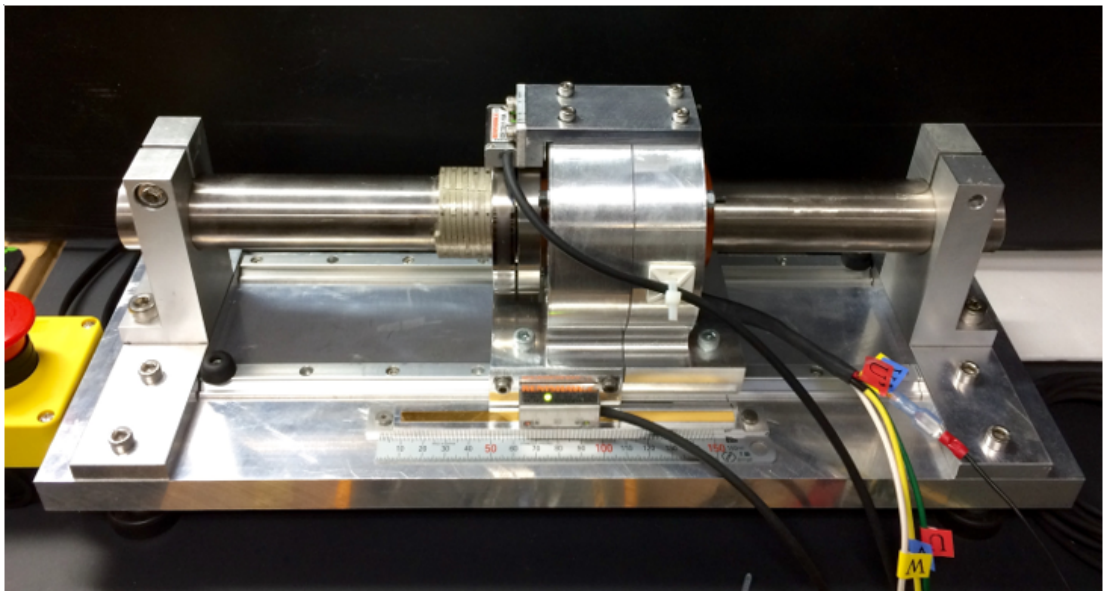

(a) 3D Lateral View of Implemented Prototype

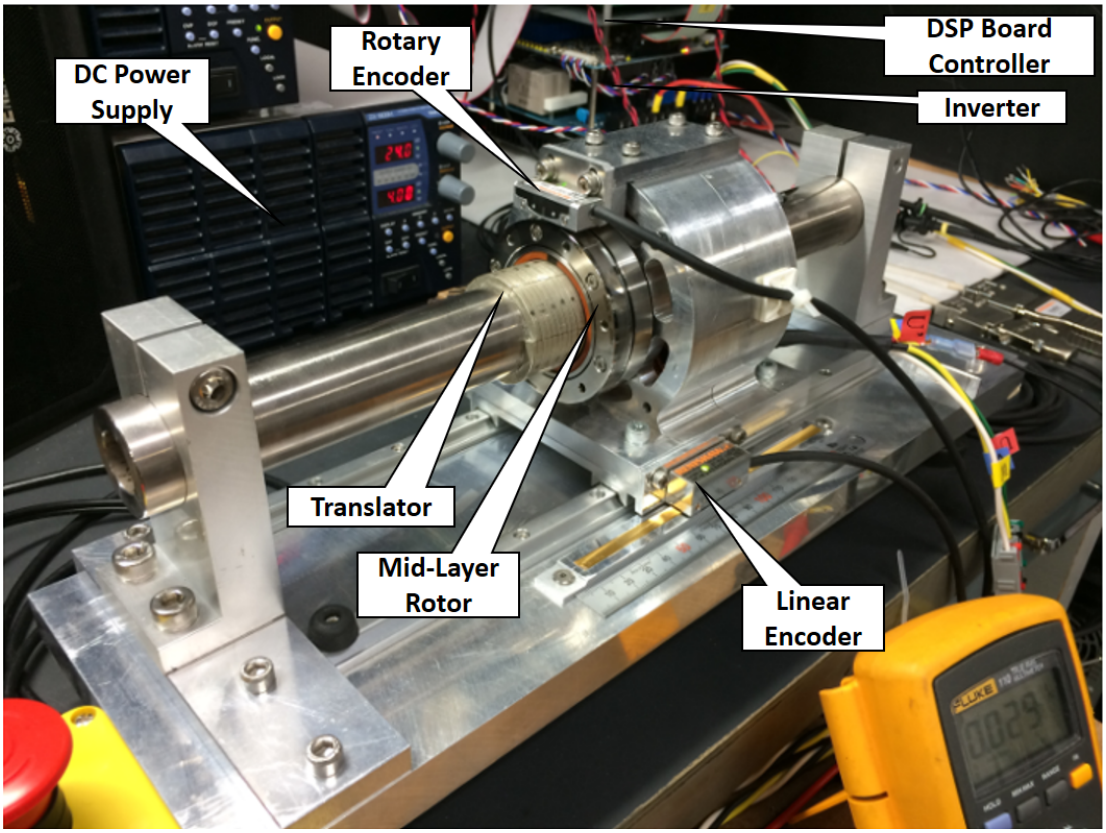

(b) Prototype Perspective View

Figure 5.1: Manufactured Prototype - Radial Gap Helical *RotLin* machine

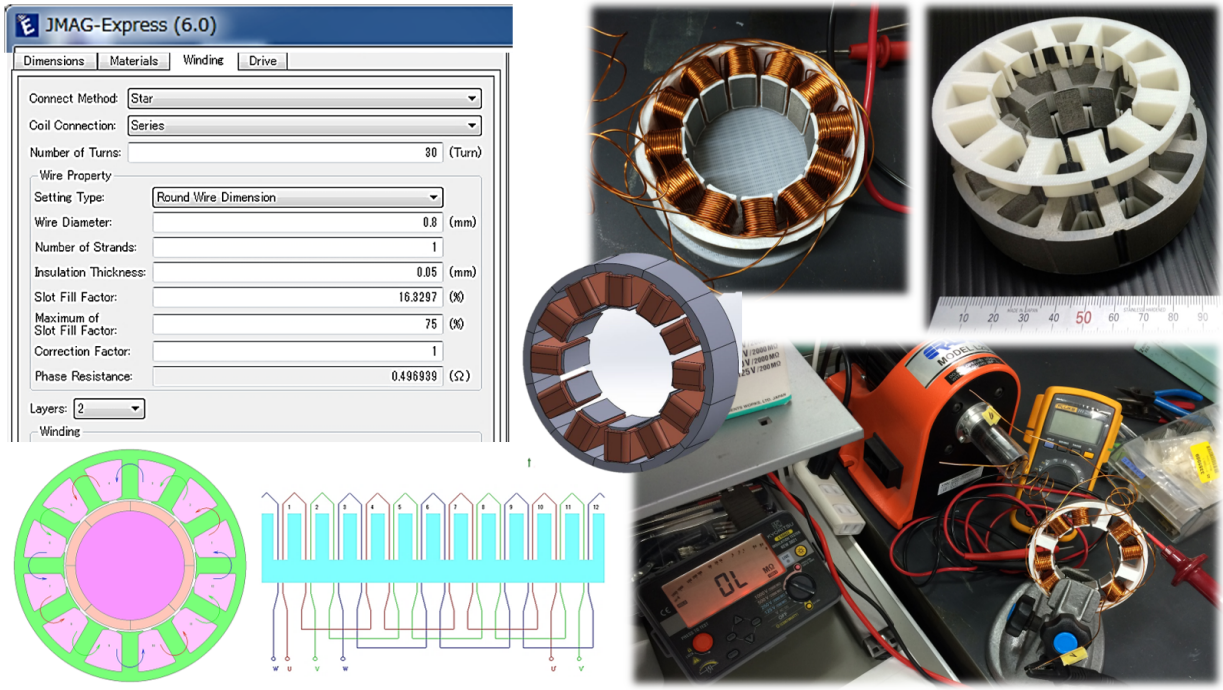

Figure 5.2: *RotLin*'s Stator Coil Winding

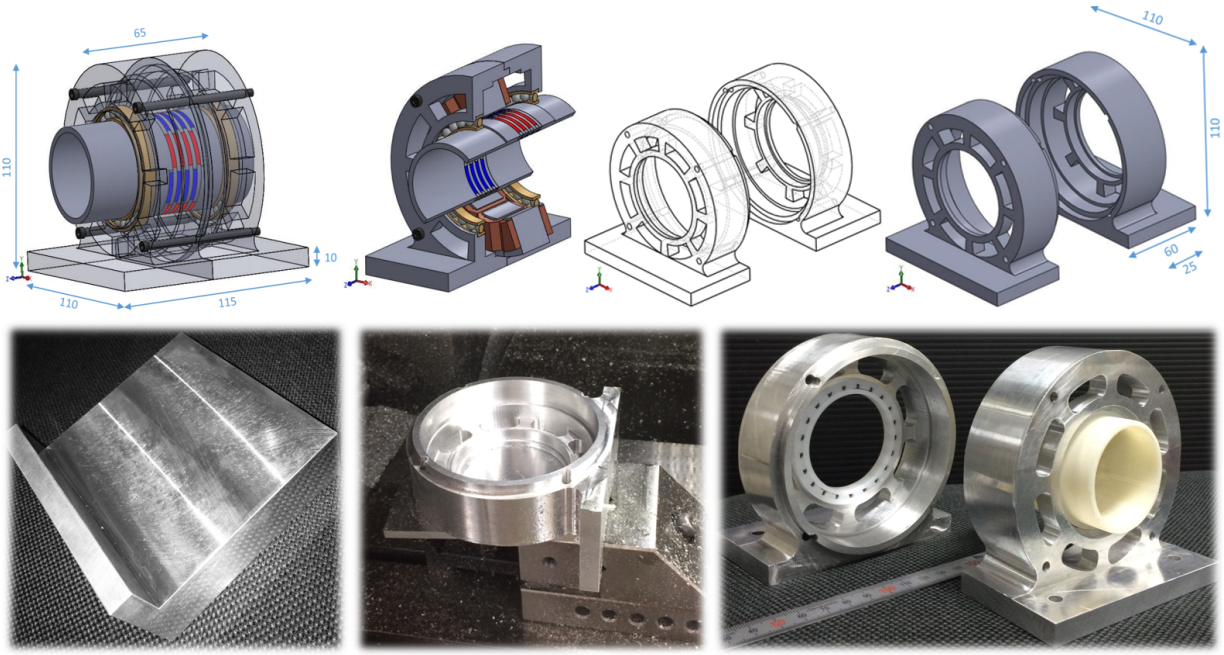

Figure 5.3: *RotLin*'s Shell Manufacturing

5.2 Mid-Layer / Rotor Part

The Rotor, now termed Mid-Layer part, is comprised of a nonmagnetic cylindrical frame in which are embedded the peicewise helical-shapped radially magnetized Permanent Magnets. These lasts appear on both inner and outer surfaces of the frame, and are able to interact simultaneously with the stator rotating magnetic field and translator helical magnets.

5.2.1 Peicewise Helical-Shaped Permanent Magnets

Smartly piecewise helical shaped $NdFeB$ Permanent Magnet (PM) that are radially magnetized and helically layered on Translator and helically embedded in Rotor frame. PM proposed topologies and the manufactured ones are shown in Fig. 5.4.

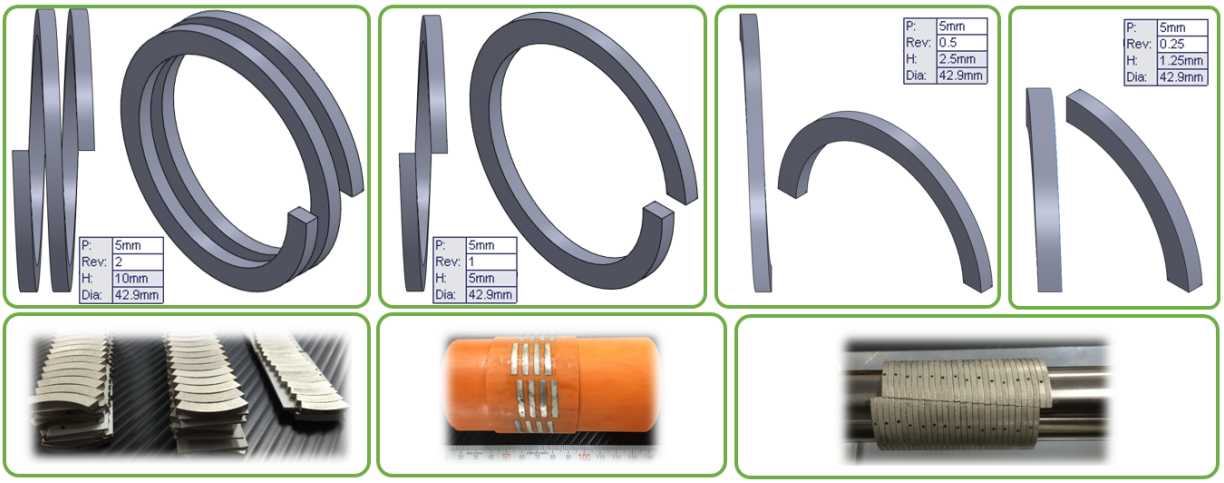

Figure 5.4: Peicewise Helical-Shaped PM design proposals

5.2.2 Rotor Frame Manufacturing Processes

In Fig. 5.5, the Rotor Frame with embedded Helical-Shaped PM is shown, its material is *Bakelite* and was processed using *CNC Modeling Machine* to cut the helical-shaped threads in which the corresponding PM were embedded and fastened using strong adhesive bonding.

5.3 Translator / Mover Part

By layering peicewise helical shaped PM and fastening them using strong adhesive bond on a steel stainless shaft, the translator seen in Fig. 5.6 was implemented.

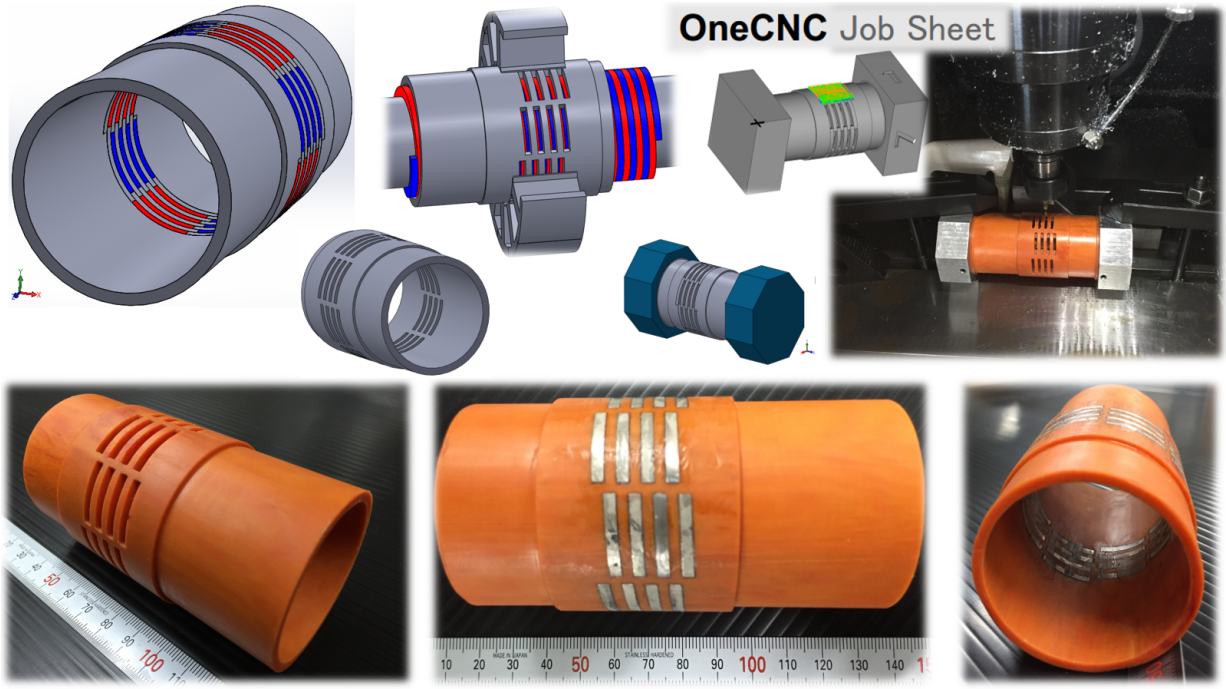

Figure 5.5: Rotor Frame with Embedded Helical-Shaped PM Manufacturing

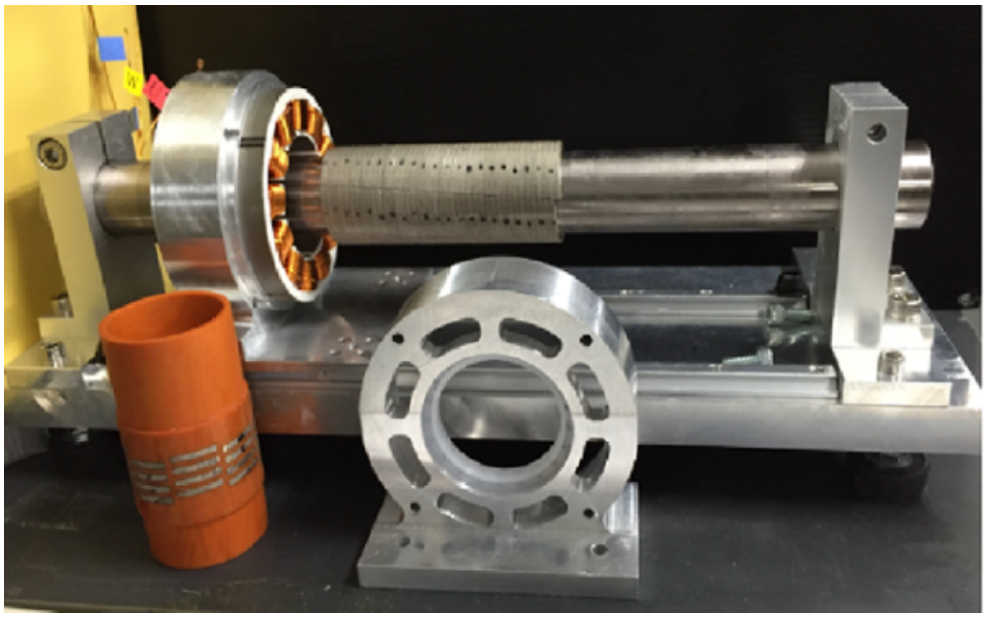

Figure 5.6: Manufactured Prototype Parts - Radial Gap Helical *RotLin* machine

5.4 Summary

In this chapter, procedures and steps of how the experimental prototype was developped are highlighted and explained. Most of the parts were developed, processed and manufactured from row materials by the authors of this thesis and the production can be estimated to 99% leaving the 1% to unpredicted manufacturing errors.

Chapter 6

Parameter Identification of *RotLin* Helical Machine

6.1 Coil Resistance and Inductance Measurements

Precise measurements of inductances are necessary for a better control of the motor. LCR meter at various frequency settings was used to measure the coil resistances and inductances for all three phases. Next, the actual measured values were compared to the ones from FEA analyses in *JMAG Designer* and found out to be almost the same (See Fig. 6.1).

6.2 Inherent Back-EMF Measurements

Back-EMF is among the key characteristics of a rotating electrical machine in order to derive its relative rotational speed. In this regard, the measured back-emf voltage is directly proportional to its angular velocity and may be used in motion control algorithms to modulate velocity. As carried out in [34], oscilloscopes recordings (see Fig. 6.2) show the back-emf of $7.52V$ phase voltages from intrinsic backdrivability i.e the moving part is pushed linearly and as a reaction the rotor rotates spirally following the pitch. Consequently, back-EMF voltages are measured across stator coil terminals. Proportionally, the waveform period estimates a speed of about $1,875rpm$ which is in close agreement with the simulation results where almost the same voltage at $1,800rpm$ is obtained. The model's back-EMF is represented by the term $-p\dot{\theta}\Psi$ in equation (3.3).

6.3 Simulated, Estimated vs. Measured Forces

A high-bandwidth Piezoelectric Force Sensor *(KISTLER Type 9301B), connected to Charge Meter Amplifier *(KISTLER Type 5015), was mounted to the system in order to measure the thrust force and compare it to the estimated force computed from rotary and linear encorders

JMAG Calculations

[Coil Inductance Calculation] FEM Coil			
ID	Coil	Resistance [ohm]	# of Turns [turn]
1	U	3.50E-01	3.000e + 001
2	V	3.50E-01	3.000e + 001
3	W	3.50E-01	3.000e + 001

[Coil Inductance Calculation] Calculation Results		
Output Items	Max Value [H]	Min Value [H]
L11 [H]	5.379E-04	5.379E-04
L22 [H]	5.385E-04	5.385E-04
L33 [H]	5.380E-04	5.380E-04
M21 [H]	-2.136E-04	-2.136E-04
M32 [H]	-2.141E-04	-2.141E-04
M13 [H]	-2.133E-04	-2.133E-04
M12 [H]	-2.133E-04	-2.133E-04
M23 [H]	-2.135E-04	-2.135E-04
M31 [H]	-2.134E-04	-2.134E-04

Measurements

[Measured Values] Coil			
ID	Coil	Resistance [ohm]	Inductance [H]
1	U	0.3443	5.369E-04
2	V	0.3402	5.347E-04
3	W	0.3495	5.355E-04

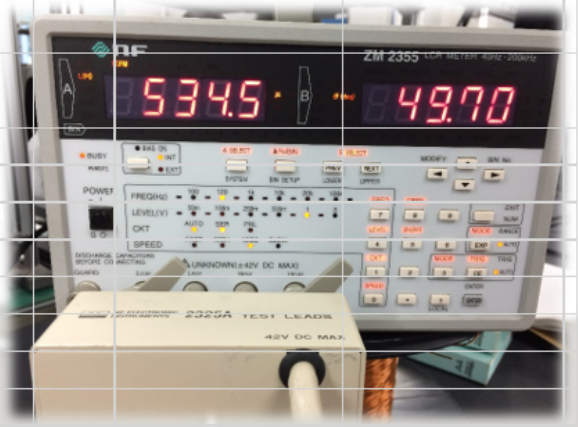

Figure 6.1: Coil Resistances and Inductances Measurements and Calculations

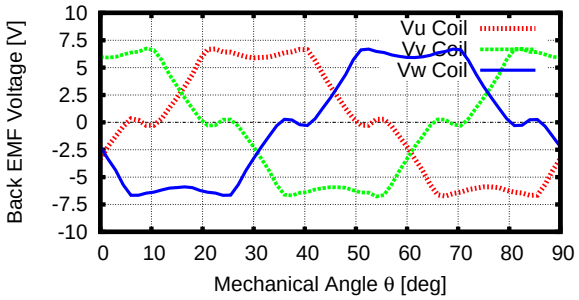

(a) FEA Back-EMF

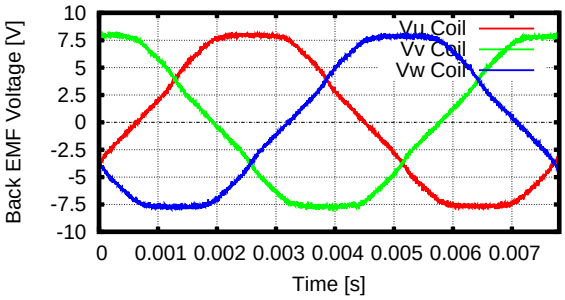

(b) Measured Back-EMF

Figure 6.2: *RotLin*'s Inherent Back-EMF measurement

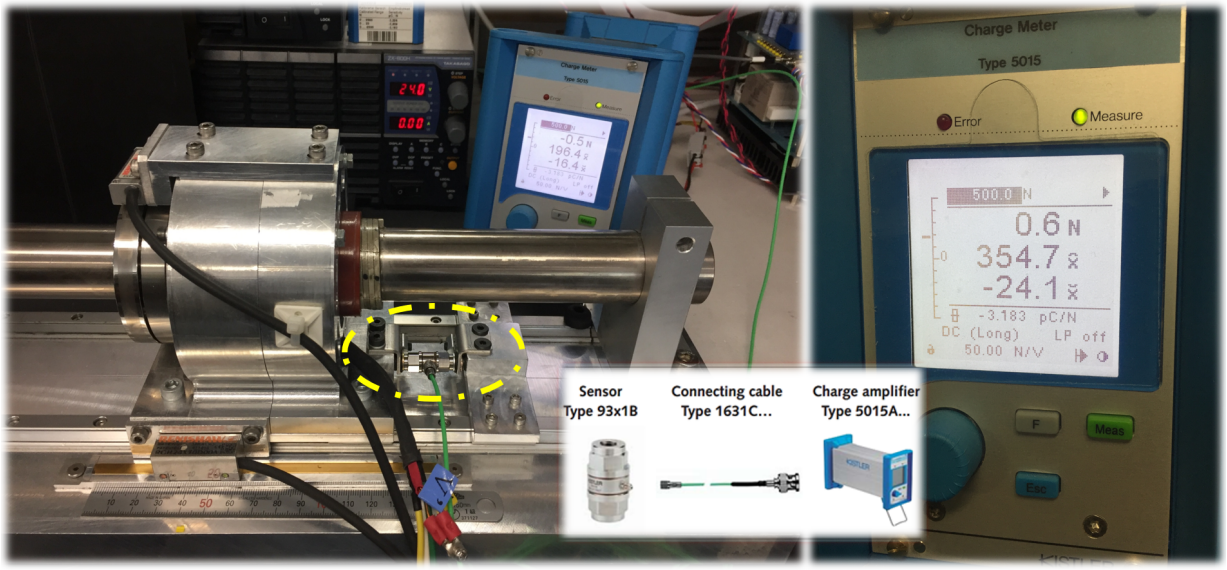

Figure 6.3: Force sensor installation

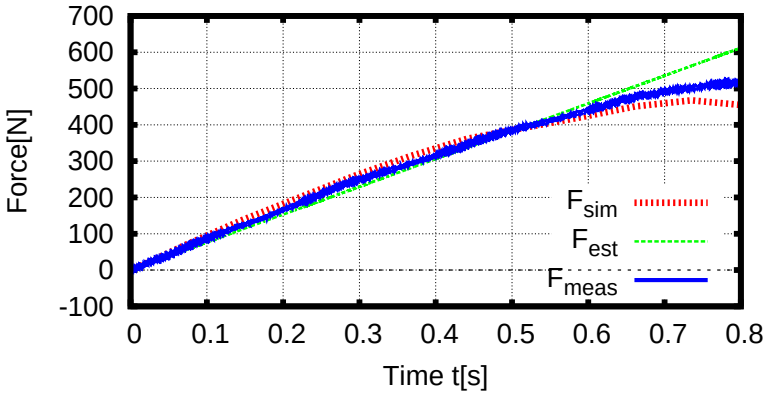

Figure 6.4: Estimated, Simulated and Measured Thrust Forces

information using equation (3.6). See Fig. 6.4 graph for results. Substantially linear Spring Constant characteristic $K_s = 850kN/m$ is identified.

6.4 Summary

In this chapter, parameter identifications through measurements and simulations were discussed on.

Chapter 7

Drive Control Tests of *RotLin* Helical Machine

In this chapter, various control schemes that have been so far applied to the implemented prototype in simulations and experiments are thouroughly highlighted and at the end compared. The proposed control is applied to helical motor model (3.2)-(3.5). Table 7.2 shows the plant and control parameters. The overall control block diagram is depicted in Fig. 7.12.

7.1 Controller Design Framework of Linear Motor

In this section, analogy from controlling the position of a linear motor by PD *(Proportional-Derivative) Controller and compensating the disturbance using DOb *(Disturbance Observer) is summarized.

7.1.1 Modeling of Linear Motor

Fig. 7.1 shows the plant model of a linear motor. Here, in order to have a rigorous control design, a rigorous model that allows the plant to work and a control model that will be used by the controller to control the plant, is derived. The model equations for the strict model are given as follows.

$$M\ddot{x} + D\dot{x} = F_m - F_{dis} \tag{7.1}$$

$$F_m = K_t I_a \tag{7.2}$$

Assuming that the frictional resistance of the linear motor is sufficiently small, the following model is used.

$$M\ddot{x} = F_m - F_{dis} \tag{7.3}$$

$$F_m = K_t I_a \tag{7.4}$$

The Table 7.1 shows Linear Motor system parameters. F_{dis} includes clutch frictions and forces that result from nominal errors.

Table 7.1: Parameters of Linear Motor

Nomenclature	Description
M [kg]	Translator/Mover Mass - Actual Value
M_n [kg]	Translator/Mover Mass - Nominal Value
D [-]	Viscous Frictions - Actual Value
F_m [N]	Translator/Mover Thrust Force
F_{dis} [N]	Disturbance Force
K_t [N/A]	Thrust Force Constant
K_{tn} [N/A]	Nominal Thrust Force Constant
I_a [A]	Armature Current

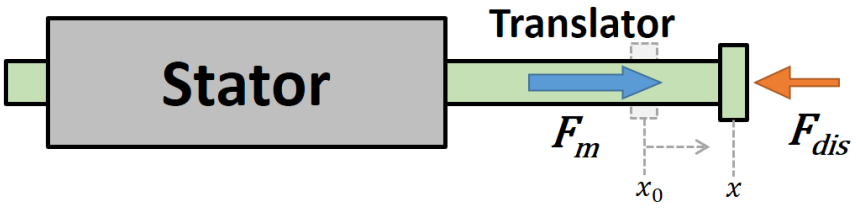

(a) Linear Motor

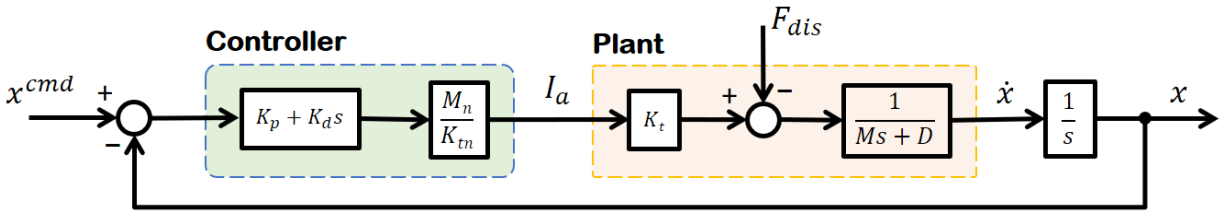

(b) Block Diagram of Closed-Loop of Linear Motor & PD Controller

Figure 7.1: Linear Motor

7.1.2 Controller Design of Linear Motor

PD controller is designed using proportional gain K_p and differential gain K_d. In equations (7.3) and (7.4) only I_a can be arbitrarily manipulated. In the case I_a is determined by the feedback of x and $\dot{x}$, according to the PD control, it becomes:

$$I_a = K_p(x^{cmd} - x) + K_d(\dot{x}^{cmd} - \dot{x}) \tag{7.5}$$

However, to simplify analysis, I_a will be given by the following expression.

$$I_a = \frac{M_n}{K_{tn}}\left[K_p(x^{cmd} - x) + K_d(\dot{x}^{cmd} - \dot{x})\right] \tag{7.6}$$

The block diagram of this control structure is shown in Fig. 7.1(b).

7.1.3 Simulation Program of the Controller Structure

As a prerequisite for simulation, it sometimes handles things in discrete time. Therefore, it is often said that, by making the sampling time small enough and devising a simulation method, the same thing can be said for discrete time and continuous time. In addition, since a PC and microcomputer board *(microcontroller) are used to control the motor and robot, control time also becomes discrete because there are calculation time and other factors.

Therefore, by separating the real-time sampling time Δt and the controller calculation time's sampling time $\Delta t_{control}$, it is possible to simulate in a more realistic environment (see Fig. 7.2). However, $\Delta t_{control} > \Delta t$ is always true, and then $\Delta t_{control}$ is determined by the performance of the computer and DSP *(Digital Signal Processor). In the case of robots, it is in the order of $[msec] \sim [\mu sec]$, in the case of motors and the like, it is in the order of $[\mu sec] \sim [nsec]$. A sample program to run the plant function and the controller function at different sampling times is shown in Appendix A.

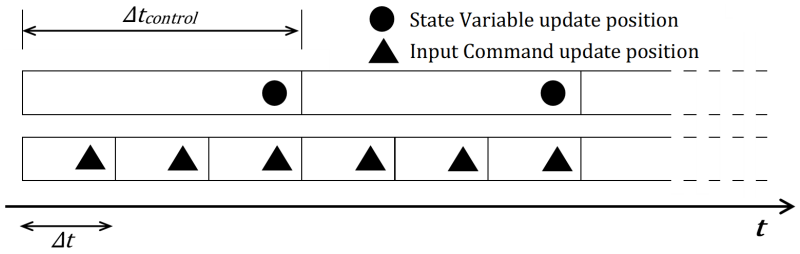

Figure 7.2: Timeline of Control Sampling Time

(a) Linear Motor Plant State Variables

In the plant function, there is a part that simulates the actual operation of motor, robot, etc. Specifically, the next state variables ($x[t+1], \dot{x}[t+1]$) are obtained from the input determined in the controller (For example, I_a) and the current state variables ($x[t], \dot{x}[t]$). When the state variable is $[x, \dot{x}]^t$, from equations (7.1) and (7.2), the state equation is given by

$$\frac{d}{dt}\begin{bmatrix} x \\ \dot{x} \end{bmatrix} = \begin{bmatrix} 0 & 1 \\ 0 & -D/M \end{bmatrix}\begin{bmatrix} x \\ \dot{x} \end{bmatrix} + \begin{bmatrix} 0 \\ K_t/M \end{bmatrix} I_a + \begin{bmatrix} 0 \\ -F_{dis}/M \end{bmatrix} \tag{7.7}$$

The next state $[x[t+1], \dot{x}[t+1]]^2$ can be obtained by solving the previous differential equation (7.7). Methods like the **Euler method** and **Runge-Kutta method** exist to solve differential equations. Detailed explanation of each method will be left to be read in specialized technical books. When implementing a plant function in a simulation, examples of input/output variables are the state variables ($x[t], \dot{x}[t]$), input I_a, elapsed time t *(disturbance can be added at an arbitrary time) as input, and the next state variables ($x[t+1], \dot{x}[t+1]$) as intended output variables.

(b) Derivation of the new state variable by Euler's method

First, solve equation (7.7) to find $\frac{d}{dt}[x[t], \dot{x}[t]]^t$. Then, from the integration definition, $[x[t+1], \dot{x}[t+1]]^t$ is obtained as:

$$\begin{bmatrix} x\,[t+1] \\ \dot{x}\,[t+1] \end{bmatrix} = \begin{bmatrix} x\,[t] \\ \dot{x}\,[t] \end{bmatrix} + \frac{d}{dt}\begin{bmatrix} x \\ \dot{x} \end{bmatrix}\Delta t \tag{7.8}$$

Here, there are other integration methods that can be applied, such as trapezoidal integration, so use an appropiate method. Eulers method accuracy is not very good, but since it is simple, its advantage is its high speed computations.

(c) Controller Function

The controller function, simulating the microcontroller board and PC, has a part that calculates the torque and voltage given by the the linear motors plant *(In the example is the current I_a). In fact, when implementing the controller function in a simulation, the following examples of input and output variables, for inputs there are: state variables ($x[t], \dot{x}[t]$), elapsed time t *(disturbance can be added at any time), and I_a as an input to the plant.

(d) Simulation Results (PD control)

The nominal values are equivalent to actual plant values. Under the condition that $\dot{x}^{cmd} = 0$, the Transfer Function from x to $\dot{x}^{cmd}$ is expressed by

$$\frac{X}{X^{cmd}} = \frac{K_p}{s^2 + K_d s + K_p} \tag{7.9}$$

Here, the transfer function of the secondary system response uses the damping constant ζ and the vibration frequency ω_n, and it becomes:

$$G(s) = \frac{\omega_n^2}{s^2 + 2\omega_n\zeta s + \omega_n^2} \tag{7.10}$$

Comparing (7.9) and (7.10), the following relationships are obtained.

$$\omega_n = \sqrt{K_p} \tag{7.11}$$
$$K_d = 2\sqrt{K_p}\zeta \tag{7.12}$$

Therefore, when K_p and ζ have been decided, K_d is determined. Fig. 7.3 shows the differences in response due to ζ variations.

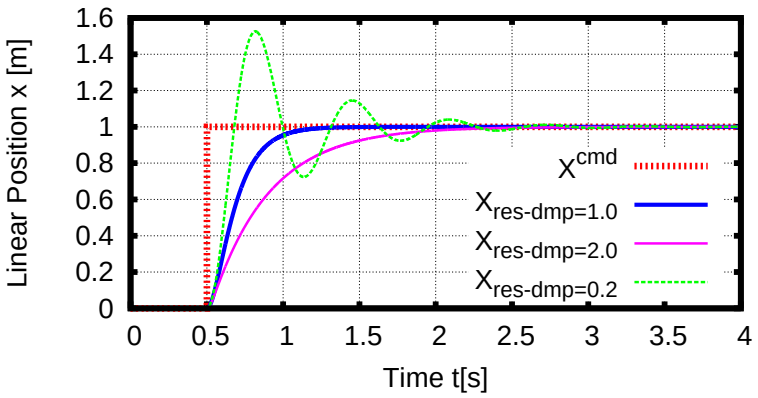

Figure 7.3: Linear Motor + PD Controller with Damping Variations

7.1.4 Disturbance Observer *(DOb) Calculations

Details of the DOb will be left to various professional journals. The DOb calculates motor's Thrust Force F_{m+} and Thrust Force F_{m-} of the motor calculated backwards, from the input I_a (generally u), and estimates the difference as a disturbance. From equations (7.3) and (7.4),

$$F_{m+} = K_{tn} I_a \tag{7.13}$$
$$F_{m-} = M_n \ddot{x} \tag{7.14}$$
$$F_{dis} = F_{m+} - F_{m-} = K_{tn} I_a - M_n \ddot{x} \tag{7.15}$$

Actually, it passes it through the filter *(cutoff frequency ω_{DOb}[rad/s]), drops the currents dimension and feeds it back to the current value.

$$\hat{F}_{dis} = \frac{\omega_{DOb}}{s + \omega_{DOb}} F_{dis} = \frac{\omega_{DOb}}{s + \omega_{DOb}} (K_{tn} I_a - M_n \ddot{x}) \tag{7.16}$$
$$I_{com} = \frac{\hat{F}_{dis}}{K_{tn}} = \frac{1}{K_{tn}} \frac{\omega_{DOb}}{s + \omega_{DOb}} (K_{tn} I_a - M_n \ddot{x}) \tag{7.17}$$

However, equation (7.17) contains second order derivative. Calculating this $\ddot{x}$ with a backward difference and pseudo-derivative is a cause for noise and a factor of band narrowing. Therefore, equation (7.17) can be transformed to the equivalent equation as follows.

$$I_{com} = \frac{1}{K_{tn}}\left(\frac{\omega_{DOb}}{s+\omega_{DOb}}K_{tn}I_a - \frac{\omega_{DOb}}{s+\omega_{DOb}}M_n \underbrace{sX(s)}_{Acceleration}\right) \tag{7.18}$$

$$= \frac{1}{K_{tn}}\left(\frac{\omega_{DOb}}{s+\omega_{DOb}}K_{tn}I_a - \frac{s}{s+\omega_{DOb}}M_n\omega_{DOb}\underbrace{X(s)}_{Speed}\right) \tag{7.19}$$

$$= \frac{1}{K_{tn}}\left(\frac{\omega_{DOb}}{s+\omega_{DOb}}K_{tn}I_a - \frac{s+\omega_{DOb}-\omega_{DOb}}{s+\omega_{DOb}}M_n\omega_{DOb}X(s)\right) \tag{7.20}$$

$$= \frac{1}{K_{tn}}\left(\frac{\omega_{DOb}}{s+\omega_{DOb}}K_{tn}I_a - \frac{s+\omega_{DOb}}{s+\omega_{DOb}}M_n\omega_{DOb}X(s) + \frac{\omega_{DOb}}{s+\omega_{DOb}}M_n\omega_{DOb}X(s)\right) \tag{7.21}$$

$$= \frac{1}{K_{tn}}\left[\frac{\omega_{DOb}}{s+\omega_{DOb}}\left(K_{tn}I_a + \frac{\omega_{DOb}}{s+\omega_{DOb}}M_n\omega_{DOb}X(s)\right) - M_n\omega_{DOb}X(s)\right] \tag{7.22}$$

Fig. 7.4 shows the overall block diagram including DOb.

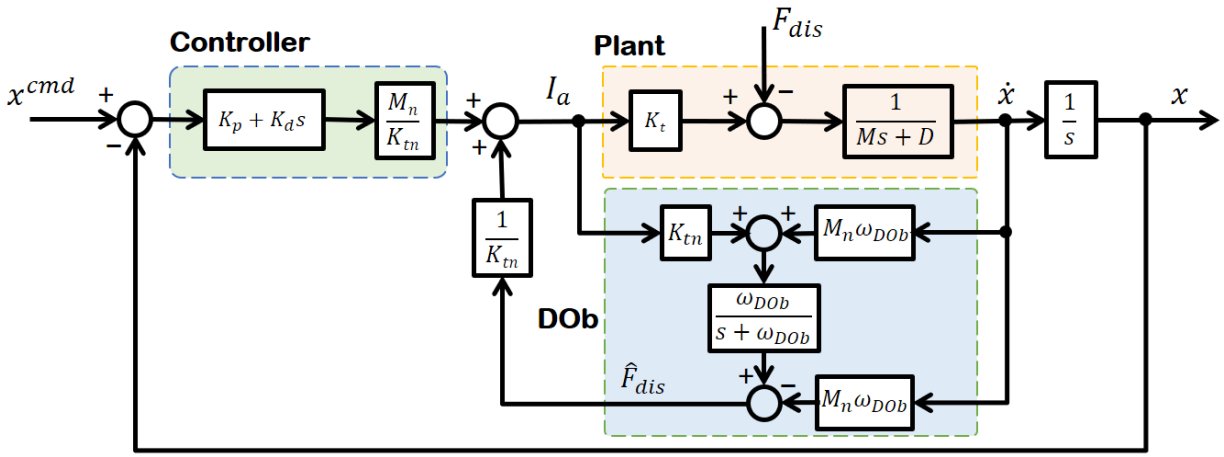

Figure 7.4: Linear Motor + PD Controller with DOb Block Diagram

(a) Development of First-Order Low-Pass Filter

The transfer function of the DOb's low pass filter *(Cutoff Frequency ω_c) is represented as follows.

$$\frac{Y}{X} = \frac{\omega_c}{s+\omega_c} \tag{7.23}$$

Transforming equation (7.23), it yields

$$Y = \frac{1}{s}\omega_c(X-Y) \tag{7.24}$$

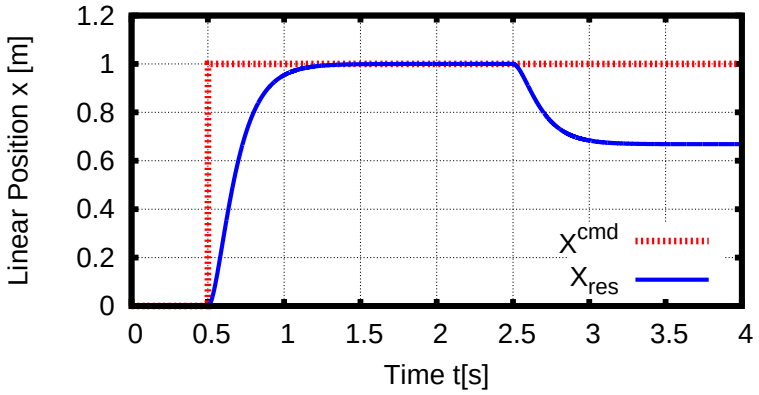

(a) Linear Position Response

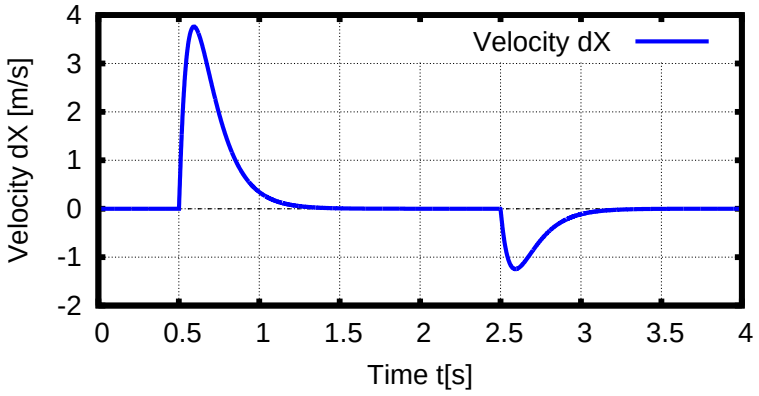

(b) Velocity Response

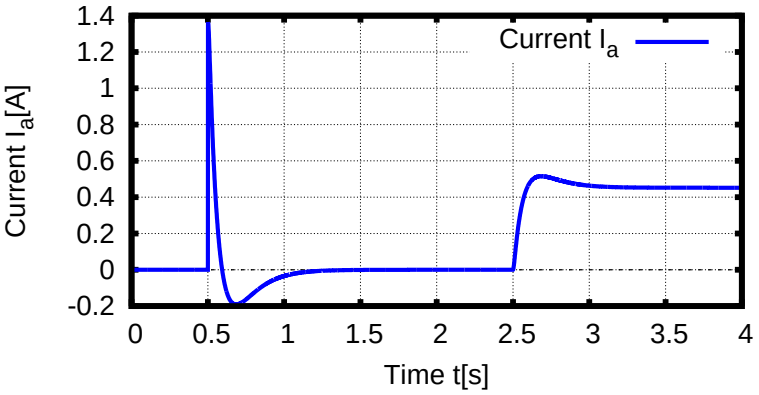

(c) Current Response

Figure 7.5: Effect of Disturbance on the PD Controlled Linear Motor

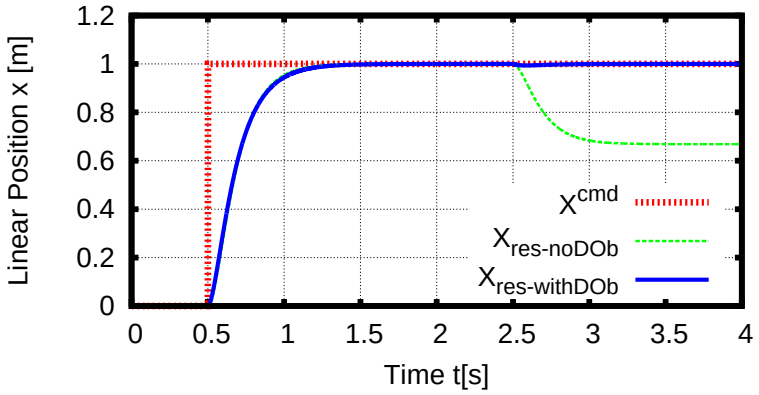

(a) Linear Position Response

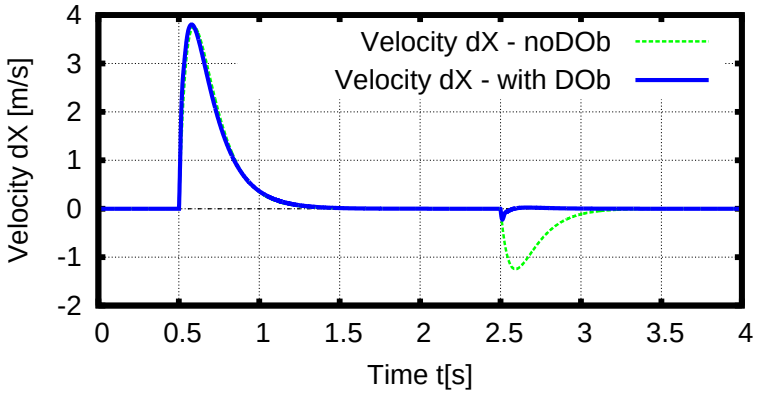

(b) Velocity Response

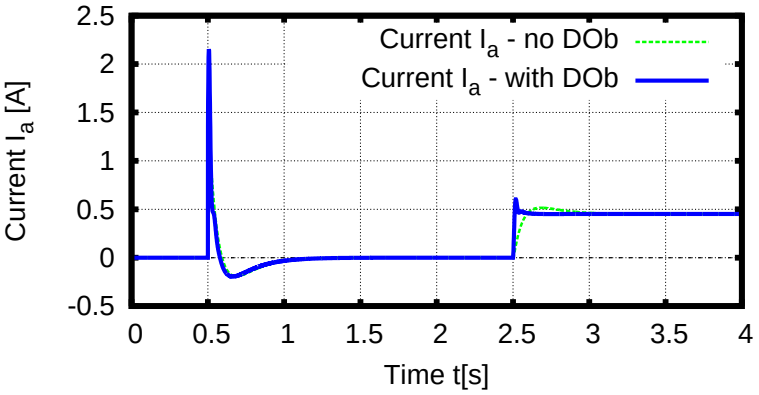

(c) Current Response

Figure 7.6: Disturbance Compensation on the PD Controlled Linear Motor using DOb

From (7.24), the following equation is obtained.

$$Y[t] = Y[t-1] + \omega_c(X[t] - Y[t-1])\Delta T \tag{7.25}$$

(b) Development of Pseudo-Derivative

When realizing classical control using Laplace operator s in a discrete system, such as a personal computer, it becomes possible by appropriately replacing s. Differential operator s in the Laplace space can be realized by backward difference, amongst others. Here, the pseudo differentiator, composed by integral operator $1/s$ and a low-pass filter is introduced.

The transfer function, which combines the differentiator and the low-pass filter,

$$\frac{Y}{X} = \frac{\omega_x}{s + \omega_x} s \tag{7.26}$$

Dividing the numerator and denominator by s, it becomes:

$$\frac{Y}{X} = \frac{\omega_x}{1 + \omega_x / s} s \tag{7.27}$$

Therefore,

$$Y = \omega_x X - \frac{\omega_x}{s} Y \tag{7.28}$$

A differentiator constructed by an integrator can be used. Fig. 7.7 shows the block diagram when a Pseudo-Differentiator is applied to the output position to get the speed.

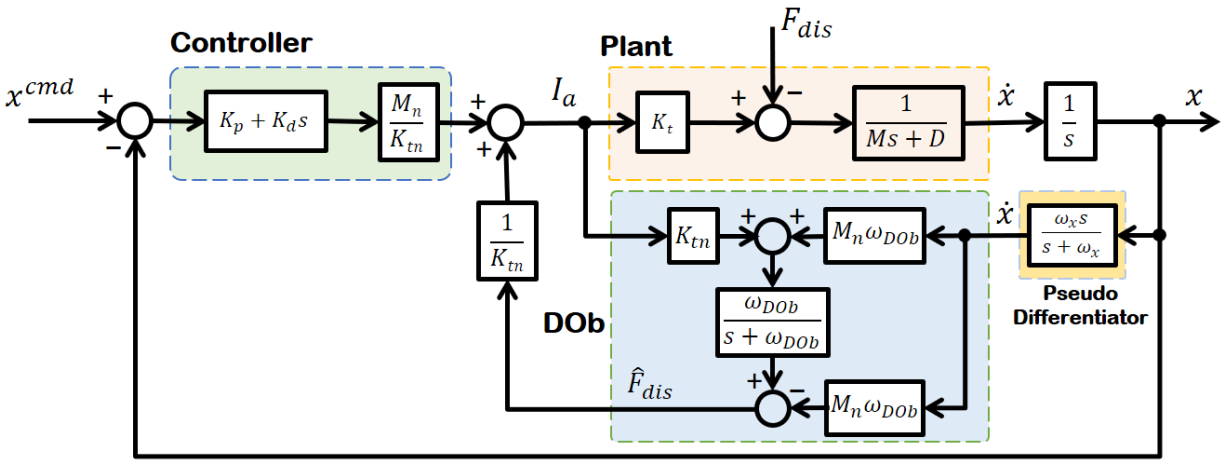

Figure 7.7: Linear Motor + PD Controller + DOb with Pseudo-Differentiator Block Diagram

(c) Development of Quantizer

Some sensors such as encoders take finite and discrete digital data. Therefore, to perform a strict simulation, it is necessary to quantize the data obtained from the sensor. In Appendix A, a sample program that quantizes 2π with 8 bits (256 levels) is shown.

7.2 Open Loop V/f Control

Knowing that the synchronous speed is proportional to the supply frequency by the relation $N_s = 120f/P$, the speed can be varied by just varying the frequency. Basically, the stator voltage was varied simultaneously with the supply frequency in a such a way the V/f ratio remained constant. This resulted in speed variations within the the operating frequency region which is from $2.5Hz$ to about $4.75Hz$ for a V_{rated} of around 12 Volts. Fig. 7.8 depicts and confirm the speed variation by varying the frequency of the supply leading also to voltage varying accordingly to keep the ratio constant.

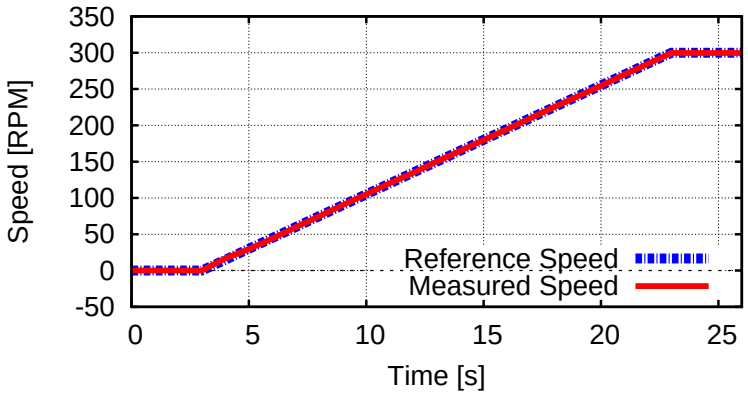

Figure 7.8: Open Loop V/f Control by varying Supply Frequency

7.3 State Space Formulation

In order to obtain a linear model that can be used for control design, the motion equations are linearized and represented by state space formulation.

$$\dot{x} = Ax + Bu + Hd \tag{7.29}$$

$$y = Cx + Du \tag{7.30}$$

Where y is the output vector, x is the state vector, and $u = -Kx$ is the input vector. In this regard, the motion equations (3.4) and (3.5) yield the following formulation:

$$\underbrace{\frac{d}{dt}\begin{bmatrix}\theta\\ \dot{\theta}\\ x\\ \dot{x}\end{bmatrix}}_{\dot{X}} = (A - BK)\underbrace{\begin{bmatrix}\theta\\ \dot{\theta}\\ x\\ \dot{x}\end{bmatrix}}_{X} + BK\underbrace{\begin{bmatrix}\theta^{cmd}\\ \dot{\theta}^{cmd}\\ x^{cmd}\\ \dot{x}^{cmd}\end{bmatrix}}_{X^{cmd}} + HF_{load} \tag{7.31}$$

Where constants A (dynamics), B (control distribution / gain), and H (disturbance) are matrices; and K is feedback matrix.

$$A = \begin{bmatrix} 0 & 1 & 0 & 0\\ \frac{-h^2K_s}{J} & 0 & \frac{-hK_s}{J} & 0\\ 0 & 0 & 0 & 1\\ \frac{-hK_s}{M} & 0 & \frac{-K_s}{M} & 0\end{bmatrix}; B = \begin{bmatrix}0\\ \frac{K_\tau}{J}\\ 0\\ 0\end{bmatrix}; H = \begin{bmatrix}0\\ 0\\ 0\\ \frac{-1}{M}\end{bmatrix} \tag{7.32}$$

$$K = \begin{bmatrix}K_{p\theta} & K_{d\theta} & K_{px} & K_{dx}\end{bmatrix} \tag{7.33}$$

Since the force is related to the position, the output of interest is the load-position and there is no direct coupling from input to output i.e. the output matrix C (sensor matrix) and the coupling matrix D are given by:

$$C = \begin{bmatrix}0 & 0 & 1 & 0\end{bmatrix}; D = 0 \tag{7.34}$$

In the Laplace domain, system equation (7.31) is described by:

$$[sI - (A - BK)]\,X(s) = BKX^{cmd}(s) + HF_{load} \tag{7.35}$$

$$Y(s) = CX(s) \tag{7.36}$$

The matrix transfer functions then can be derived in the following form.

$$X(s) = [sI - (A - BK)]^{-1}BKX^{cmd}(s) + [sI - (A - BK)]^{-1}HF_{load} \tag{7.37}$$

$$Y(s) = C\,[sI - (A - BK)]^{-1}BKX^{cmd}(s) + C\,[sI - (A - BK)]^{-1}HF_{load} \tag{7.38}$$

7.4 Servo System Control Design

In order to regulate the output of a dynamical system rom an arbitrary initial state by means of state feedback control, and because the plant exhibits oscillatory transient response, the Servo System Controller has been designed with the aim of minimizing the error almost to zero and suppress vibrations. In order to realize the stepwise tracking reference, the state space system is virtually extended *(refer to equation (7.39)) for the sake of designing integral type controller capable of mitigating the error, hence the control law in equation (7.40) is applied.

$$\frac{d}{dt}\begin{bmatrix}x(t)\\ z(t)\end{bmatrix} = \begin{bmatrix}A & 0\\ -C & 0\end{bmatrix}\begin{bmatrix}x(t)\\ e(t)\end{bmatrix} + \begin{bmatrix}B\\ 0\end{bmatrix}u(t) + \begin{bmatrix}0\\ I\end{bmatrix}r \tag{7.39}$$

$$u(t) = -Kx(t) + K_i\int_0^i e(t)dt \tag{7.40}$$

Where $e(t) = r - y(t)$ is the error and $y(t) = Cx(t)$ is the output. The $r(t)$ is the reference signal or setpoint that the servo output $y(t)$ is required to follow. The virtually extended system has new matrices $\tilde{A}$ and $\tilde{B}$ represented as follows.

$$\tilde{A} = \begin{bmatrix} A & 0 \\ -C & 0 \end{bmatrix} = \begin{bmatrix} 0 & 1 & 0 & 0 & 0 \\ \frac{-h^2 K_s}{J} & 0 & \frac{-hK_s}{J} & 0 & 0 \\ 0 & 0 & 0 & 1 & 0 \\ \frac{-hK_s}{M} & 0 & \frac{-K_s}{M} & 0 & 0 \\ 0 & 0 & -1 & 0 & 0 \end{bmatrix} \tag{7.41}$$

$$\tilde{B} = \begin{bmatrix} B \\ 0 \end{bmatrix} = \begin{bmatrix} 0 \\ \frac{K_\tau}{J} \\ 0 \\ 0 \\ 0 \end{bmatrix} \tag{7.42}$$

These matrices are used to compute the feedback gains corresponding to the faster and stable system. With state feedback, the closed loop response of the system can be selected by combining the control law with the state space model and selecting the state feedback gain K to give desirable closed loop poles which in turn give a desired transient response. Fig. 7.11 shows simulation results of an ideal system i.e when any disturbance is ignored; it is therefore possible to fastly achieve steady state response and thus mitigate the error to zero. Feedback gains represented by matrix K and integral gain K_i are designed by using Ackermann's pole placement algorithm as observed in Fig. 7.10 where the bode diagram and step response of different selected poles are depicted for optimal stability.

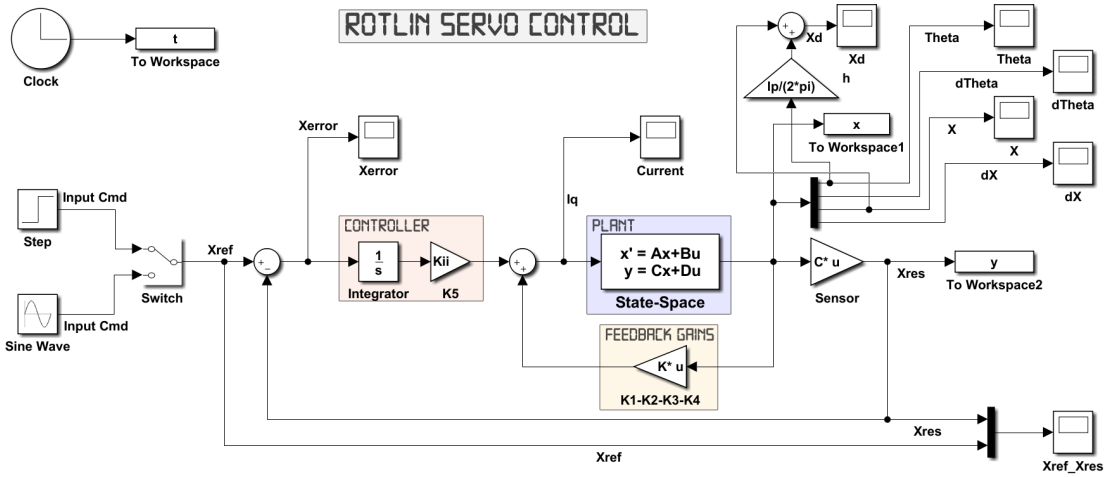

Figure 7.9: *RotLin* Servo Control Block Diagram

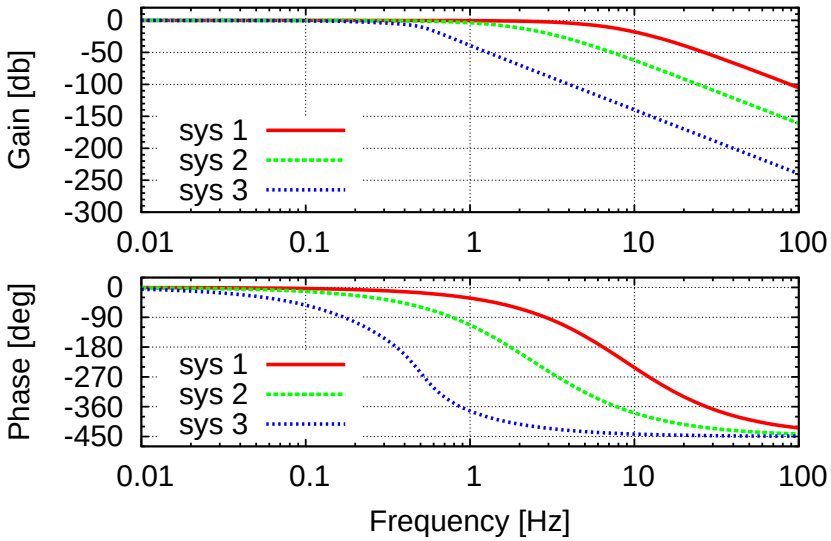

(a) Pole Placement Bode Diagram

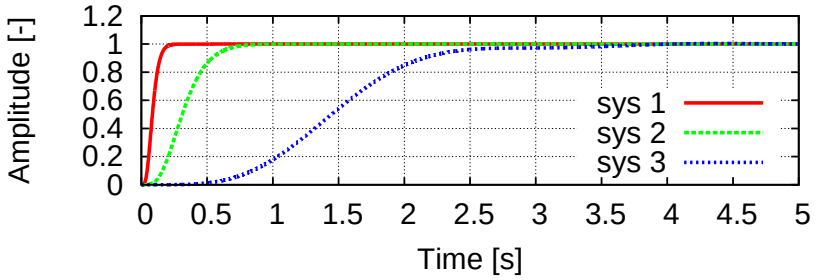

(b) Pole Placement Step Responses

Figure 7.10: Servo Control Pole Placement Stability Analysis

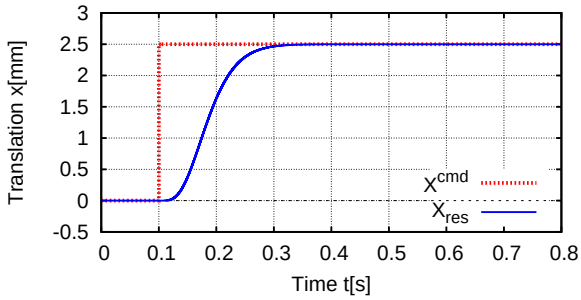

(a) Linear Position response x in mm

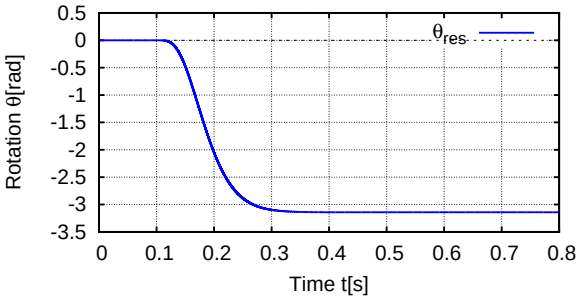

(b) Rotary Position response θ in rad

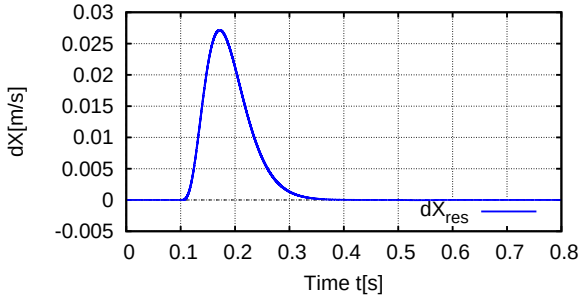

(c) Linear Velocity response $\dot{x}$ in m/s

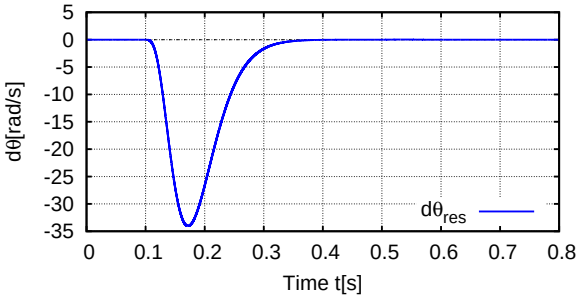

(d) Rotary Velocity response $\dot{\theta}$ in rad/s

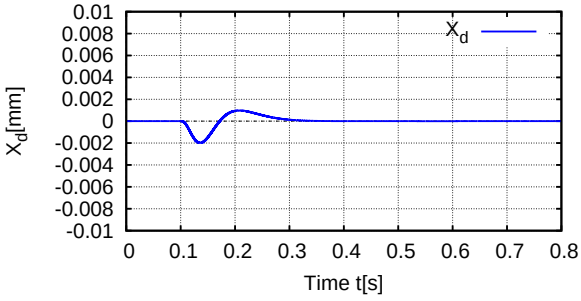

(e) Displacement x_d in mm

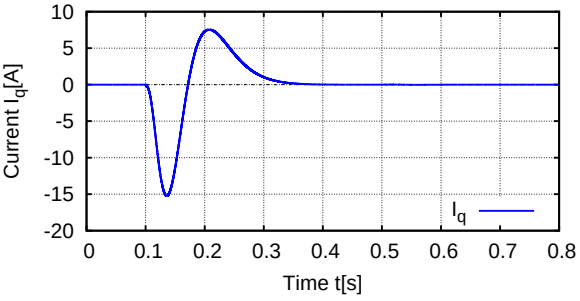

(f) Input q-axis current I_q in A

Figure 7.11: *RotLin* Servo Control Simulation Results

7.5 Vector Control using PP+DOb

7.5.1 Current Controller

From (3.2) and (3.3), the current controller is designed as follows using PI controller.

$$V_d^{ref} = \left(K_{pd} + \frac{K_{id}}{s}\right)(I_d^{ref} - I_d) + \hat{E}_d \tag{7.43}$$

$$V_q^{ref} = \left(K_{pq} + \frac{K_{iq}}{s}\right)(I_q^{ref} - I_q) + \hat{E}_q \tag{7.44}$$

With K_{pd}, K_{pq}, K_{id} and K_{iq} are PI controller gains tunned as follows.

$$K_{pd} = \omega_{id} L \tag{7.45}$$

$$K_{pq} = \omega_{iq} L \tag{7.46}$$

$$K_{id} = \omega_{id} R_s \tag{7.47}$$

$$K_{iq} = \omega_{iq} R_s \tag{7.48}$$

The terms $\hat{E}_d$ and $\hat{E}_q$ are the back-EMF compensations defined as follows.

$$\hat{E}_d = -p\dot{\theta} L_q I_q \tag{7.49}$$

$$\hat{E}_q = p\dot{\theta}(\Psi + L_d I_d) \tag{7.50}$$

Actually, only I_q current is only used to control RotLin i.e $I_d^{ref} = 0$.

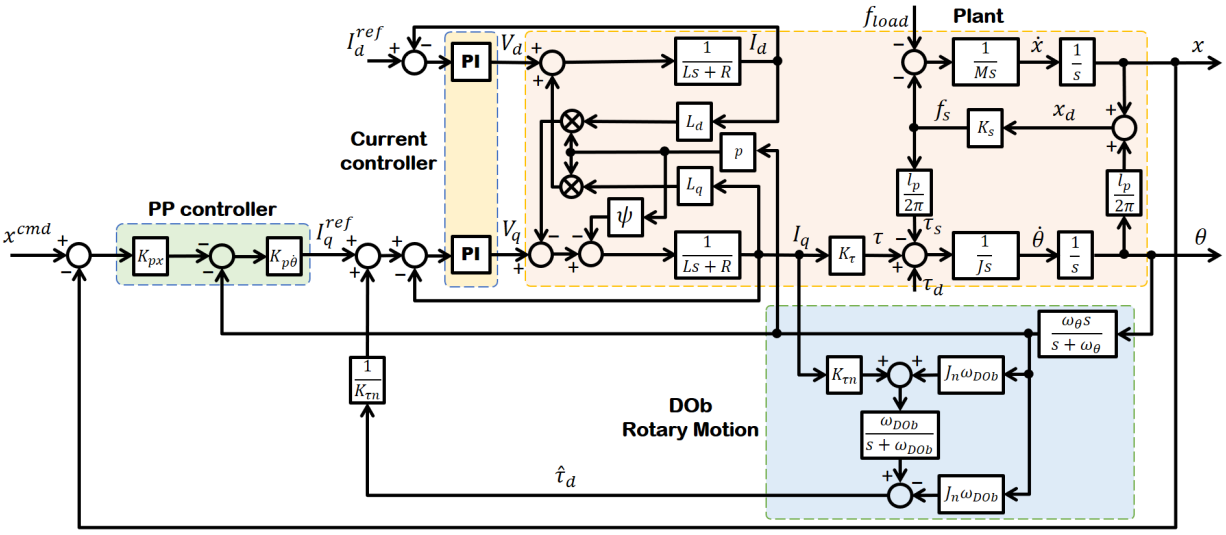

Figure 7.12: Plant-Controller-DOb Block Diagram

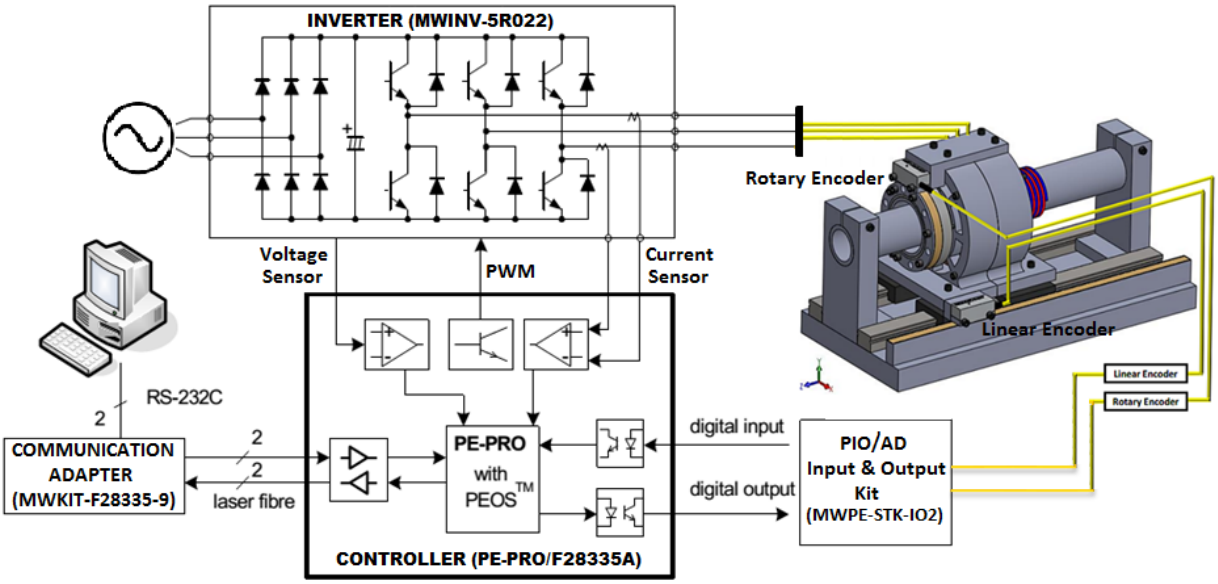

Figure 7.13: Experimental Setup Configuration Diagram

7.5.2 Position & Velocity Controller

The direct-drive of RotLin Helical Machine is achieved by using cascade control where PP+DOb *(with P: Proportional and DOb: Disturbance Observer) was designed to both control the linear position and angular velocity. This last is controlled by using q-axis current, and the overall controller is designed as follows.

$$\dot{\theta}^{cmd} = -K_{px}(x^{cmd} - x) \tag{7.51}$$

$$I_q^{ref} = K_{p\dot{\theta}}(\dot{\theta}^{cmd} - \dot{\theta}) \tag{7.52}$$

The overall transfer function of plant and controller between the input command and response is given in (7.53) and the bode plots of frequency characteristics between input and output are shown in Fig. 7.14(a) for uncontrolled system and in Fig. 7.14(b) and (c) for controlled system.

$$\frac{x}{x^{cmd}} = \frac{K_{px}K_{p\dot{\theta}}K_sK_\tau h}{JMs^4 + K_{p\dot{\theta}}K_\tau Ms^3 + (K_sMh^2 + JK_s)s^2 + K_{p\dot{\theta}}K_sK_\tau s + K_{px}K_{p\dot{\theta}}K_sK_\tau h} \tag{7.53}$$

7.5.3 Disturbance Torque Estimation

The Disturbance Observer (DOb) Torque to compensate the disturbance is designed as follows.

$$\hat{\tau}_d = \frac{\omega_{DOb}}{s+\omega_{DOb}}K_{\tau n}I_q^{ref} - \frac{\omega_{DOb}}{s+\omega_{DOb}}J_n \underbrace{s\theta(s)}_{Acceleration} \tag{7.54}$$

$$= \frac{\omega_{DOb}}{s+\omega_{DOb}}K_{\tau n}I_q^{ref} - \frac{s}{s+\omega_{DOb}}J_n\omega_{DOb}\underbrace{\theta(s)}_{Speed} \tag{7.55}$$

$$= \frac{\omega_{DOb}}{s+\omega_{DOb}}K_{\tau n}I_q^{ref} - \frac{s+\omega_{DOb}-\omega_{DOb}}{s+\omega_{DOb}}J_n\omega_{DOb}\theta(s) \tag{7.56}$$

$$= \frac{\omega_{DOb}}{s+\omega_{DOb}}K_{\tau n}I_q^{ref} - \frac{s+\omega_{DOb}}{s+\omega_{DOb}}J_n\omega_{DOb}\theta(s) + J_n\omega_{DOb}\theta(s) \tag{7.57}$$

$$= \frac{\omega_{DOb}}{s+\omega_{DOb}}\left(K_{\tau n}I_q^{ref} + \frac{\omega_{DOb}}{s+\omega_{DOb}}J_n\omega_{DOb}\theta(s)\right) - J_n\omega_{DOb}\theta(s) \tag{7.58}$$

$$= \frac{\omega_{DOb}}{s+\omega_{DOb}}\left(K_{\tau n}I_q^{ref} + \omega_{DOb}J_n\dot{\theta}\right) - \omega_{DOb}J_n\dot{\theta} \tag{7.59}$$

Where s is the Laplace operator and $\hat{\tau}_d$ is the estimated torque disturbance which the DOb uses to compensate the modeling error and disturbance as proposed in [36].

7.5.4 Experimental and Simulation Results

In order to validate and enact the direct-drive of the proposed machine, experiments were conducted and compared to simulations. The pre-drive tests such as open loop V/f control were

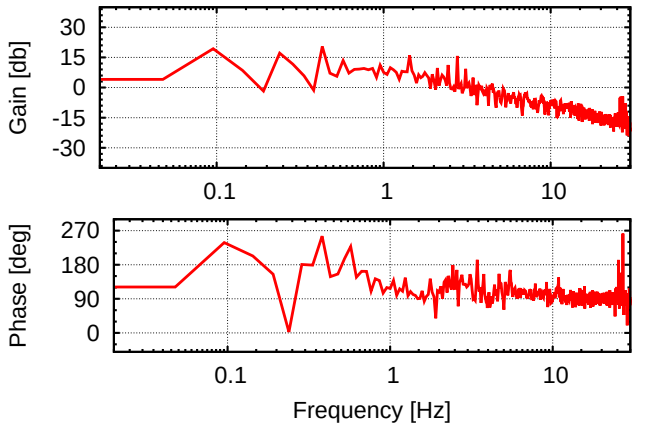

(a) Uncontrolled System $\dot{\theta}/I_q$ *(Experiments)

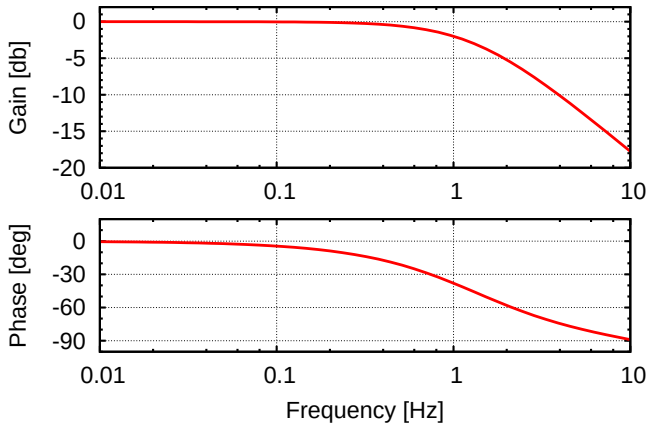

(b) Controlled System x/x^{cmd} *(Simulations)

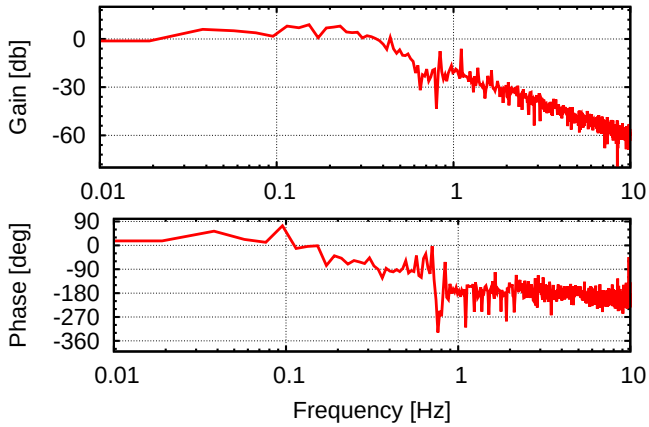

(c) Controlled System x/x^{cmd} *(Experiments)

Figure 7.14: Frequency Characteristics of Uncontrolled and Controlled System

Table 7.2: Plant and Control Parameters of *RotLin*

p	Number of pole pairs	4
l_g	Nominal air gap length	0.8 [mm]
l_m	PM thickness	4 [mm]
l_p	Pitch or Lead Length of screw	5 [mm]
B_r	PM Residual Flux Density	1.2 [T]
R_s	Resistance of Coil Windings	0.345 [Ω]
L_d	d-axis Inductance	0.535 [mH]
L_q	q-axis Inductance	0.535 [mH]
Ψ	Field Flux	9.67 [mWb]
K_τ	Torque Constant	0.0387 [N·m/A]
K_s	Equivalent Spring Coefficient	850 [kN/m]
J	Moment of Inertia of Rotor	67.494×10^{-5} [kg·m^2]
M	Mass of Mover	2.41 [kg]
K_{pd}, K_{pq}	Proportional Gain of Current Controller	24.21
K_{id}, K_{iq}	Integral Gain of Current Controller	15750
K_{px}	Proportional Gain of Linear Position	10200
$K_{p\dot{\theta}}$	Proportional Gain of Angular Velocity	9.7
ω_{id}, ω_{iq}	Bandwidth of Current Control System	45000 [rad/s]
ω_x	Bandwidth of Linear Velocity	3000 [rad/s]
ω_θ	Bandwidth of Angular Velocity	3000 [rad/s]
ω_{DOb}	Bandwidth of Disturbance Observer	10 [rad/s]
Δ_{Reso-x}	Linear Encoder Resolution	1 [μm]
$\Delta_{Reso-\theta}$	Rotary Encoder Resolution	$2\pi/47360$ [rad]
V_{dc}	Inverter input dc voltage	24 [V]
$I_{q-limit}$	dc Current limit	10 [A]

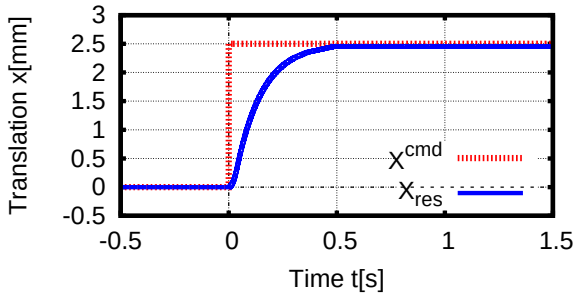

(a) Linear Position Response

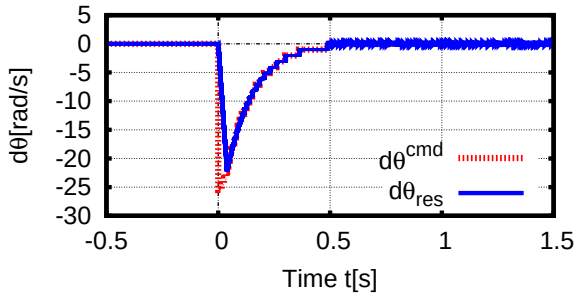

(b) Angular Velocity Control

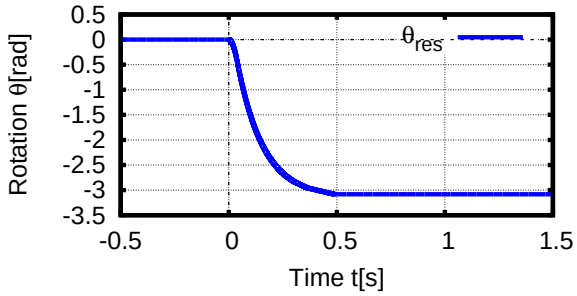

(c) Rotary Position Response

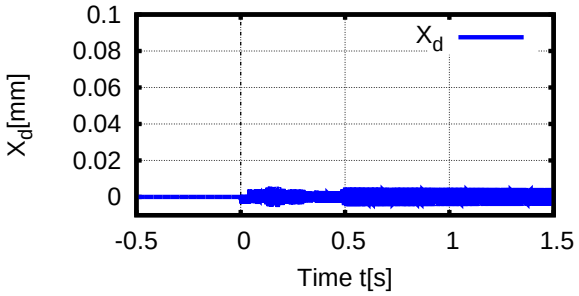

(d) Displacement x_d

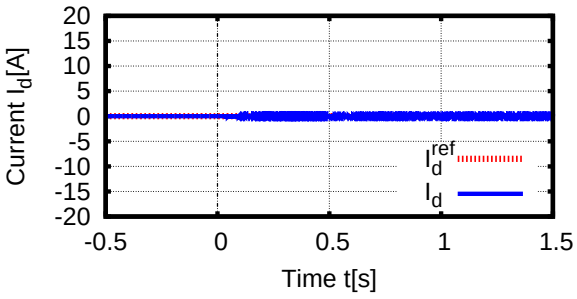

(e) I_d current ($I_d^{ref} = 0$)

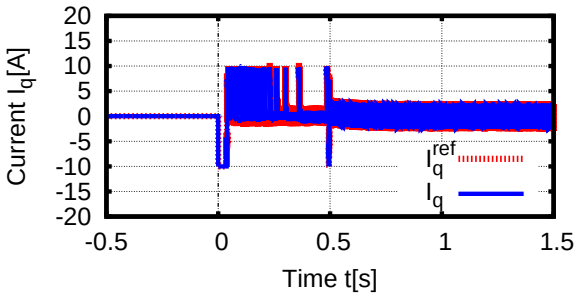

(f) I_q current

Figure 7.15: PP controller with DOb Simulation Results

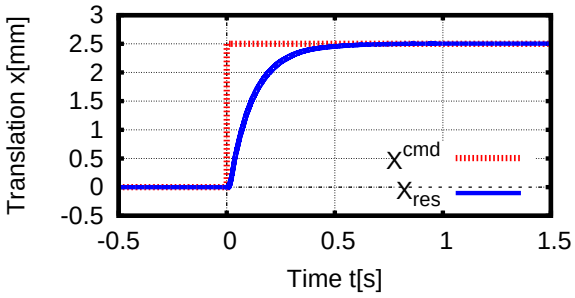

(a) Linear Position Response

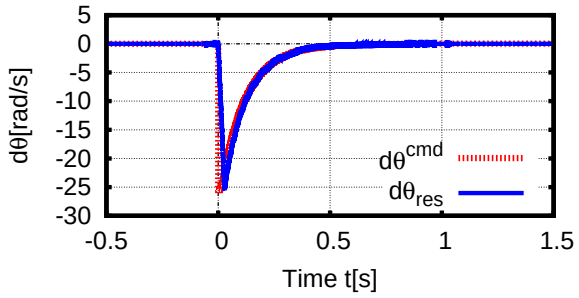

(b) Angular Velocity Control

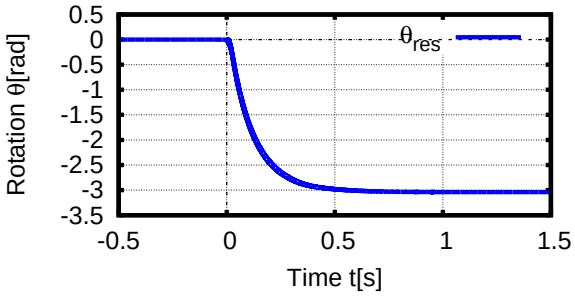

(c) Rotary Position Response

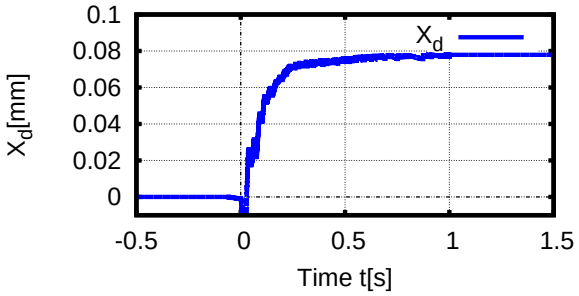

(d) Displacement x_d

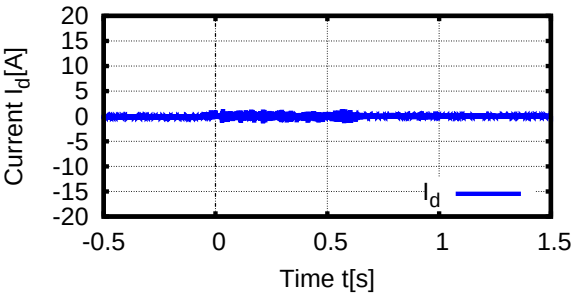

(e) I_d current ($I_d^{ref} = 0$)

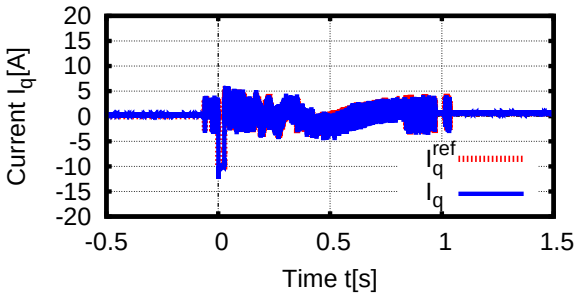

(f) I_q current

Figure 7.16: PP controller with DOb Experimental Results

conducted and presented in [32]. Whereas in this current paper, extensive vector control drive tests were performed by controlling both speed and position for both linear and rotary motions. A step reference linear position of $2.5mm$ is input to the controller system, ideally at $t = 0.0s$ but in reality at $t = 0.5s$. Fig. 7.15 represents the simulation results while Fig. 7.16, the experimental results. As a matter of fact, the enacted machine is validated since the above both results agree each other for the same controller gains. Furthermore, the mechanical angle and translational position responses are respecting the kinematic relation equation $x = -h\theta$, this means when the mid-layer rotor rotates clockwise, the translator moves in the opposite direction. Ideally, x_d should converge to zero as visualized in simulations, but due to some parameterization errors and most possibly relattively small frictions x_d in experiments has a very small value. And again, I_q current has a small current to keep the rotor and/or mover in its steady state. The observed I_d small currents are just reflections and are explained by the nature of the plant voltage circuit in Fig. 7.12.

7.6 Force Control using Force Sensor

An actuator with flexibility and almost maintenance free is being studied, tested and a prototype was developed in order to confirm its design, modeling, backdrivability and controllability. In this section, force control aiming at improving the backdrivability is achieved by experimentally designing a closed-loop force controller to accurately make RotLin become more flexible in terms of backdrivability than in the case of intrinsic backdrivability, thanks to the torque DOb on the system Rotary Motion side designed to compensate the effect of disturbance force through deflective torque.

7.6.1 Controlled Backdrivability of Radial-Gap Helical *RotLin* Actuator

Backdrivability which may be termed also Flexibility in some cases *(i.e not meaning flexible actuators) describes motor or actuator conditions in which when external forces are applied, either rotarly or linearly, they are able to absorb them.

Efficient, high backdrivable actuators with high forces play a remarkable role in robotics in particular and in industrial applications in general. Backdrivable simply describes the ability of such actuator to be flexible to responding to operators maneuvers and it is acheived by force estimatiom. Backdrivability can be described as a special case of force control where the desired force of interaction is zero. [37–39]

In this framework, *RotLin* Radial Gap Helical Machine was conceptualized, designed, modeled, developed and tested. Up to now, *RotLin* brings some hope as it was possible to run it and control it. The details of its designs, tests, position and speed control were presented in previous researches [31–34], and as for the current section, Controlled Backdrivability by using closed-loop force controller is discussed on.

RotLin actuator can generate thrust forces of up to 250N with inherent/intrinsic backdrivability requiring more contact forces whereas controlled backdrivability requires less forces thanks

to the closed-loop force control and torque disturbance observer. As result, *RotLin* actuator can be back-driven with just slight finger force.

The current paper aims at a preliminary closed-loop force control using a force sensor which detects the load disturbance and feedbacks to the controller. A DOb *(Disturbance Observer) on the rotary motion side is used to estimate the disturbance force and thus the improvement of force control robustness and force estimation accuracy. [22, 23, 36]

7.6.2 Estimated, Simulated and Measured Thrust Forces

A high-bandwidth Piezoelectric Force Sensor *(KISTLER Type 9301B), connected to Charge Meter Amplifier *(KISTLER Type 5015), was mounted to the system in order to measure the thrust force and compare it to the estimated force computed from incremental rotary and linear encorders'information using equation (3.6). In Fig. 6.4, the estimated, simulated and measured thrust forces were compared, and thus, the substantially spring constant was confirmed experimentally.

7.6.3 Current Controller

From (3.2) and (3.3), the current controller is designed as follows using PI controller.

$$V_d^{ref} = \left(K_{pd} + \frac{K_{id}}{s}\right)(I_d^{ref} - I_d) + \hat{E}_d \tag{7.60}$$

$$V_q^{ref} = \left(K_{pq} + \frac{K_{iq}}{s}\right)(I_q^{ref} - I_q) + \hat{E}_q \tag{7.61}$$

With K_{pd}, K_{pq}, K_{id} and K_{iq} are PI controller gains tunned as follows.

$$K_{pd} = \omega_{id} L \tag{7.62}$$

$$K_{pq} = \omega_{iq} L \tag{7.63}$$

$$K_{id} = \omega_{id} R_s \tag{7.64}$$

$$K_{iq} = \omega_{iq} R_s \tag{7.65}$$

The terms $\hat{E}_d$ and $\hat{E}_q$ are the back-EMF compensations defined as follows.

$$\hat{E}_d = -p\dot{\theta} L_q I_q \tag{7.66}$$

$$\hat{E}_q = p\dot{\theta}(\Psi + L_d I_d) \tag{7.67}$$

Actually, only I_q current is only used to control RotLin i.e $I_d^{ref} = 0$.

7.6.4 Force Controller & Disturbance Torque Estimation

The force can be controlled indirectly through q-axis current I_q and the controller is basically designed as follows.

$$I_q^{ref} = K_{pf}(f^{cmd} - f_{dis}) \tag{7.68}$$

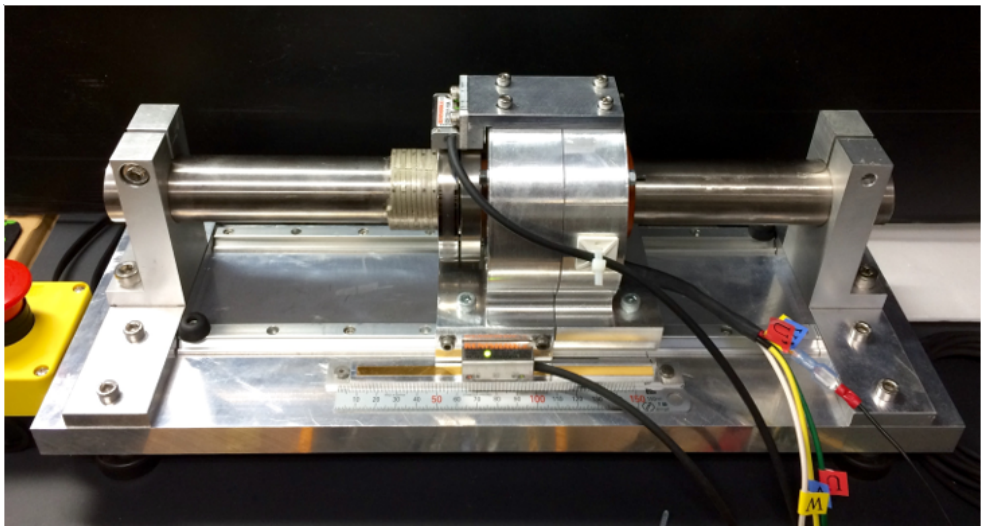

(a) 3D Lateral View of Implemented Prototype

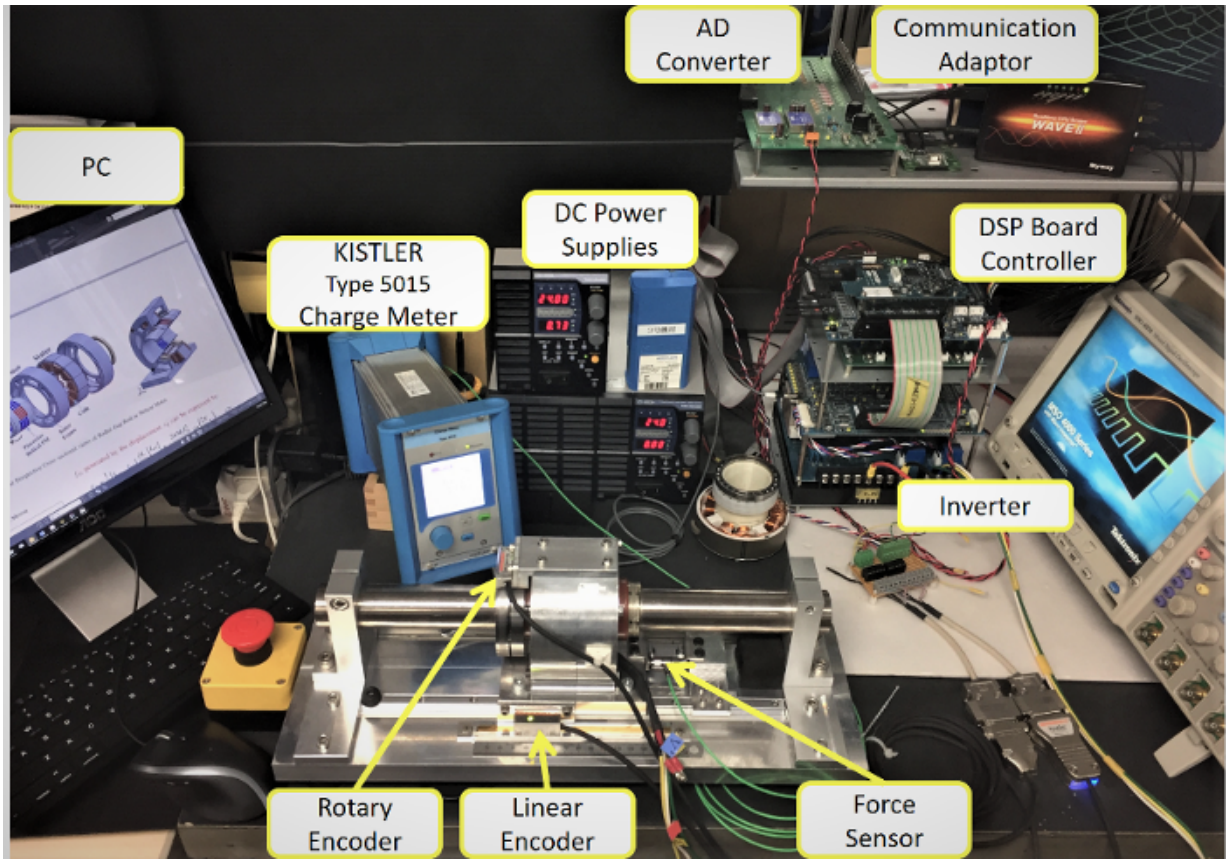

(b) Prototype Experimental Setup

Figure 7.17: Implemented Experimental Prototype - Radial Gap Helical *RotLin* machine

Also, designing the Disturbance Observer (DOb) for the system makes it possible to compensate the modeling error and disturbance. The Torque DOb to compensate the torque disturbance

twisting generated from linear disturbance through transmission equation (3.10) is designed as follows below and the overall block diagram is represented in Fig. 7.12.

$$\hat{\tau}_d = \frac{\omega_{DOb}}{s + \omega_{DOb}} \left(K_{\tau n} I_q^{ref} + \omega_{DOb} J_n \dot{\theta} \right) - \omega_{DOb} J_n \dot{\theta} \tag{7.69}$$

Where s is the Laplace operator and $\hat{\tau}_d$ is the estimated torque disturbance which the DOb uses to compensate the modeling error and disturbance. The calculation of the disturbance torque is based on angular velocity and a first-order Low Pass Filter (LPF) is inserted with ω_{DOb} denoting DOb cut-off angular frequency. When this last is large enough, the estimated disturbance torque can be closer to the actual one.

7.6.5 Experimental Outcomes

The designed controller is conventional and basic as for preliminary force control. Table 7.3 shows the plant ant controller parameters. Except that a Disturbance Observer was designed on the Rotary Motion side to indirectly estimate the effect of disturbance/external linear force on the Linear Motion side. Simply, the high bandwidth force sensor detects force information from the user and/or environment, and the measured force is feedbacked to be compared with the zero force command and the error is compansated by the proportional controller which outputs the reference current to which is added the estimated current from DOb. The resulting current generates a torque to the system thus making it possible for the system to absorb the external force indirect effects and thus improved backdrivability. (See Fig. 7.18)

Briefly, when the linear load force is applied, this last is indirectly transmitted or converted to torque τ_s using equation (3.10). τ_s is somehow a disturbance torque to Rotary Motion Side and it results in the Mid-Layer rotating at the same time translating linearly thanks to the design structure (See Fig. 7.19).

7.7 *RotLin* Modeled as Two-Mass Resonant System

The framework topology of *RotLin* can be related to a Series Elastic Actuator as it is consisted of motor-side *(rotary dynamic) and load-side *(linear dynamic) systems, coupled by magnetic spring K_s. Table 7.4 highlights new parameters of *RotLin* modeled as Two-Mass System.

7.7.1 Conversion of Rotary to Linear Dynamics

Rotary dynamic equation (3.4) is converted to linear equivalent dynamics by defining new variables $X_1 = h\theta$ and $X_2 = -x$; the motor-side and load-side equations are respectively given by:

$$M_1 \ddot{X}_1 = F_1 + F_s \tag{7.70}$$

$$M_2 \ddot{X}_2 = -F_s + F_{load} \tag{7.71}$$

Table 7.3: Plant and Control Parameters of *RotLin*

p	Number of Pole Pairs	4
l_g	Nominal Air Gap Length	0.8 [mm]
l_m	PM thickness	4 [mm]
l_p	Pitch or Lead Length of screw	5 [mm]
B_r	PM Residual Flux Density	1.2 [T]
R_s	Resistance of Coil Windings	0.345 [Ω]
L_d	d-axis Inductance	0.535 [mH]
L_q	q-axis Inductance	0.535 [mH]
Ψ	Field Flux	9.67 [mWb]
K_τ	Torque Constant	0.0387 [N·m/A]
K_s	Equivalent Spring Coefficient	850 [kN/m]
J	Moment of Inertia of Rotor	67.494×10^{-5} [kg·m^2]
M	Mass of Mover	2.41 [kg]
K_{pd}, K_{pq}	Proportional Gain of Current Controller	24.21
K_{id}, K_{iq}	Integral Gain of Current Controller	15750
K_{pf}	Proportional Gain of Force Controller	10
ω_{id}, ω_{iq}	Bandwidth of Current Control System	45000 [rad/s]
ω_x	LPF Cut-off Frequency of Pseudo-Derivative of x	3000 [rad/s]
ω_θ	LPF Cut-off Frequency of Pseudo-Derivative of θ	3000 [rad/s]
ω_{DOb}	Cut-off Frequency of Torque DOb	10 [rad/s]
Δ_{Reso-x}	Linear Encoder Resolution	1 [μm]
$\Delta_{Reso-\theta}$	Rotary Encoder Resolution	$2\pi/47360$ [rad]
V_{dc}	Inverter input dc Voltage	24 [V]
$I_{q-limit}$	dc Current limit	10 [A]

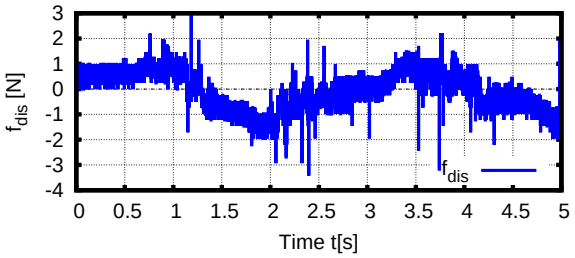

(a) Disturbance/Load Force

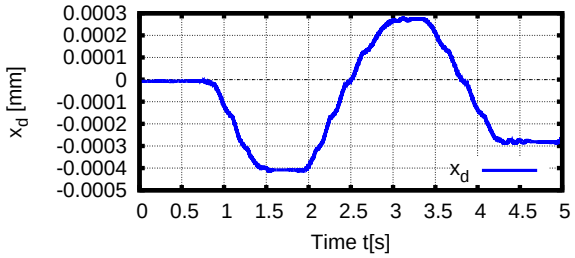

(b) Displacement x_d

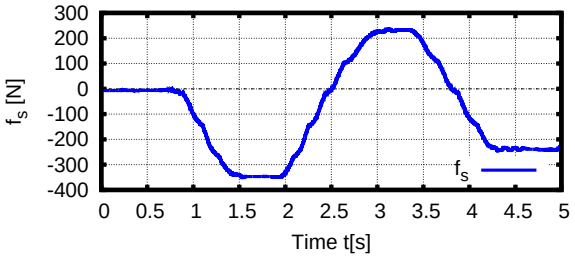

(c) Generated Thrust Force f_s

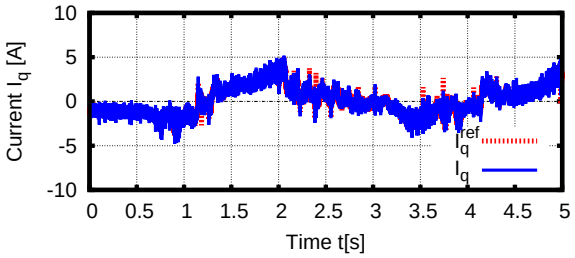

(d) Current I_q

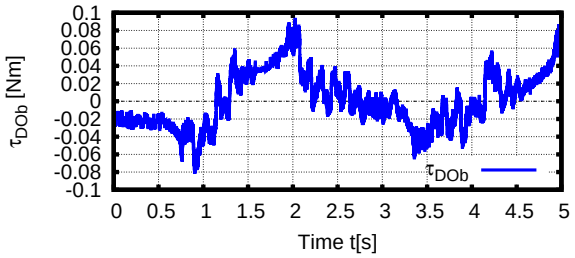

(e) Estimated Disturbance Torque by DOb

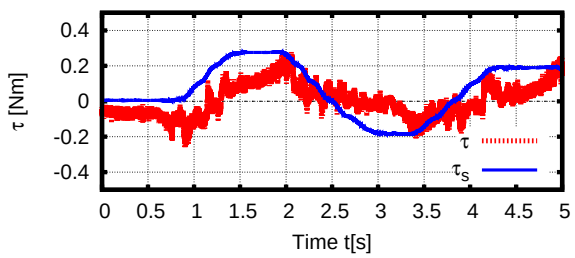

(f) Torque τ vs. Spring Torque τ_s

Figure 7.18: Closed-Loop Force Control aiming at improving *RotLin*'s Backdrivability - Disturbance & Compensation

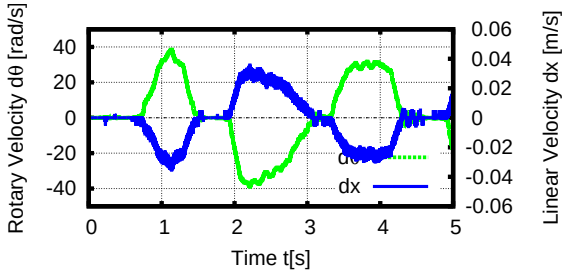

(a) Angular and Linear Velocities

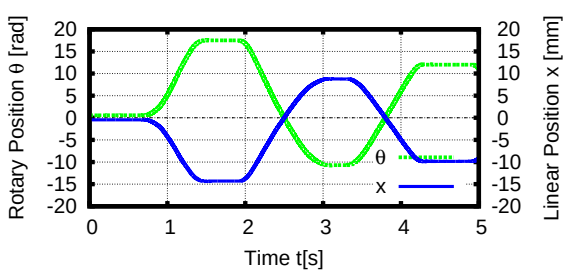

(b) Angular and Linear Positions

Figure 7.19: Closed-Loop Force Control aiming at improving *RotLin*'s Backdrivability - Position and Speed Responses

Table 7.4: Parameters of *RotLin* as Two-Mass System

M_1	Motor-side Mass	1065.8 [kg]
M_{1n}	Motor-side Nominal Mass	1065.8 [kg]
M_2	Load-side Mass	2.41 [kg]
M_{2n}	Load-side Nominal Mass	2.41 [kg]
M_{Res}	Modal Mass of Internal Resonance	2.405 [kg]
ω_{Res}	Resonance Frequency	594.554 [rad/s] = 94.626 [Hz]
$\omega_{Anti-Res}$	Anti-Resonance Frequency	593.883 [rad/s] = 94.519 [Hz]

Where the motor-side mass $M_1 = J/h^2$; force $F_1 = (K_\tau I_q)/h$; and the load-side mass $M_2 = M$. The variables X_1 and X_2, respectively, denoting the linear motor-side position and the linear-load side position. The spring force F_s is given by:

$$F_s = -K_s(X_1 - X_2) \tag{7.72}$$

For unloaded *RotLin* spring, the natural / resonance frequency of the motor-side mass system is given by:

$$\omega_{Res} = \sqrt{\frac{K_s}{M_{Res}}} \tag{7.73}$$

where $M_{Res} = (M_1 \cdot M_2)/(M_1 + M_2)$ is the Modal Mass of Internal Resonance Mode. The Anti-Resonance frequency is given by:

$$\omega_{Anti-Res} = \sqrt{\frac{K_s}{M_2}} \tag{7.74}$$

7.7.2 Transfer Functions and Open-Loop Frequency Responses

After modeling *RotLin* as a Two-Mass system, related transfer functions are derived and open-loop frequency responses *(See Fig. 7.20) are considered.

$$G_1 = \frac{X_1}{F_1} = \frac{M_2 s^2 + K_s}{M_1 M_2 s^4 + (M_1 K_s - M_2 K_s)\, s^2} \tag{7.75}$$

$$G_2 = \frac{X_2}{F_1} = \frac{K_s}{M_1 M_2 s^4 + (M_1 K_s - M_2 K_s)\, s^2} \tag{7.76}$$

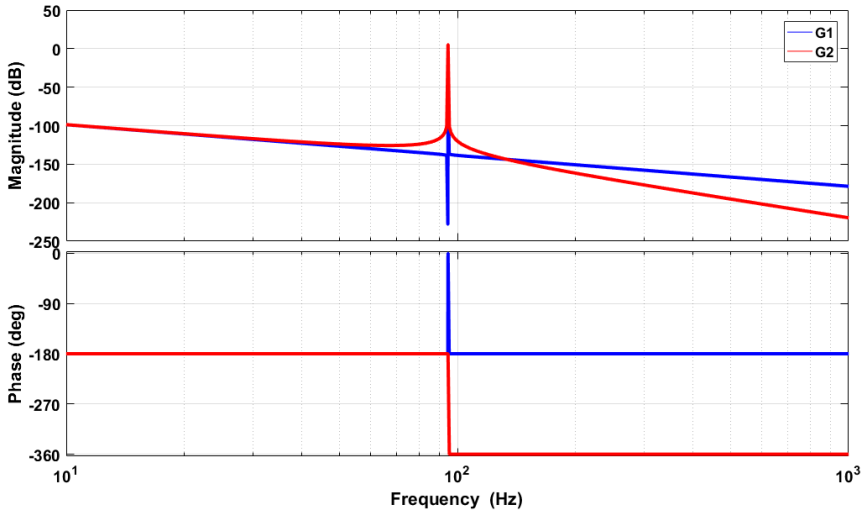

Figure 7.20: Open-Loop Frequency Responses

7.7.3 Force Control Schemes and Goals

Position and speed control were achieved and presented in previous subsections. PP+DOb controller was applied, [31] and also servo control scheme was used to mitigate the error. [31]

As per now, the focus is on force control with or without force sensor and the one utilizing sensor has been achieved though it still needs some improvements. However, in this paper, SEA-based sensoreless force control of *RotLin* when modeled as Two-mass system is presented.

The applied force control is using a method based on higher order derivative. At the beginning of this section, the disturbances δ_1 and δ_2 were assumed to be zero, and hereafter they will be considered.

$$M_1\ddot{X}_1 = F_1 + F_s + \delta_1 \tag{7.77}$$
$$M_2\ddot{X}_2 = -F_s + F_{load} + \delta_2 \tag{7.78}$$

The force reference of the equivalent virtual linear motor is obtained as follows.

$$F_1^{ref} = M_1\ddot{X}_1 + F_s + \hat{\delta}_1 \tag{7.79}$$

where $\hat{\delta}_1$ is Disturbance Observer *(DOb)'s estimated value to compensate δ_1.

Assuming the output $y = F_s$ and the indirect input $u = \dddot{X}_1$. y is differentiated iteratively, and u appears visibly in second order differentiation.

$$y = F_s = K_s(X_2 - X_1) \tag{7.80}$$
$$\dot{y} = \dot{F}_s = K_s(\dot{X}_2 - \dot{X}_1) \tag{7.81}$$
$$\ddot{y} = \ddot{F}_s = K_s(\ddot{X}_2 - \ddot{X}_1) \tag{7.82}$$

Solving (7.82) about $\ddot{X}_1$, u is obtained as follows.

$$\ddot{X}_1 = u = \frac{\ddot{y}}{K_s} + \ddot{X}_2 \tag{7.83}$$

and

$$\ddot{X}_2 = \frac{K_s(X_2 - X_1) - \hat{\delta}_2}{M_{2n}} \tag{7.84}$$

Deciding polynomial roots $\mu_i = (i = 0, 1, 2)$ and feedback gain λ_i, assuming a virtual input $\nu = \ddot{y}$:

$$\nu = \ddot{y} = \ddot{y}^{cmd} + \lambda_1(\dot{y}^{cmd} - \dot{y}) + \lambda_0(y^{cmd} - y) \tag{7.85}$$

The force command of the equivalent linear motor is given by:

$$\begin{aligned} F_1^{ref} &= M_{1n}(\frac{\ddot{y}}{K_s} + \ddot{X}_2) + K_s(X_2 - X_1) + \hat{\delta}_1 && (7.86)\\ &= \frac{M_{1n}}{K_s} + M_{1n}\ddot{X}_2 + K_s(X_2 - X_1) + \hat{\delta}_1 \\ &= \frac{M_{1n}}{K_s}\nu + M_{1n}\left[\frac{K_s(X_2 - X_1) - \hat{\delta}_2}{M_{2n}}\right] + K_s(X_2 - X_1) + \hat{\delta}_1 \\ &= \frac{M_{1n}}{K_s}\nu + \left(1 + \frac{M_{1n}}{M_{2n}}\right)K_s(X_2 - X_1) - \frac{M_{1n}}{M_{2n}}\hat{\delta}_2 + \hat{\delta}_1 && (7.87) \end{aligned}$$

The overall force control scheme is summarized in the block diagram in Fig. 7.21.

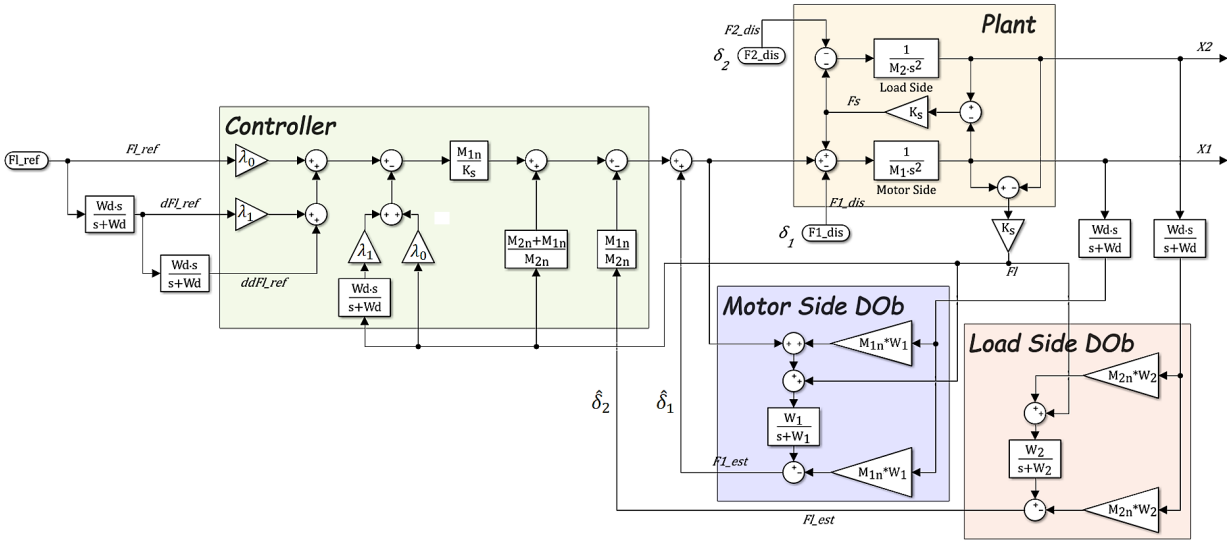

Figure 7.21: *RotLin* Sensorless Force Control Block Diagram *(F_{load}^{ref} is actually F_{load}^{cmd})

7.7.4 Sensoreless Force Control Simulation Results

The proposed force controller does not use any force sensor to detect the disturbance; instead it operates based on the feedback informations from motor and load side encoders. The effects of disturbances are compensated by Multi Encoder Based DObs i.e Motor Side DOb and Load Side DOb; these two lasts estimates the disturbances and compensate them. The load force

command/reference is generated by an S-function and the disturbance by a step function which is inserted at $t = 0.2s$; the control parameters are shown in Table 7.5. The feedback gains are computed as follows.

$$\lambda_0 = \omega_n^2 \tag{7.88}$$
$$\lambda_1 = 2\zeta\omega_n \tag{7.89}$$

where ζ is the Damping Constant. Fig. 7.22 shows the force responses and effects of ζ variations

Table 7.5: *RotLin* System Control Parameters

λ_0	Proportional Feedback Gain of Force Controller	490000
λ_1	Derivative Feedback Gain of Force Controller	1400
ω_1	Motor Side DOb LPF Cut-off Frequency	500 [rad/s]
ω_2	Load Side DOb LPF Cut-off Frequency	500 [rad/s]
ω_d	LPF Cut-off Frequency of Pseudo-Derivative	3000 [rad/s]

for ideal, disturbed and compensated systems. Though the system is disturbed at some point, the effectiveness of proposed controller makes it possible to restore it back to track the reference in relatively very small settling time i.e with this proposed control scheme fast convergence is achieved with no steady state error.

Fig. 7.23 shows that the Load Side DOb's estimated disturbance compensates quickly the disturbance error, while Fig. 7.24 and Fig. 7.25 portray the system linear position responses for ideal and compensated systems respectively.

7.8 Summary

In this section, controlled backdrivability of a novel developped RotLin actuator has be discussed on. Conventional force control using force sensor to detect external force disturbance which is applied linearly on the system Linear Motion side and thus transmitted on the Rotary Motion side causing a disturbance torque, and this last is estimated using a torque DOb. Even though the system is inherently backdrivable but with high stifness, the combination of applied control structure makes it possible for the system to be more flexible and thus improving its backdrivability.

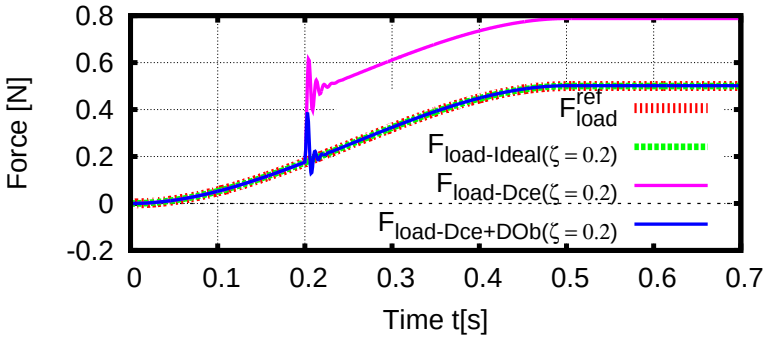

(a) Force Responses *($\zeta = 0.2$)

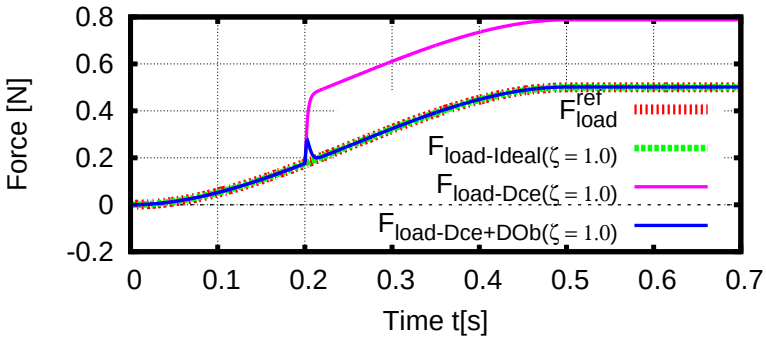

(b) Force Responses *($\zeta = 1.0$)

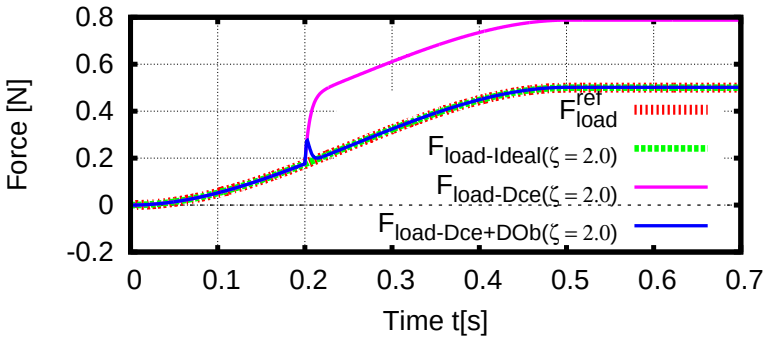

(c) Force Responses *($\zeta = 2.0$)

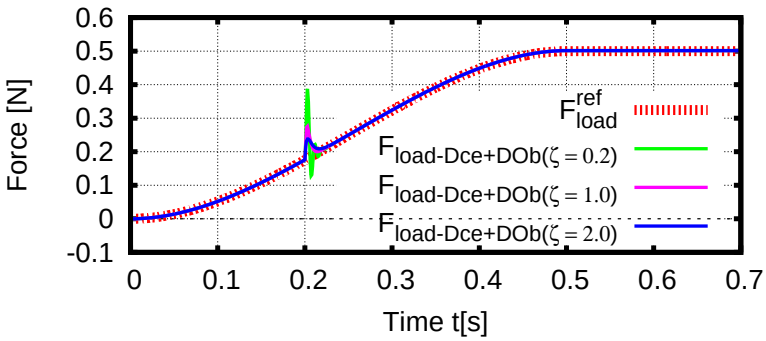

(d) Force Controller + DOb Responses

Figure 7.22: Simulation Results of Force Responses when $\zeta = 0.2 \sim 2.0$ and $\omega_n = 700 rad/s$

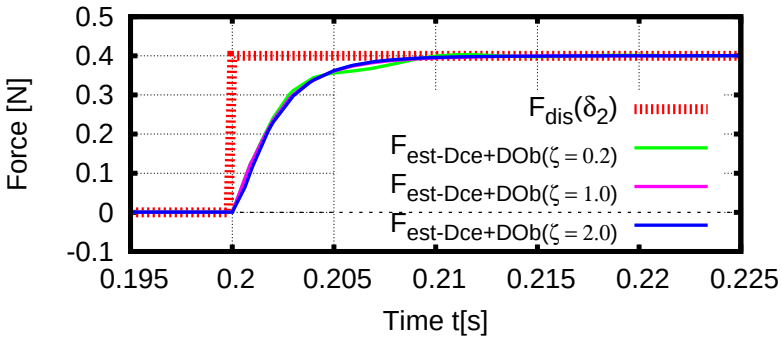

Figure 7.23: *RotLin* Estimated Load Disturbance

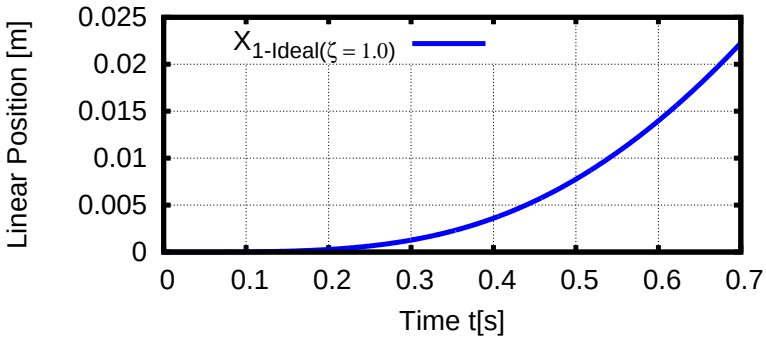

(a) Motor Side Linear Position

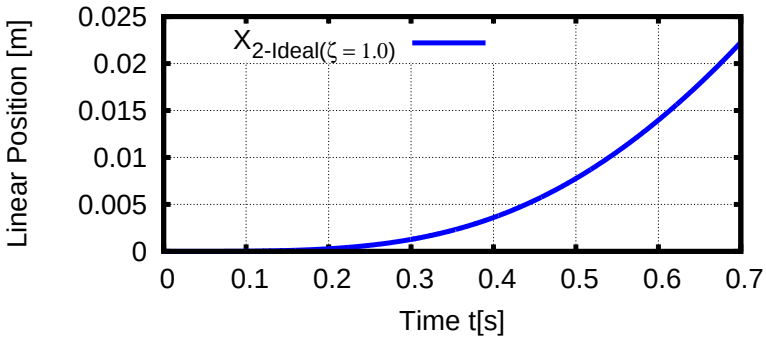

(b) Load Side Linear Position

Figure 7.24: *RotLin* Linear Positions *(Ideal system)

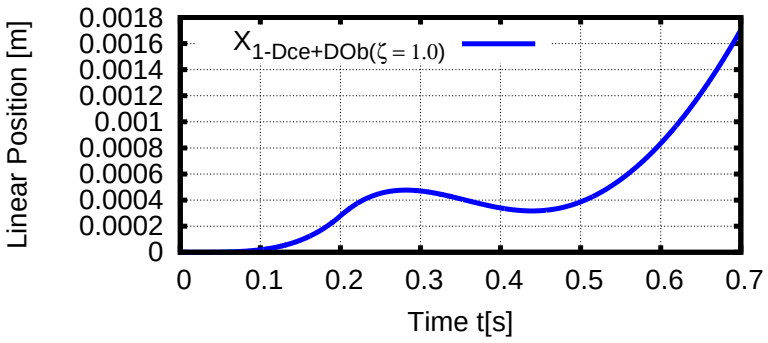

(a) Motor Side Linear Position

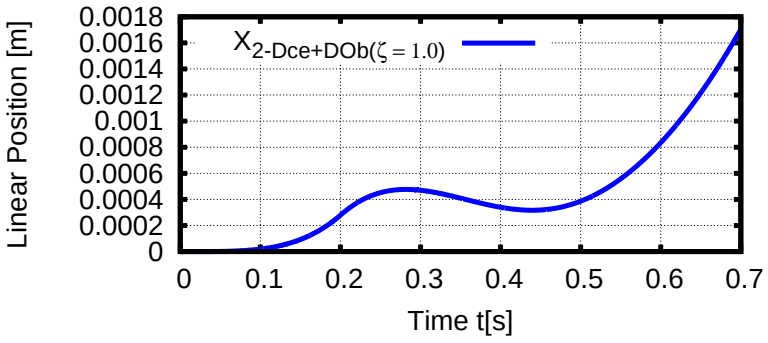

(b) Load Side Linear Position

Figure 7.25: *RotLin* Linear Positions *(Compensated system)

Chapter 8

Performance Evaluation / Comparison

8.1 *RotLin* Specs and Features

The features and specifications of the proposed motor/actuator are summarized in the Table 8.1. The force density was calculated as follows using the values in Table 8.2.

Table 8.1: Specs and Features of *RotLin*

Speed	s_{rpm}	$= 1,800rpm = 30rps$
	ω	$= 188.496rad/s$
Torque	τ	$= 0.2Nm$
Power	P_{out}	$= \tau \times \omega$
		$= 0.2 \times 188.5 = 37.7W = 0.051hp$
		$(P_{(W)} = 746 \times P_{(hp)})$
Current Density		$9.947A/mm^2$
Full-Load Torque	$\tau_{full-load}$	$= (5252 \times HP)/(s_{rpm})$
		$= (5252 \times P_{out})/(s_{rpm} \times 746)$
		$= 0.149Nm$
	$(Where$	$5252 = 33,000/2\pi$
		$HP = 33,000lbs$ lifted one foot in one minute)
Force Density		$6.14MN/m^3$
Thrust Force		$250N$

$$Force \quad Density \quad = \quad \frac{F_s}{nL \times eL \times l_p \times D} = 6.138 \times 10^6 \frac{N}{m^3} \tag{8.1}$$

Table 8.2: Dimensions of *RotLin*

Lead Length	l_p	5mm
Layers	nL	4
Efficient/Active Length	eL	20mm
Outer Diameter	D	94.5mm
Thrust Force	F_s	232N

8.2 Evaluation compared to Axial Gap Spiral Motor

8.2.1 Axial Gap vs. Radial Gap Machines

This topic can be left to various technical papers but at a glance, the said gap describes the air space between two main parts of electrical machines i.e stator and rotor. Topologically, direct-drive electric generators and motors can be designed based on either Axial Flux or Radial Flux technology. Axial means, essentially, on the same axis, while Radial means perpendicular to the axis.

Axial flux motors produce high torque, but their speeds are limited. They are characterized by a higher proportion of electromagnetically active material, thus the percentage of winding mass which yields no torque, but still generating losses, is lower.

Radial flux motors are commonly hybrid systems in which a rotor fitted with permanent magnets rotates within a coil wound stator. A small gap is found between the outer surface of the rotor and the inner diameter of the stator. They can produce high power owing to their ability to run at relatively high speeds.

8.2.2 Comparison to Axial Gap Spiral Motor

Axial gap type Spiral Motor *(described in details in [22,23]) has been previously developed and the current research highlights almost same principle based model but of radial gap type. Radial Gap Helical machine has some advantages compared to its counterpart Axial Gap Helical motor.

For instance, in the Axial Gap Helical Motor there is always a need of controling the gap for the mover rotor to levitate and screw through the spiral stator whereas in the Radial Gap Helical machine there is no need of controlling the gap because it is constant.

8.3 Pros and Cons of selected Actuators

Table 8.3 summarizes some of the already existing actuators and their characteristics [3–5].

Table 8.3: Summary of Actuators and their Characteristics

Actuator	Specs
Piezoelectric	*Pros*: High Force Densities ($2600 \sim 7800 kg/m^3$), Very High Bandwidth (5×10^5–$3\times10^7 Hz$)
	Cons: Limited Strokes. Good in Compression only, not in Tension.
Pneumatic	*Pros*: Force (up to $25kN$), Densities ($180 \sim 250 kg/m^3$), High Bandwidth (5×10^1–$3\times10^2 Hz$), Light, Simple and Fast
	Cons: Less Efficiency at Lower Pressures. Complex System requiring Continuous operation of Air Compressor. High Maintenance Cost.
Hydraulic	*Pros*: Very High Force (up to 25 times than Pneumatic Actuator of the same frame size), Densities ($1600 \sim 2000 kg/m^3$), High Bandwidth (5×10^1–$3\times10^2 Hz$), Large Strokes.
	Cons: Fluid Leakages involving Less Efficiency, Complex System requiring Pumps, Reservoir, Motors, Valves, Heat Exchangers and Noise Reduction Equipment, High Maintenance Cost.
Electro-Mechanical	*Pros*: High Force (up to $40kN$), Rotary to Linear using Ball/Roller Screw, Highest Precision-Control Positioning.
	Cons: Backlash and Elastic Deformation of the Mechanical Transmission, Jamming problem, Non-Linear Frictions.
Electro-Magnetic	*Pros*: Many advantages, in terms of being virtually maintenance free and having a high efficiency over wide operating conditions. Good Positioning Accuracy.
	Cons: High Initial Cost. Vertical Operation Problematic. Cogging Force.

8.4 Summary

In this narrow chapter, the proposed model was contrasted to already existing machines and actuators in point of view specifications, force density; and also important features such as power, Speed, Torque and Current Density were presented.

Chapter 9

Conclusion & Future Work

9.1 Conclusions

An introduction to rotary and linear motion achievement has been given using existing methodologies to attain linear motion from rotary motion. The paper presents thoroughly the novel combination concept of magnetic screw with PM brushless machine. 3-D FEA simulations confirmed that the system can realize rotary and linear motions, and thus obtain high Thrust Force by control of current. The validation of analytical modeling of voltage and dynamic equations used for directly driving the novel Radial Gap *RotLin* Helical motor are logically derived, elaborated and validated experimentally.

The characteristics of this compact linear actuator outweigh the ones of existing magnetic screws, and it can have a wide range of applications in industrial robotics where safe and precise motion is required. In addition, the size, weight and maintainability are of a great advantage. The back-EMF is measured hence the velocity of the motor is computed, also other important characteristics such as Power of about $40W(\approx 0.051hp)$ and Force Density of $6.14MN/m^3$ were determined.

Also, controlled backdrivability of *RotLin* actuator has be discussed on. Conventional force control using force sensor to detect external force disturbance which is applied linearly on the system Linear Motion side and thus transmitted on the Rotary Motion side causing a disturbance torque, and this last is estimated using a torque DOb. Even though the system is inherently/intrinsically backdrivable but with high stifness, the combination of applied control structure makes it possible for the system to be more flexible and thus improving its backdrivability.

9.2 Recommendations for Future Research Work

The research is still underway, therefore, the author of this research thesis concludes by recommending interested researchers to take over and go on improving and optmizing this novelity since it was proven to bring great input to direct-drivable systems where safe and precise motion is required in addition to the high thrust force densities characteristic.

APPENDICES

Appendix A

```
/* Linear Motor Controller Design - Sample */

/* HEADERs */
#include<stdio.h>
#include<math.h>

#define T_MAX 4.0
#define T_START 0.0
#define DT 0.0001  //Sampling Period
#define DT_CONTROL 0.001  //Controller Period
#define DT_OUTPUT 0.001
#define Wdob 200.0*1.0
#define Wc 200.0

/* PLANT MODEL */
#define Kt 22.12
#define M 0.3012
#define D 0.01

/* NOMINAL MODEL */
#define Ktn 22.0
#define Mn 0.3

#define X 0
#define DX 1

/* QUANTIZATION */
#define QMAX M_PI*1.0  // Angle
#define QNUM 256000    // Resolution


/* PLANT */
void plant(double stat[], double u, double t){
int i,j;
double dstat[2] = {0.0, 0.0};
double A[4] = {0.0, 1.0, 0.0, -D/M};
double B[2] = {0.0, Kt/M};
```

```
double dis[2] = {0.0, 0.0};

double Fdis = 0.0;

if(t > 2.5){
Fdis = 10.0*1.0;
}

dis[1] = -Fdis / M;

/* Euler's Method */
for(i = 0; i < 2; i++){
for(j = 0; j < 2; j++){
dstat[i] += A[i*2+j] * stat[j];   //
}
dstat[i] += B[i]*u + dis[i];
}

for(i = 0; i < 2; i++){
stat[i] += dstat[i] * DT;
}
return ;
}


/* PD CONTROLLER */
//double controller(double stat_cmd[], double stat[]){
double controller(double stat[], double t){
double stat_cmd[2] = {0.0, 0.0};
double Ia = 0.0;
double Kp, Kd, dmp;

/* Damping Constant */
//dmp = 0.2;
dmp = 1.0;
//dmp = 2.0;

/* PD Controller Gains */
Kp = 100.0;
Kd = 2.0 * sqrt(Kp) * dmp;

if(t > 0.5){
stat_cmd[0] = 1.0;
}

Ia = Kp * ( stat_cmd[X] - stat[X]);
Ia += Kd * ( stat_cmd[DX] - stat[DX]);
```

```
Ia *= Mn/Ktn;

//printf("%lf %lf \n", t, stat_cmd[0]);

return Ia;
}


/* LOW PASS FILTER */
double filter(double x, double wc, double dt){
static double y = 0.0;
y += wc * (x - y)*dt;
return y;
}


/* DISTURBANCE OBSERVER */
double DObserver(double stat[], double Ia, double t){
double tmp, I_com;
tmp = Ktn*Ia + Wdob*Mn*stat[DX];
tmp = filter(tmp, Wdob, DT_CONTROL);
tmp = tmp - Wdob*Mn*stat[DX];
I_com = tmp/Ktn;
return I_com;
}


/* QUANTIZATION - For Simulations - Encoder */ //Quantize 2PI in 8bits *(256 steps)
double quantization(double x){
double qx;
int cck, c;    // cck: Carry Check; // c: rounding; // QNUM: Reso; // QMAX: Angle
qx = (double)(QNUM-1) * x * 10.0/QMAX;
cck = (int)qx - (int)(qx/10)*10;
//Carry Check
if(abs(cck) >= 5){
c = cck / abs(cck); // "1" or "-1"
}else{
c = 0;
}
qx = QMAX * (double)((int)(qx/10.0) + c) / (double)(QNUM-1);
return qx;
}

/* PSEUDO DIFFERENTIATION */
double PseudoDiff (double x, double w, double dt){
static double y = 0.0;
double dy;
```

```
dy = (x - y) * w;
y += dy * DT_CONTROL;
return dy;
}

/* MAIN PROGRAM */
int main (void){
double cnt_control = DT_CONTROL + 0.5*DT;
double cnt_output = DT_OUTPUT + 0.5*DT;

double t;
double stat[2] = {0.0, 0.0};
double qstat [2] = {0.0, 0.0};

double Ia = 0.0;
static double I_com = 0.0;


/* SAVE/RECORD DATA */
FILE *fp = fopen("outputdata.dat","w");

fprintf(fp, "Time[s], stat_cmd[0], stat[X], stat[DX], qstat[X], qstat[DX], Ia,
Estimated Dce  \n");

for(t = T_START; t < T_MAX; t += DT){
plant(stat, Ia, t);

double stat_cmd[2] = {0.0, 0.0};
if(t > 0.5){               //1.0
stat_cmd[0] = 1.0;
}

/* CONTROL */
if(cnt_control > DT_CONTROL){

//qstat[X] = quantization (stat[X]);     // Quantized Position
qstat[X] = stat[X];
qstat[DX] = PseudoDiff (qstat[X], Wc, DT_CONTROL);

//I_com = filter(stat_cmd[0], 100.0, DT_CONTROL);

I_com = DObserver(qstat, Ia, t);

Ia = controller (qstat, t);
Ia += I_com;

//I_com = DObserver(qstat, Ia, t);
```

```
cnt_control -= DT_CONTROL;
}
cnt_control += DT;

//printf("%lf %lf \n", t, stat_cmd[0]); // Print Preview - Print to Console

/* OUTPUT */
if(cnt_output > DT_OUTPUT){
fprintf(fp, "%lf " , t);
fprintf(fp, "%lf " , stat_cmd[0]);
fprintf(fp, "%lf " , stat[X]);
fprintf(fp, "%lf " , stat[DX]);
fprintf(fp, "%lf " , qstat[X]);
fprintf(fp, "%lf " , qstat[DX]);
fprintf(fp, "%lf " , Ia);
fprintf(fp, "%lf " , I_com*Ktn);
fprintf(fp, "\n");
cnt_output -= DT_CONTROL;
}
cnt_output += DT;
}
return 0;
}
```

Appendix B

Radial Gap Helical *RotLin* Machine

PM Residual Flux Density $B_r := 1.2T$

Lead Length / Pitch $l_p := 5mm$

AirGap Length $l_g := 0.8mm$

Magnet Thickness $l_m := 4mm$

Displacement $x_d := 0.4mm$

Pi $\pi := 3.1415$

Radius $r := 22.25mm$

Vacuum Permeability $\mu_0 = 1.257 \times 10^{-6} \cdot \frac{H}{m}$

Magnetic Permeability $\mu_m := 1 \cdot \mu_0 = 1.257 \times 10^{-6} \cdot \frac{H}{m}$

AirGap Reluctance $R_{m0} := \frac{l_g}{\mu_0 \cdot l_p \cdot \pi r} = 1.822 \times 10^{6} \frac{1}{H}$

$h := \frac{l_p}{2 \cdot \pi} = 7.958 \times 10^{-4} m$

PM Reluctance $R_{mPM} := \frac{l_m}{\mu_m \cdot l_p \cdot \pi r} = 9.108 \times 10^{6} \frac{1}{H}$

Reluctance $R_m := R_{m0} + 2 \cdot R_{mPM} = 2.004 \times 10^{7} \frac{1}{H}$

Mutual Inductance $M_0 := \frac{8}{\pi^2 \cdot R_m} = 4.046 \times 10^{-8} H$

Self Inductance $L_0 := \frac{1}{R_m} = 4.991 \times 10^{-8} H$

PM Equivalent Magnetizing Current $I_m := \frac{B_r \cdot l_m}{\mu_m} = 3.82 \times 10^{3} A$

==> INDUCTANCE MATRIX

$$L := \begin{pmatrix} L_0 & M_0 \cdot \sin\left(\frac{2\pi}{l_p} \cdot x_d\right) \\ M_0 \cdot \sin\left(\frac{2\pi}{l_p} \cdot x_d\right) & L_0 \end{pmatrix} = \begin{pmatrix} 4.991 \times 10^{-8} & 1.949 \times 10^{-8} \\ 1.949 \times 10^{-8} & 4.991 \times 10^{-8} \end{pmatrix} H$$

==> INDUCTANCE MATRIX DERIVATIVE RELATIVE TO DISPLACEMENT

$$\frac{d}{dx_d}\begin{pmatrix} L_0 & M_0 \cdot \sin\left(\frac{2\pi}{l_p} \cdot x_d\right) \\ M_0 \cdot \sin\left(\frac{2\pi}{l_p} \cdot x_d\right) & L_0 \end{pmatrix} \text{ expand } \rightarrow \begin{pmatrix} 0 & \frac{4.4548886318394741359e\text{-}8 \cdot H}{mm} \\ \frac{4.4548886318394741359e\text{-}8 \cdot H}{mm} & 0 \end{pmatrix}$$

==> SPRING FORCE

$$f_{s0} := \frac{2\pi M_0 \cdot I_m^{2}}{l_p}\left(\sin\left(\frac{2\pi}{l_p} \cdot x_d\right)\right) = 357.317 \cdot N$$

==> SPRING CONSTANT

$$K_{s0} := \frac{f_{s0}}{x_d} = 893.292 \cdot \frac{kN}{m}$$

==> DISPLACEMENT $x := 0, 0.05 .. 1.25$

==> SPRING CONSTANT $K := 820$

==> THRUST FORCE function *(Ks = 850kN/m)

$$f(x) := \left[K\left(\sin\left(\frac{2\pi}{5} \cdot x \right) \right) \right]$$

==> THRUST FORCE function

$$f_s(x) := \frac{2\pi M_0 \cdot I_m^{\,2}}{I_p} \cdot \left(\sin\left(\frac{2\pi}{5} \cdot x \right) \right)$$

==> THRUST FORCE - Taylor Series

$$T(x) := \left[K\left(\sin\left(\frac{2\pi}{5} \cdot x \right) \right) \right] \text{series}, 5 \rightarrow 1030.412 \cdot x - 271.17757212445333333 \cdot x^3 + 21.410059943977677726 \cdot x^5$$

==> FORCE vs. DISPLACEMENT

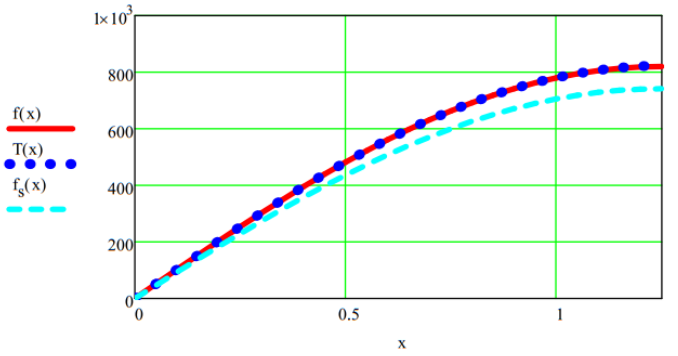

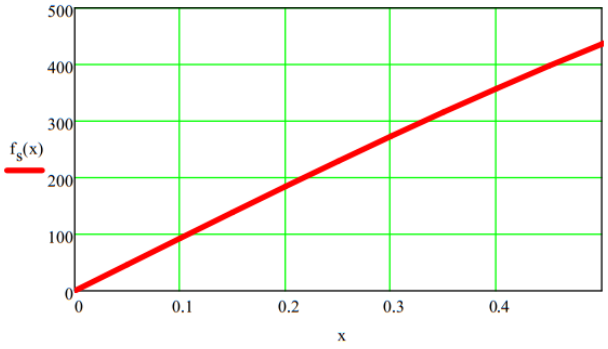

Bibliography

[1] H. Vallery, J. Veneman, E. Asseldonk, R. Ekkelenkamp, M. Buss, and H. Der Kooij, "Compliant Actuation of Rehabilitation Robots", *IEEE Robot. Autom. Mag.*, Vol.15, no.3, pp.60-69, Sep. 2008

[2] G. Xu, A. Song, and H. Li, "Control System Design for an Upper-Limb Rehabilitation Robot", *Adv. Robot.*, Vol.25, no.1/2, pp.229-251, 2011

[3] E. A. Lomonova, "Advanced Actuation Systems State of the Art: Fundamental and Applied Research", *IEEE Int. Conf. on Elec. Mach. and Sys. (ICEMS)*, pp.13-24, Oct. 2010, ISBN: 978-89-86510-11-9

[4] C. Allegranza, L. Gaillard, R. Le Letty, S. Patti, L. Scolamiero, M. Toso, "Actuators for Space Applications: State of the Art and New Technologies ", *14th International Conference on New Actuators*, pp. 283-288, Bremen, Germany, June 2014

[5] J.E. Huber, N.A. Fleck, M.F. Ashby, "The Selection of Mechanical Actuators based on Performance Indices ", *Proc. Royal Society of London A*, pp.2185-2205, October 1997, DOI: 10.1098/rspa.1997.0117

[6] J. Roskam, M. Rice, and H. Eysink, "A Comparison of Hydraulic, Pneumatic, and Electro-Mechanical Actuators for General Aviation Flight Controls", *SAE Technical Paper*, 790623, Feb. 1979, DOI:10.4271/790623

[7] J. Wang, G.W. Jewell, and D. Howe, "A General Framework for the Analysis and Design of Tubular Linear Permanent Magnet Machines", *IEEE Trans. on Magnetics*, Vol.35, no.3, pp.1986-2000, May 1999

[8] M. Karita, "Linear Actuator", JP Patent 2002-027732, Jan. 25, 2002

[9] J. Wang, and D. Howe, "Tubular Modular Permanent-Magnet Machines Equipped with Quasi-Halbach Magnetized MagnetsPart II: Armature Reaction and Design Optimization", *IEEE Trans. on Magnetics*, Vol.41, no.9, pp.2479-2489, Sep. 2005

[10] J. Wang, M. West, D. Howe, H.Z.D. La Parra, and W.M. Arshad, "Design and Experimental Verification of a Linear Permanent Magnet Generator for a Free-Piston Energy Converter", *IEEE Trans. on Energy Conversion*, Vol.22, no.2, pp.299-306, Jun. 2007

[11] N. Bianchi, S. Bolognani, D.D. Corte, and F. Tonel, "Tubular Linear Permanent Magnet Motors: An overall Comparison", *IEEE Trans. on Industrial Electronics*, Vol.39, no.2, pp.466-475, Mar. 2003

[12] F. Cupertino, P. Giangrande, G. Pellegrino, and L. Salvatore, "End Effects in Linear Tubular Motors and Compensated Position Sensorless Control Based on Pulsating Voltage Injection", *IEEE Trans. on Industrial Electronics*, Vol.58, no.2, pp.494-502, Feb. 2011

[13] R. Cao and K.S. Low, "A Repetitive Model Predictive Control Approach for Precision Tracking of a Linear Motion System", *IEEE Trans. on Industrial Electronics*, Vol.56, no.6, pp.1955-1962, Jun. 2009

[14] Y.S. Huang and C.C. Sung, "Function-Based Controller for Linear Motor Control Systems", *IEEE Trans. on Industrial Electronics*, Vol.57, no.3, pp.1096-1105, Mar. 2010

[15] C.C. Sung and Y.S. Huang, "Based on Direct Thrust Control for Linear Synchronous Motor Systems", *IEEE Trans. on Industrial Electronics*, Vol.576, no.5, pp.1629-1639, May 2009

[16] S. Pakdelian, M. Moosavi, H.A. Hussain and H.A. Toliyat, "Control of an Electric Machine Integrated with the Trans-Rotary Magnetic Gear in a Motor Drive Train", *IEEE Trans. on Indusrial Applications*, Vol.53, no.1, pp.106-114, Feb. 2017, DOI:10.1109/TIA.2016.2606092

[17] S. Pakdelian, N.W. Frank, and H.A. Toliyat, "Principles of the Trans-Rotary Magnetic Gear", *IEEE Trans. on Magnetics*, Vol.49, no.2, pp.883-889, Feb. 2013

[18] S. Pakdelian, Y. Deshpande, and H.A. Toliyat, "An Electric Machine Integrated with Trans-Rotary Magnetic Gear", in proc. *IEEE Energy Conversion Congress and Exposition*, pp.3356-3362, Sept. 2012

[19] J. Hashimoto and Y. Kubo, "Magnetic Screw Device", U.S. Patent 5 687 614, Nov. 18, 1997

[20] B. Andrews, "Magnetic Screw ", U.S. Patent 1 562 730, Nov. 24, 1925

[21] N.I. Berg, R.K. Holm, and P.O. Rasmussen, "Theoretical and Experimental Loss and Efficiency Studies of a Magnetic Lead Screw", in proc. *IEEE Energy Conversion Congress and Exposition*, pp.2185-2192, Sept. 2013

[22] I.A. Smadi, H. Omori, Y. Fujimoto, "Development, Analysis and Experimental Realization of a Direct Drive Helical Motor", *IEEE Trans. on Industrial Electronics*, Vol.59, no.5, pp.2208-2216, 2012

[23] Y. Fujimoto, I.A. Smadi, H. Omori, K.Suzuki, H. Hamada, "Modeling and Control of a High Thrust Direct-Drive Spiral Motor", *IEEJ International Conference on Power Electronics*, 24F1-4, pp.2222-2229, 2010

[24] R.K. Holm, N.I. Berg, M. Walkusch, P.O. Rasmussen, and R.H. Hansen, "Design of a Magnetic Lead Screw for Wave Energy Conversion", *IEEE Trans. on Industry Applications*, Vol.49, no.6, pp.2699-2708, Nov. 2013

[25] H. Polinder, M.E.C. Damen, and F. Gardner, “Linear PM Generator System for Wave Energy Conversion in the AWS, *IEEE Trans. on Energy Conversion*, pp.583-589, Sept. 2004

[26] Wenlong Li, K.T. Chau, and J.Z. Jiang, “Application of Linear Magnetic Gears for Pseudo-Direct-Drive Oceanic Wave Energy Harvesting”, *IEEE Trans. on Magnetics*, Vol.47, no.10, pp.2624-2627, Oct. 2011

[27] J. Wang, K. Atallah, W. Wang, “Analysis of a Magnetic Screw for High Force Density Linear Electromagnetic Actuators”, *IEEE Trans. on Magnetics*, Vol.47, no.10, pp.4477-4480, 2011

[28] S. Pakdelian, N.W. Frank and H.A. Toliyat, “Magnetic Design Aspects of the Trans-Rotary Magnetic Gear Apparatus”, *IEEE Trans. on Energy Conversion*, Vol.30, no.1, pp.41-50, March 2015, DOI: 10.1109/TEC.2014.2361289

[29] N.G. Vitale, “Rotary Torque to Axial Force Energy Conversion Apparatus”, U.S. Patent 5 984 960, Nov. 16, 2013

[30] R.J.A. Paul, “Magnetic Rotary-Linear or Linear-Rotary Converter”, *IEE Journal on Electric Power Applications*, Vol.2, no.4, pp.135-138, Aug. 1979, DOI: 10.1049/ij-epa.1979.0022

[31] C.S. Cyusa, Y. Fujimoto, “Enactment Based Direct-Drive Test of a Novel Radial-Gap Helical *RotLin* Machine”, *IEEE Trans. on Industry Applications*, Vol.PP, no.99, pp.1-10, Oct. 2017, DOI: 10.1109/TIA.2017.2766578

[32] C.S. Cyusa, Y. Fujimoto, “Pre-Drive Test of an Implemented Novel Radial-Gap Helical *ROTLIN* Machine”, in proc. *IEEE Energy Conversion Congress and Exposition (ECCE 2016)*, pp.1-7, Sept. 2016, DOI: 10.1109/ECCE.2016.7855366

[33] C.S. Cyusa, Y. Fujimoto, “Modeling and Implementation based Control of a Novel Radial-Gap Helical *ROTLIN* Machine”, in proc. *IEEE Energy Conversion Congress and Exposition (ECCE 2015)*, pp.1803-1809, Sept. 2015

[34] C.S. Cyusa, Y. Fujimoto, “Inherent Back-EMF Measurement of a Novel Radial-Gap Helical *ROTLIN* Machine”, in proc. *IEEJ Sensing, Actuation, Motion Control, and Optimization (SAMCON2016)*, TT2-1, Mar. 2016

[35] Y. Fujimoto, “Direct-Drive Characteristics of Radial-Gap Helical Motors”, *IEEJ Technical Meeting on Mechatronics Control*, MEC-14-136, pp.25-31, Nagaoka, July 2014

[36] K. Ohnishi, M. Shibata, and T. Murakami, “Motion Control for Advanced Mechatronics”, *IEEE/ASME Trans. on Mechatronics*, Vol.1, no.1, pp.56-67, March 1996

[37] C. Mitsantisuk, M. Nandayapa, K. Ohishi, S. Katsura, “Design for Sensorless Force Control of Flexible Robot by Using Resonance Ratio Control Based on Coefficient Diagram Method”, *automatika*, Vol.54, no.1, pp.62-73, 2013, DOI: 10.7305/automatika.54-1.311

[38] C. Mitsantisuk, K. Ohishi, S. Urushihara, S. Katsura, "Kalman Filter-Based Disturbance Observer and its Applications to Sensorless Force Control", *Advanced Robotics*, Vol.25, Iss.3-4, pp.335-353, 2011, DOI: 10.1163/016918610X552141

[39] Y. Ohba, M. Sazawa, K. Ohishi, T. Asai, K. Majima, Y. Yoshizawa, K. Kageyama, "Sensorless Force Control for Injection Molding Machine Using Reaction Torque Observer Considering Torsion Phenomenon", *IEEE Trans. on Industrial Electronics*, Vol.56, no.8, pp.2955-2960, Aug. 2009

[40] K. Abe, T. Suga, and Y. Fujimoto, "Control of a Biped Robot Driven by Elastomer-based Series Elastic Actuator", *12th IEEE International Workshop on Advanced Motion Control (AMC)*, Sarajevo, 2012, pp. 1-6, Mar. 2012, DOI: 10.1109/AMC.2012.6197136

[41] A. Calanca, L. Capisani, and P. Fiorini, "Robust Force Control of Series Elastic Actuators ", *Actuators*, 3, pp.182-204, 2014, DOI:10.3390/act3030182

Related Publications

Journal Papers

- C.S. Cyusa, Y. Fujimoto, "Enactment Based Direct-Drive Test of a Novel Radial-Gap Helical *RotLin* Machine", *IEEE Trans. on Industry Applications*, Vol.54, no.2, pp.1273-1282, Oct. 2017, DOI: 10.1109/TIA.2017.2766578

Conference Papers

- C.S. Cyusa, Y. Fujimoto, "Two Mass System Modeling and Sensorless Force Control applied to Novel Radial-Gap Helical *RotLin* Machine", in proc. *IEEJ Sensing, Actuation, Motion Control, and Optimization (SAMCON 2018)*, SS2-5, Tokyo, JAPAN, Mar. 2018

- C.S. Cyusa, Y. Fujimoto, "Servo Control Feasibility of a Magnetic Screw-Like Radial-Gap *RotLin* Actuator", in proc. *IEEJ Sensing, Actuation, Motion Control, and Optimization (SAMCON 2017)*, TT4-1, Nagaoka, JAPAN, Mar. 2017

- C.S. Cyusa, Y. Fujimoto, "Pre-Drive Test of an Implemented Novel Radial-Gap Helical *ROTLIN* Machine", in proc. *IEEE Energy Conversion Congress and Exposition (ECCE 2016)*, pp.1-7, Milwaukee, USA, Sept. 2016

- C.S. Cyusa, Y. Fujimoto, "Inherent Back-EMF Measurement of a Novel Radial-Gap Helical *ROTLIN* Machine", in proc. *IEEJ Sensing, Actuation, Motion Control, and Optimization (SAMCON 2016)*, TT2-1, Tokyo, JAPAN, Mar. 2016

- C.S. Cyusa, Y. Fujimoto, "Modeling and Implementation based Control of a Novel Radial-Gap Helical *ROTLIN* Machine", in proc. *IEEE Energy Conversion Congress and Exposition (ECCE 2015)*, pp.1803-1809, Montreal, CANADA, Sept. 2015

Honors & Awards

- Best Paper Award *(IEEE Energy Conversion Congress and Exposition (ECCE 2016)), Milwaukee, USA, Sept. 19, 2016

- IEEJ Industry Applications Society Excellent Presentation Award *(IEEJ 3rd International Workshop on Sensing, Actuation, Motion Control, and Optimization (SAMCON 2017)), 2017 IEE-Japan IAS Conference, Hakodate, Japan, Aug. 29, 2017

Unpublished Conference Papers *(Posters)

- C.S. Cyusa, Y. Fujimoto, "Controlled Backdrivability of Radial-Gap Magnetic-Screw Type *RotLin* Actuator ", *20th POWER ELECTRONICS & MOTION CONTROL CAMP (PEMC 2017)*, Tokyo University of Sciences, Chiba, Tokyo, Japan, Sep. 2017)

- C.S. Cyusa, Y. Fujimoto, "Direct Linear Drive Performance of a Radial Gap Electromagnetic-Screw-Like *RotLin* Actuator ", *19th POWER ELECTRONICS & MOTION CONTROL CAMP (PEMC 2016)*, Tokyo University of Sciences, Chiba, Tokyo, Japan, Nov. 2016)

- C.S. Cyusa, Y. Fujimoto, "Modeling and Implementation based Control of a Novel Radial-Gap Helical *ROTLIN* Machine ", *18th POWER ELECTRONICS & MOTION CONTROL CAMP (PEMC 2015)*, Tokyo Denki University, Saitama, Tokyo, Japan, Sep. 2015)

- C.S. Cyusa, Y. Fujimoto, "Multivariable Speed Control of *ROTLIN* Radial Gap Helical Machine ", *17th POWER ELECTRONICS & MOTION CONTROL CAMP (PEMC 2014)*, Tokyo Denki University, Saitama, Tokyo, Japan, Sep. 2014)